Dark Energy And Large Scale Structure

A thesis submitted to The University of Manchester for the degree of
Doctor of Philosophy
in the Faculty of Engineering and Physical Sciences

2011

Steven Pediani

School of Physics and Astronomy

Contents

Word count ~ 22000

List of Figures

List of Tables

Abstract

Currently one of the most exciting problems in cosmology is the nature of dark energy, which is responsible for the late time accelerated expansion of the universe. Dark energy modifies the distance-redshift relation, and governs the late time evolution of gravitational potentials in the universe. Therefore by observing large scale structure we can gain valuable information on the nature of dark energy. In this thesis we examine a particular theory of dark energy, known as elastic dark energy. Using weak lensing and the ISW effect, coupled with CMB and SNIa data, we find lower bounds for the sound speed of elastic dark energy. We also explore how this model behaves in the presence of collapsing matter.

Declaration

I declare that no portion of the work referred to in the thesis has been submitted in support of an application for another degree or qualification of this or any other university or other institute of learning.

Copyright Statement

(i) The author of this thesis (including any appendices and/or schedules to this thesis) owns certain copyright or related rights in it (the Copyright) and s/he has given The University of Manchester certain rights to use such Copyright, including for administrative purposes.

(ii) Copies of this thesis, either in full or in extracts and whether in hard or electronic copy, may be made only in accordance with the Copyright, Designs and Patents Act 1988 (as amended) and regulations issued under it or, where appropriate, in accordance with licensing agreements which the University has from time to time. This page must form part of any such copies made.

(iii) The ownership of certain Copyright, patents, designs, trade marks and other intellectual property (the Intellectual Property) and any reproductions of copyright works in the thesis, for example graphs and tables (Reproductions), which may be described in this thesis, may not be owned by the author and may be owned by third parties. Such Intellectual Property and Reproductions cannot and must not be made available for use without the prior written permission of the owner(s) of the relevant Intellectual Property and/or Reproductions.

(iv) Further information on the conditions under which disclosure, publication and commercialisation of this thesis, the Copyright and any Intellectual Property and/or Reproductions described in it may take place is available in the University IP Policy (see http://www.campus.manchester.ac.uk/medialibrary/policies/intellectual-property.pdf), in any relevant Thesis restriction declarations deposited in the University Library, The University Librarys regulations (see http://www.manchester.ac.uk/library/aboutus/regulations) and in The Universitys policy on presentation of Theses

Acknowledgements

I thank my supervisor, Dr Richard Battye, for giving me an interesting project to work on, and for his help and support over the last few years. I also thank Dr Anthony Holloway and Dr Bob Dickson for their help with problems relating to COMA, and general IT issues.

Finally I thank my parents, sister, and fiancée, Jacqui, for their love and support, without which, none of this would have been possible.

This work was supported by a studentship from the Science and Technology Facilities Council. This thesis was typeset with LaTeX.

The Author

The Author graduated from Lancaster University in 2006 with an M.Phys in Physics, Astrophysics and Cosmology. Since then he has been carrying out research at the Jodrell Bank Centre for Astrophysics. The results of this research are described in this thesis.

Conventions

Unless otherwise stated, we use a spacetime metric, $g_{\mu\nu}$ with signature (-,+,+,+). Spacetime coordinates are expressed as x^{μ}, with Greek indices running from 0 to 3. We use natural units where $\hbar = c = k_B = 1$.

1

Introduction

Cosmology, the study of the Universe, is a relatively modern science that has in recent times seen an explosion in interest due to new and exciting observational results and theories. Physical cosmology attempts to explain why our Universe looks and behaves the way it does, by tying astronomical observations with other disciplines within physics such as general relativity, astrophysics, and particle physics. Our understanding of the universe and our place within it has come along way. In the Second Century the astronomer and mathematician Clauidus Ptolemy published his Almagest, which, using a geocentric model, discussed the motions of the planets and background stars. This idea of the Earth at the centre of the Universe remained popular in European society for over a thousand years. It wasn't until Nicolaus Copernicus published his work on a heliocentric model, in 1543, that the model of Ptolemy was superseded. Further work, notably by Johannes Kepler and Issac Newton in the 17th Century, showed that the planets moved on elliptical orbits around the Sun, and that the mechanism responsible was gravity. In the early part of the 20th Century the astronomer Edwin Hubble discovered that the Cepheid variable stars he was observing were located outside the Milky Way, in other galaxies. He was able to show a relationship between the distance of these Cepheid variables and the redshift of the galaxies they inhabited. Generally the further the galaxy, the larger the observed redshift, in other words Hubble showed that the Universe was expanding. A few years later, Fritz Zwicky proposed the idea of

a new type of matter, called dark matter, to account for the missing matter necessary to explain measured galaxy rotation curves. Following the discovery of an expanding universe, the two big theories of cosmology that emerged were the steady state theory, in which new matter is created as the Universe expands, meaning the Universe looks the same at every point in time, and the big bang model, in which the Universe began life as a singularity which underwent a rapid expansion and continues to expand today. George Gamow predicted that a big bang would leave the universe bathed in a background radiation, which would posses a blackbody spectrum and be isotropic. In 1964 this Cosmic Microwave Background (CMB) was detected by Arno Penzias and Robert Wilson, and with this, the hot big bang model was established as the most popular cosmological theory of our Universe. This model explains, the origins of the CMB, nucleosynthesis of the light elements (deuterium, helium-3, helium-4, and lithium), the expansion of the Universe, and the formation of large scale structure. Just before the turn of the 21th Century, it was observed by two independent groups (Riess et al. (1998), and Perlmutter et al. (1999)) that the Universe appeared to have recently entered a period of accelerated expansion. The cause of this acceleration is unknown, and the term dark energy was coined to describe the collective theories put forward to explain it. One of the more popular theories is the ΛCDM model which consists of a universe currently dominated by a cosmological constant, Λ, while also containing cold dark matter (CDM), baryonic matter, and radiation. A model, which is spatially flat, containing $\approx$ 73% dark energy, $\approx$ 23% CDM, and $\approx$ 4% baroyinc matter, is sometimes known as the Cosmic Concordance Model (CCM), due to the agreement between many independent astronomical measurements. While this models predictions match observational measurements, it is not without its problems, which leaves the door open for many other theories that aim to improve upon the ΛCDM model. The area of dark energy is now a subject in its own right within cosmology, and the basis of this thesis is to examine a particular model of dark energy, known as elastic dark energy, and to comment on how this model's presence affects observable astronomical quantities. By doing so we aim to constrain the model's parameters and also show that elastic dark

energy is not ruled out by a variety of observational data.

1.1 Basics of cosmology

Given that we appear to live in an expanding universe, it is helpful to factor the expansion out by defining two different distance measures, $r = a\chi$, where a is known as the scale factor, which we define to be equal to 1 at the present day, χ is the comoving distance, and r the real distance. The distance between two points in such a universe increases with time, but in the absence of peculiar velocities, the comoving distance remains constant. How the scale factor evolves with time depends on the geometry, and total energy density of the Universe. We can define the Hubble parameter as, $H(t) \equiv \frac{da}{dt}\frac{1}{a}$, where, as derived later,

$$H^2(t) = \frac{8\pi G}{3}\rho_{\text{total}} - \frac{k}{a^2}\,, \tag{1.1}$$

where ρ_{total} is the combined density of all the energy density components in the Universe, and k measures the curvature of space. This then gives us a relation between the expansion of the universe, and the energy density of constituent components and curvature of space. When appropriately scaled, k can be made dimensionless and take on three values, -1, 0 and 1, corresponding to an open, flat, or closed universe. An open, or hyperbolic universe has the property that the angles of a triangle add up to be more than 180°, or in other words, two lines running parallel would eventually diverge from one another. Such a universe would be infinite in extent. A closed universe has the opposite properties in that parallel lines eventually cross one another, and angles of a triangle add up to less than 180°. Such a universe is finite, hence the name, closed. A flat universe is one where the angles of a triangle add up to exactly 180° and parallel lines remain parallel as in Euclidean geometry. In order for the universe to be flat, the energy density of the universe must be an exact value, known as the critical density. H is usually expressed as $h\,100\,\text{km}\,\text{s}^{-1}\,\text{Mpc}^{-1}$, where h has been observed to be ≈ 0.7 (Jarosik et al. (2011)), making today's value of the Hubble parameter $H_0 \approx 70\,\text{km}\,\text{s}^{-1}\,\text{Mpc}^{-1}$.

Rearranging (1.1) we find that today's value of the critical density is given as,

$$\rho_c = \frac{3H_0^2}{8\pi G}\,. \tag{1.2}$$

In SI units, this becomes $\rho_c = 1.88\,h^2 \times 10^{-29}\,\mathrm{g\,cm^{-3}}$. The Universe has been measured to be remarkable flat (Spergel et al. (2007)), and for this work, we will now only consider a flat universe, $k = 0$. It is useful to define the density parameter of a given energy density component, x, as,

$$\Omega_x(t) \equiv \frac{\rho_x(t)}{\rho_{\mathrm{total}}(t)}\,, \tag{1.3}$$

where $\rho_x(t)$ is the average energy density of component x, and $\rho_{\mathrm{total}}(t)$ is the sum of the average energy density of all components. We can now write the Friedmann equation in terms of the density parameter,

$$H^2(t) = H_0^2 \sum_x \Omega_x(t)\,. \tag{1.4}$$

Another important cosmological equation is the fluid equation,

$$\dot{\rho}_x = -3H\left(\rho_x + P_x\right) = -3H\rho_x\left(1 + w_x\right)\,, \tag{1.5}$$

where the dot denotes a derivative with respect to time, and we have introduced the equation of state parameter, $w = \frac{P}{\rho}$, with P being the pressure of the fluid. The fluid equation tells us how the density of each species, x, evolves with time. If we integrate the fluid equation, we can write,

$$\Omega_x(t) = \Omega_x a^{-3(1+w)}\,, \tag{1.6}$$

where Ω_x is today's value. The fluid equation, combined with differentiating the Friedmann equation with respect to time yields a third cosmological equation, the acceleration equation,

$$\frac{\ddot{a}}{a} = -\frac{4\pi G}{3}\rho\left[1 + 3w\right]\,. \tag{1.7}$$

In an expanding universe, distance is now a function of the scale factor. The comoving distance from an observer to a source located at a scale factor, a, is given by,

$$\chi(a) = \int_{t(a)}^{t_0} \frac{dt'}{a(t')} = \int_a^1 \frac{da'}{a'^2 H(a')} \,. \tag{1.8}$$

To obtain the physical distance to the source, the comoving distance must be multiplied by $a(t)$. Since light has a finite speed, parts of the universe are not casually connected. An observer can define a cosmological horizon, which is the furthest point that light could have travelled to the observer given the age of the Universe, and so is the barrier between the observable and unobservable regions of the Universe. The comoving distance to this horizon is given by,

$$d_H(t) = \int_0^{t_0} \frac{dt'}{a(t')} \,, \tag{1.9}$$

where t_0 is the time today. In a similar way to the definition of a comoving distance, we can define comoving, or conformal time, which is given by $d\tau = dt/a$, and so with the speed of light set to $c = 1$, τ and χ are the same. Using conformal time, we can define the conformal Hubble parameter which is given by,

$$\mathcal{H} = \frac{1}{a}\frac{da}{d\tau} = aH \,. \tag{1.10}$$

1.2 Fundamentals of general relativity

In order to describe our Universe, we first need a relation between the geometry of space, and the energy density of objects in said space. General relativity, published by Einstein in 1915, gives us these tools and allow us to proceed with describing our universe. In our everyday Euclidean world we measure the separation between two objects by measuring the distance, s, between them, given by $s^2 = x^2 + y^2 + z^2$. In the special theory of relativity, temporal separation must also be considered as there is no such thing as a universal time. The separation between two events in spacetime is now

given by the line element,

$$ds^2 = -dt^2 + dx^2 + dy^2 + dz^2 \,. \tag{1.11}$$

If $ds^2 < 0$ the spacetime interval between two events is said to be timelike, and a causal relationship exists between these two events. If the interval is $ds^2 > 0$, then the interval is spacelike, and the events are not casually connected and the spatial distance is so large that travelling at the speed of light is not enough to traverse it. If $ds^2 = 0$ the interval is lightlike and this separates the regions which are causally linked, to ones which are not. This line element is called the Minkowski coordinate system, and can be written as,

$$ds^2 = \sum \eta_{\mu\nu} dx^\mu dx^\nu \,, \tag{1.12}$$

where $\eta_{\mu\nu}$ is the Minkowski metric and is given by,

$$\eta_{\mu\nu} = \begin{pmatrix} -1 & 0 & 0 & 0 \\ 0 & 1 & 0 & 0 \\ 0 & 0 & 1 & 0 \\ 0 & 0 & 0 & 1 \end{pmatrix}, \tag{1.13}$$

and we have introduced index notation where $x^0 = t$, $x^1 = x$, $x^2 = y$, and $x^3 = z$. When we want to refer specifically to spatial indices we will use Roman indices, whereas generally we will use Greek indices. It is convention to sum over repeated indices, and we will therefore remove the summation term in (1.12) from now on.

In Minkowski space particles obey Newton's laws, if no force acts on a particle, it will travel in a straight line. In general relativity the idea of a straight line is replaced with a geodesic, where gravity is not thought of as an external force, but the curvature of spacetime. In general relativity a particle with no external force acting on it travels along a geodesic. The Minkowski metric is replaced with the metric tensor, $g_{\mu\nu}$. The equations of motion,

$$\frac{d^2x^i}{dt^2} = 0\,, \tag{1.14}$$

is replaced with the geodesic equation, given by,

$$\frac{d^2x^\mu}{d\lambda^2} = -\Gamma^\mu_{\alpha\beta}\frac{dx^\alpha}{d\lambda}\frac{dx^\beta}{d\lambda}\,. \tag{1.15}$$

Time is now an evolving parameter and hence we parameterize a particle's path with λ, so a vector x^μ is now a function of λ. We have also introduced the connection coefficients, also known as Christoffel symbols, given by,

$$\Gamma^\mu_{\alpha\beta} = \frac{1}{2}g^{\mu\rho}\left[\partial_\alpha g_{\beta\rho} + \partial_\beta g_{\alpha\rho} - \partial_\rho g_{\alpha\beta}\right]\,, \tag{1.16}$$

where we have written the partial derivatives as $\partial/\partial x^\mu = \partial_\mu$, and $\partial/\partial x_\mu = \partial^\mu$. A tensor is defined by the way it transforms from one coordinate system to another. For example, the covariant tensor transforms as,

$$A'_\mu = \frac{\partial x_\nu}{\partial x'_\mu}A_\nu\,, \tag{1.17}$$

and a contravariant tensor transforms as,

$$A'^\mu = \frac{\partial x'_\mu}{\partial x_\nu}A^\nu\,. \tag{1.18}$$

Under a transformation, the partial derivatives do not transform in the same way as tensors, and so we define a covariant derivative. The covariant derivative of a contravariant tensor is,

$$\nabla_\rho A^\mu = \partial_\rho A^\mu + \Gamma^\mu_{\rho\sigma}A^\sigma\,, \tag{1.19}$$

and for a covariant tensor,

$$\nabla_\rho A_\mu = \partial_\rho A_\mu - \Gamma^\sigma_{\rho\mu}A_\sigma\,. \tag{1.20}$$

The first part is just the partial derivative, the other parts with the Christoffel symbols are the corrections, defined to make the covariant derivative transform like a tensor. We will be using the metric for a Friedmann-Robertson-Walker (FRW) universe, which is a universe that is homogeneous and isotropic. This metric in a flat universe is given by,

$$g_{\mu\nu} = \begin{pmatrix} -1 & 0 & 0 & 0 \\ 0 & a^2(t) & 0 & 0 \\ 0 & 0 & a^2(t) & 0 \\ 0 & 0 & 0 & a^2(t) \end{pmatrix}, \tag{1.21}$$

where a is the scale factor. The assumption of homogeneity and isotropy apply on the large scales of the universe. Clearly on small scales the universe is lumpy, littered with galaxies surrounded by huge voids of space. But as we look at larger scales these ”lumps” smooth out. If we assume the Copernican principle, that we do not observe the universe from a special vantage point, and with the knowledge that the CMB is very smooth, with the differences in temperature varying by $\approx 10^{-5}$ at the most, it follows that the rest of the universe must also be homogeneous and isotropic. The Reimmann curvature tensor is given by,

$$R^{\sigma}{}_{\rho\mu\nu} = \partial_\mu \Gamma^{\sigma}{}_{\rho\nu} - \partial_\nu \Gamma^{\sigma}{}_{\rho\mu} + \Gamma^{\sigma}{}_{\mu\alpha}\Gamma^{\alpha}{}_{\rho\nu} - \Gamma^{\sigma}{}_{\nu\alpha}\Gamma^{\alpha}{}_{\rho\mu}\,. \tag{1.22}$$

The Ricci tensor $R_{\mu\nu}$ is a contraction of the Riemmann tensor,

$$R_{\mu\nu} = R^{\rho}{}_{\mu\rho\nu} = \partial_\rho \Gamma^{\rho}{}_{\mu\nu} - \partial_\nu \Gamma^{\rho}{}_{\rho\mu} + \Gamma^{\rho}{}_{\rho\sigma}\Gamma^{\sigma}{}_{\mu\nu} - \Gamma^{\rho}{}_{\rho\nu}\Gamma^{\nu}{}_{\rho\mu}\,, \tag{1.23}$$

and the Ricci scalar is the contraction of the Ricci Tensor, $R = g^{\mu\nu}R_{\mu\nu}$. These equations govern the curvature of space and appear in the Einstein field equations which are given by,

$$G^{\mu}{}_{\nu} \equiv R^{\mu}{}_{\nu} - \frac{1}{2}\delta^{\mu}{}_{\nu}R = 8\pi G T^{\mu}{}_{\nu}\,. \tag{1.24}$$

The left side of (1.24) is the curvature part, the right side is the source of the curvature, governed by the energy-momentum tensor $T^{\mu}{}_{\nu}$. We have enough information now to

compute the curvature part of (1.24) using an FRW metric. The Christoffel symbols are,

$$\Gamma^0{}_{00} = 0\,, \tag{1.25}$$

$$\Gamma^0{}_{ij} = \delta_{ij}\dot{a}a\,, \tag{1.26}$$

$$\Gamma^i{}_{0j} = \Gamma^i{}_{j0} = \delta^i_j\frac{\dot{a}}{a}\,, \tag{1.27}$$

$$\Gamma^0{}_{0i} = \Gamma^0{}_{i0} = 0\,. \tag{1.28}$$

With these we can work out that the Ricci tensor components are,

$$R_{00} = -3\frac{\ddot{a}}{a}\,, \tag{1.29}$$

$$R_{ij} = \delta_{ij}\left(2\dot{a}^2 + a\ddot{a}\right)\,. \tag{1.30}$$

And finally the Ricci scalar is,

$$R = 6\left(\frac{\dot{a}^2}{a^2} + \frac{\ddot{a}}{a}\right)\,. \tag{1.31}$$

We now turn to the right side of equation (1.24) which creates the curvature we observe. A perfect fluid has an energy-momentum tensor given by

$$T^{\mu\nu} = (\rho + P)u^\mu u^\nu + Pg^{\mu\nu}\,, \tag{1.32}$$

where the rest frame density and pressure of the fluid are given by ρ and P, and u^μ is the velocity vector field. In a frame comoving with the fluid, the energy-momentum tensor is given by,

$$T^{\mu}{}_{\nu} = \begin{pmatrix} -\rho & 0 & 0 & 0 \\ 0 & P & 0 & 0 \\ 0 & 0 & P & 0 \\ 0 & 0 & 0 & P \end{pmatrix} . \tag{1.33}$$

Putting (1.29) and (1.33) together gives the Friedmann equation,

$$H^2 = \frac{8\pi G}{3}\rho \, . \tag{1.34}$$

The trace part of the Einstein equation gives us the acceleration equation,

$$\frac{\ddot{a}}{a} = \frac{4\pi G}{3}\left[\rho + 3P\right] \, . \tag{1.35}$$

We can obtain the fluid equation by taking the covariant derivative of the energy-momentum tensor, knowing that it must be equal to zero due to energy conservation, $\nabla_{\mu} T^{\mu 0} = 0$,

$$\dot{\rho} + 3H(\rho + P) = 0 \, . \tag{1.36}$$

1.3 Perturbed cosmological equations

The equations derived so far have only been dependent on time, and describe the background evolution of the Universe. The Universe is not completely smooth however, and in order to describe gravitational perturbations in the energy density components, we need to perturb our metric. We will now be working in conformal time where $d\tau = dt/a$, and we will be using the synchronous gauge as this is what is used in the CMB codes, CMBFAST (Seljak and Zaldarriaga (1996)) and CAMB (Lewis et al. (2000)) (see Chapters 2 and 3). Unless otherwise referenced, the following discusion is taken from Ma and Bertschinger (1995). A general perturbed metric can be defined as,

$$g_{\mu\nu} = a^2\left(\eta_{\mu\nu} + h_{\mu\nu}\right), \tag{1.37}$$

and we can set the components h_{00} and h_{0i} equal to zero to remove the gauge freedom in the Einstein equations. The metric perturbation h_{ij} can be decomposed into scalar, vector and tensor components, which correspond to density, vorticity and gravity wave perturbations respectively. During the expansion of the Universe the vector modes are suppressed and so are not normally considered. Working in Fourier space, the decomposed metric perturbation can be written as,

$$h_{ij} = \hat{k}_i\hat{k}_j h + 6\eta\left(\hat{k}_i\hat{k}_j - \frac{1}{3}\delta_{ij}\right) + \hat{k}_i h^V_j + \hat{k}_j h^V_i + h^T_{ij}, \tag{1.38}$$

where the superscript V and T refer to vector and tensor respectively. Using this decomposition, the perturbed Einstein equations in the synchronous gauge are (Battye and Moss (2007)),

$$a^2 G^0{}_0 = -3\mathcal{H}^2 - \mathcal{H}\dot{h} + \frac{1}{2}\partial_i\partial^i h - \frac{1}{2}\partial_i\partial_j h^{ij}, \tag{1.39}$$

$$2a^2 G^0{}_i = \partial_i\dot{h} - \partial_j\dot{h}^j{}_i, \tag{1.40}$$

$$2a^2 G^i{}_0 = \partial_j\dot{h}^{ij} - \partial^i\dot{h}, \tag{1.41}$$

$$a^2 G^i{}_j = \left(2\dot{\mathcal{H}} - \mathcal{H}^2\right)\delta^i{}_j + \frac{1}{2}\left(\ddot{h}^i{}_j - \ddot{h}\delta^i{}_j\right) + \mathcal{H}\left(\dot{h}^i{}_j - \dot{h}\delta^i{}_j\right) \tag{1.42}$$
$$+\frac{1}{2}\left(\delta^i{}_j\partial_k\partial^k h - \partial_k\partial^k h^i{}_j\right) + \frac{1}{2}\delta^{ik}\left(\partial_k\partial_l h^l{}_j + \partial_j\partial_l h^l{}_k - \partial_k\partial_j h\right) - \frac{1}{2}\delta^i{}_j\partial_k\partial_l h^{kl}.$$

The perturbed energy-momentum tensor equations are,

$$T^0{}_0 = -(\rho + \delta\rho), \tag{1.43}$$

$$T^0{}_i = (\rho + P)v_i, \tag{1.44}$$

$$T^i{}_0 = -(\rho + P)v^i, \tag{1.45}$$

$$T^i{}_j = (P + \delta P)\delta^i_j + \Sigma^i{}_j, \tag{1.46}$$

where v_i is the velocity perturbation and $\Sigma^i{}_j = T^i{}_j - \frac{1}{3}\delta^i{}_j T^k{}_k$ is the traceless part of the energy-momentum tensor. Upon substitution of these equations into the Einstein equations, we obtain a list of constraint and evolution equations. We will only be dealing with the scalar perturbations in this work, and so the two scalar constraint equations are,

$$\mathcal{H}\dot{h} - 2k^2\eta = -8\pi G a^2 \delta T^0{}_0 \,, \tag{1.47}$$

$$k\dot{\eta} = 4\pi G a^2 (\rho + P) v^s \,, \tag{1.48}$$

and the two scalar evolution equations are,

$$\ddot{h} + 2\mathcal{H}\dot{h} - 2k^2\eta = -8\pi G a^2 \delta T^i{}_i \,, \tag{1.49}$$

$$\ddot{h} + 6\ddot{\eta} + 2\mathcal{H}(\dot{h} + 6\dot{\eta}) - 2k^2\eta = -24\pi G a^2 (\rho + P)\Theta^s \,, \tag{1.50}$$

where,

$$(\rho + P) v^s \equiv i k^j \delta T^0{}_j \,, \tag{1.51}$$

$$(\rho + P)\Theta^s \equiv -\left(\hat{k}_i \hat{k}_j - \frac{1}{3}\delta_{ij}\right)\Sigma^i{}_j \,. \tag{1.52}$$

The perturbed part of the energy-momentum conservation equation $\delta\left(\nabla_\mu T^{\mu\nu}\right) = 0$ is,

$$\delta\left(\nabla_\mu T^{\mu\nu}\right) = \partial_\mu \delta T^{\mu\nu} + \delta\Gamma^\nu_{\alpha\beta} T^{\alpha\beta} + \Gamma^\nu_{\alpha\beta}\delta T^{\alpha\beta} + \delta\Gamma^\alpha_{\alpha\beta} T^{\nu\beta} + \Gamma^\alpha_{\alpha\beta}\delta T^{\nu\beta} = 0 \,, \tag{1.53}$$

and from this we arrive at the equations describing the time evolution of the density contrast and velocity perturbation, which in the synchronous gauge are given by,

$$\dot{\delta} = -(1+w)\left(k v^S + \frac{1}{2}\dot{h}\right) - 3\mathcal{H}\left(c_s^2 - w\right)\delta \,, \tag{1.54}$$

$$\dot{v}^S = -\mathcal{H}(1 - 3w) v^S - \frac{\dot{w}}{1+w} v^s + c_s^2 \frac{1}{1+w} k\delta - k\Theta^S \,, \tag{1.55}$$

where we define a sound speed, $c_s^2 \equiv \delta P/\delta\rho$. Weller and Lewis (2003) and Bean and Doré (2004) defined the sound speed to be in the frame comoving with the fluid, and redefined δ to be $\delta \equiv \delta_{\rm rest} + 3\mathcal{H}(1+w)v^S/k$ in order to apply in an arbitrary frame. The equations of motion now become,

$$\dot{\delta} = -(1+w)\left(kv^S\left[1+\frac{9\mathcal{H}^2}{k^2}(c_s^2-w)\right]+\frac{1}{2}\dot{h}\right) - 3\mathcal{H}\left(c_s^2-w\right)\delta\,, \tag{1.56}$$

$$\dot{v}^S = -\mathcal{H}\left(1-3w\right)v^S + c_s^2\frac{1}{1+w}k\delta\,, \tag{1.57}$$

where we have assumed no anisotropic stress, and constant w.

1.4 Energy density components

We now turn our attention to the components that contribute to the energy-momentum tensor, $T_{\mu\nu}$, in our Universe. We can place these components into the following four categories, baryonic matter, radiation, dark matter, and dark energy. The two more familiar components are baryonic matter and radiation. Everything we see and touch is composed of baryonic matter, and it is radiation, in the form of photons that allow us to interact and see the baryonic world. The study of cosmology has identified two other components, which we are unaware of in our everyday existence. Dark matter, an as yet unknown form of matter, that doesn't appear to interact through the electromagnetic (EM) force, and dark energy, a component that is responsible for the accelerated expansion of the Universe.

1.4.1 Baryons and Cold Dark Matter

Baryons, which in the cosmological sense include electrons since their relative mass is so small, make up our visible Universe. The majority of the baryonic matter in our Universe is found in diffuse hot gas within galaxy clusters. This matter has been heated due to the gravitational forces induced by the cluster, allowing the gas to be

viewed in the X-ray part of the EM spectrum. In fact there is thought to be 5 to 10 times the amount of baryonic matter contained within intergalactic gas than contained within stars (Liddle (2003)). The abundance of light elements created during big bang nucleosynthesis is sensitive to the total baryon mass. Therefore study of the light elements can constrain the total baryon density, which is found to be roughly 5% of the critical density (Burles et al. (2001)). WMAP7, which is the year 7 results from the Wilkinson Microwave Anisotropy Probe (WMAP) mission, finds that for a ΛCDM model, $\Omega_b = 0.0449 \pm 0.0028$ (Jarosik et al. (2011)).

As well as baryonic matter, there is evidence that points to a non baryonic type of matter which only interacts with the rest of the Universe via gravity. Cold dark matter (CDM) is the most popular candidate for this extra component, where the term cold refers to the fact that the fluid was non-relativistic at the time of photon decoupling. The topic of the missing mass goes back to the 1930's, when Zwicky and Oort independently found evidence that the mass observed was less than the mass inferred through gravitational effects. As an example, one can look at galaxy rotation curves, which chart the rotation speed of galaxies with respect to distance from the centre. Using Kepler's law we can write this tangential velocity, v, at radius R, with respect to the mass, M, contained within R,

$$v = \sqrt{\frac{GM(R)}{R}}, \tag{1.58}$$

where G is Newton's gravitational constant. At large radii, one would expect that velocity to fall off as the inverse square root of R. In fact what is observed is the velocity becomes constant, suggesting that even when outside the visible part of the galaxy, there is still more unseen mass. There are several methods to pinning down how much of the Universe is made up of CDM, ranging from CMB anisotropies observations, Pryke et al. (2002), to measuring the ratio of baryonic matter to CDM, Grego et al. (2001). Such observations suggest that $\sim 23\%$ of the critical density is in the form of CDM (see also Turner (2002)). WMAP7 best fit parameters for a ΛCDM model put

$\Omega_{CDM} = 0.222 \pm 0.026$ (Jarosik et al. (2011)).

In cosmology matter is described as a pressureless fluid, and thus has an equation of state, $w = 0$. Referring to the fluid equation, (1.5), it is straight forward to show that $\rho_m \propto a^{-3}$, or in terms of the density parameter, $\Omega_m(t) = \Omega_m a^{-3}$, where Ω_m is the present day value. Substituting this into the Friedmann equation, (1.4), we can relate the scale factor to time, which in a universe only containing matter is,

$$a = \left(\frac{t}{t_0}\right)^{\frac{2}{3}} , \tag{1.59}$$

and,

$$H = \frac{2}{3t} . \tag{1.60}$$

A flat universe only containing matter will expand forever, but the rate at which it expands will decrease with time.

1.4.2 Radiation

The Universe is bathed in radiation, made up mainly from photons that originated from the surface of last scattering. The CMB is comprised of these photons, and has a temperature of 2.725 ± 0.002K, Mather et al. (1999), with a black body spectrum. Knowing the temperature of the radiation allows us to calculate the energy density, via,

$$\rho_\gamma = \frac{\pi^2}{15} T_\gamma^4 . \tag{1.61}$$

Relating this to the critical density, the density parameter for radiation is then,

$$\Omega_\gamma = \frac{2.47 \times 10^{-5}}{h^2} . \tag{1.62}$$

We also need to include neutrinos when discussing radiation in the cosmological context. Neutrinos are very weakly interacting particles, that only interact through the weak, and gravitational forces. At some point the early Universe will have been so

hot and dense that even the neutrinos will have been in thermal equilibrium with all other particles in the Universe. As the Universe expanded, the neutrino energy density dropped and decoupled from the rest of the Universe. At this point the neutrinos were now able to travel through the Universe freely and no longer interacted with the matter and photons. The temperature of the Universe will have continued to drop, and once lower than the mass of the electron, the positrons will have annihilated with the electrons, transferring heat to the photons. Since this occurred after the neutrinos had decoupled, they do not feel the effects of this process, and therefore the photons receive a boost in temperature relative to the neutrinos. We can predict the background neutrino temperature, T_ν, from the fact that the ratio of the present value of T_ν to T_γ, is equal to the ratio of T_γ before the electron-positron boost and T_γ afterward. The ratio is given as,

$$\frac{T_\nu}{T_\gamma} = \left(\frac{4}{11}\right)^{1/3} . \tag{1.63}$$

Since T_γ is measured to be 2.725 K, the neutrino temperature should be 1.95 K. Recalling that the energy density goes as the power of four of temperature, the energy density contribution from the neutrinos to $\Omega_{\rm rad}$ is then,

$$\Omega_\nu = 3 \times \frac{7}{8} \times \left(\frac{4}{11}\right)^{4/3} \Omega_\gamma = 0.68\Omega_\gamma \, , \tag{1.64}$$

where (1.64) takes into account the fact that there are three neutrino species, and the 7/8 term comes from the fact that neutrinos are Fermions, not Bosons like photons. The value of $\Omega_{\rm rad}$ is then the sum of the photon and neutrino contributions, $\Omega_{\rm rad} = 4.15 \times 10^{-5} h^{-2}$. Radiation has an equation of state, $w = \frac{1}{3}$, and so $\rho_{\rm rad} \propto a^{-4}$. Substituting this into the Freidmann equation gives,

$$a = \left(\frac{t}{t_0}\right)^{\frac{1}{2}} , \tag{1.65}$$

and,

$$H = \frac{1}{2t}\,. \tag{1.66}$$

A flat universe containing only radiation would also expand forever, albeit at a slower rate than a matter dominated universe. As the Universe expands, photon's wavelengths are stretched, leading to the extra a^{-1} term in $\rho_{\rm rad}$. Therefore a universe with a mixture of just matter and radiation, would always become matter dominated at some time.

1.4.3 Dark Energy

If we were to assume that the Universe was matter dominated with $\Omega_m = 1$, then the age of the Universe would be given by $t = 2/3H_0$, which if $H_0 \approx 70\text{km}\,\text{s}^{-1}\,\text{Mpc}^{-1}$, would equal $\approx$ 9 Gyr. This is in contradiction with other measurements of the age of the Universe. For example, the lifetime of a star is directly linked to its mass. A star with a greater mass will burn its fuel at a greater rate, and as a result have a shorter life. In contrast a lower mass star will have a considerably longer life. For reference our own sun, a G-type main sequence star, is thought to have a life span of $\approx$ 9 Gyr. Measuring the oldest stars in the Universe can give a lower bound on its age. Since all the stars in a globular cluster were created around the same time, they make good cosmic clocks, with the oldest globular clusters containing only contain low mass stars. Numerous globular clusters have been dated (see for example Hansen et al. (2002), Puzia (2002), Jimenez and Padoan (1996), Krauss (2003)), with some appearing to be as old as 16 Gyr which directly rules out a universe with $\Omega_m = 1$. Since the Universe is measured to be almost flat, and best estimates of the matter density are much lower than the critical density, there must be a large amount of energy density, around 70% of the critical density, missing.

By directly probing the expansion Riess et al. (1998), and Perlmutter et al. (1999) recently observed that the Universe has begun to undergo an epoch of accelerated expansion, which is direct evidence for dark energy. These groups made observations of the apparent magnitudes of a number of type Ia supernovae. It is assumed that type Ia

supernovae are standard candles, that is they have a known absolute magnitude which is independent of their location within the Universe and therefore comparing the apparent and absolute magnitude yields an estimate of the distance of a given supernova. This can then be compared against the redshift of the host galaxy measured using spectroscopy. If the Universe is experiencing an accelerated rate of expansion, the energy density component responsible must have a negative pressure. By considering the acceleration equation, equation (1.7), it is clear that such a component must have an equation of state with $w \lesssim -1/3$. The simplest, and most aesthetically pleasing, is a cosmological constant, Λ, which has $w = -1$.

A cosmological constant first appeared in Einstein's field equations in order to artificially keep the Universe static, and while later he considered it a mistake and dropped it from the field equations, it has since been brought back to explain the late time acceleration of the Universe. A cosmological constant is homogeneous and isotropic, and while its effect would have been negligible in the early Universe, as the energy density of the radiation and matter components decay, it will eventually become the dominant component. We can define $\Omega_\Lambda = \Lambda/3H_0^2$, and so the Friedmann equation becomes,

$$H^2(t) = H_0^2 \left(\Omega_m a^{-3} + \Omega_{rad} a^{-4} + \Omega_\Lambda\right) . \tag{1.67}$$

A ΛCDM model, with $\Omega_\Lambda \approx 0.7$ gives a very good fit to a wide range of observations. Large deviations from this model are limited by data from the WMAP mission. In Komatsu et al. (2009) the authors, using a combination of data from WMAP, baryonic acoustic oscillations (BAO) and Type Ia supernova observations, found a constraint on the equation of state to be $-1.14 < w < -0.88$. Using measurements of the X-ray gas mass fraction in 42 X-ray luminous galaxies, Allen et al. (2008) found the equation of state to be, $w = -1.14 \pm 0.31$. When they combined this data with CMB and type Ia supernova (SNIa) data, they found $w = -0.98 \pm 0.07$. Hicken et al. (2009) found that by combining CfA3 SNIa data with that of the Union set (Kowalski et al. (2008)), and combining with a BAO prior, the bounds on the equation of state to be $1+w = 0.013^{+0.066}_{-0.068}$. Both results are consistent with a cosmological constant. A ΛCDM

universe will become dominated by the Λ component eventually, at which point such a universe will undergo accelerated expansion which will last forever.

There are problems with a cosmological constant, however, which leave the door open for a wide range of other dark energy models. There is no fundamental theory that allows us to derive the energy density of the cosmological constant. Currently, particle physicists estimate the value for the energy density to be many orders of magnitude from the observed value (for example, Weinberg (1989) and Bertolami (2009)). A second problem is the coincidence problem, which asks why are the matter and dark energy densities currently very similar. A cosmological constant's energy density would have been negligible in the early Universe next to the matter energy density. Since $\rho_m \propto a^{-3}$, the cosmological constant is going to become totally dominant in the not too distant future. To be living in an epoch where they are very similar is considered by some to be a huge coincidence. The coincidence problem can be alleviated somewhat by anthropic considerations. If the Universe was not the way it is currently, then we may not be here to observe it, thus perhaps we should not be surprised by dark energy's current energy density.

1.5 CMB anisotropies

The CMB is the earliest snap shot of the Universe we have. It is isotropic to 1 part in 100,000, has the most perfect black body spectrum ever observed in nature (White (1999)), and its intensity peaks in the microwave range. According to the hot big bang model, after an inflationary period the early Universe would have been filled with a "cosmic gas" of high energy particles all coupled together in thermal equilibrium. Quantum fluctuations before inflation will have been amplified, leading to regions in the cosmic gas having different densities. As the Universe expanded this cosmic gas would have cooled and the energies of the particles would have fallen. When the Universe reached a temperature of $\sim$ 5eV, the electrons had lost enough energy and began combining with protons, forming hydrogen, without the reverse process occur-

ring. The temperature continued to fall and at about $\sim$ 0.25eV the photons decouple from the matter and started to travel through the Universe freely, an epoch known as photon decoupling. These photons are said to have been emitted from the surface of last scattering. This happened at a redshift $z \sim 1100$ and it is these photons that make up the CMB, which due to continual expansion of the Universe now has a temperature of 2.725K. What makes the CMB so valuable are the angular correlations in the temperature and polarisation anisotropies. The most comprehensive study of the CMB has been made using WMAP, which measured the temperature of the CMB at different points on the sky. The temperature autocorrelation function can then be calculated,

$$C(\theta) = < \left(\frac{\Delta T}{T}\right)_1 \left(\frac{\Delta T}{T}\right)_2 > , \tag{1.68}$$

where the subscripts 1 and 2 refer to two positions on the sky subtended by and angle θ. $C(\theta)$ can be expanded in a multipole expansion,

$$C(\theta) = \sum_{l=2}^{\infty} \frac{2l+l}{4\pi} C_l \mathcal{P}_l(\cos\theta) , \tag{1.69}$$

where l is the wave number, $\mathcal{P}_l(\cos\theta)$ are the Legendre polynomials, and C_l is the angular power spectrum. The peaks and troughs in this power spectrum are created due to a variety of effects, and it is these features that can tell us a huge amount about our Universe.

In the early Universe, the cosmic gas was filled with density perturbations which had been seeded by initial quantum fluctuations. Perturbations within the horizon oscillated with time due to the competing effects of gravity, trying to compress an overdense region, and the photon pressure, trying to oppose the compression. Photons leaving the surface of last scattering from an overdense region will have to climb out of a potential well, and thus be redshifted relative to a photon emanating from an underdense region. Photons leaving an overdense region will have a higher energy initially than a photon leaving an underdense region due to the fact that higher density regions will be hotter. Also, a photon emanating from a perturbation that possesses a pecu-

liar velocity relative to us will exhibit a Doppler shift. These competing effects are recorded on the CMB, and allow us to constrain different cosmological parameters.

The Sachs-Wolfe plateau is the fairly flat part of the power spectrum, located at large angular scales, $l \lesssim 100$. On such large scales no oscillations occurred in the cosmic gas since the associated Fourier modes hadn't re-entered the horizon. Therefore $\Delta T/T$ is purely due to the gravitational potential, Φ, of "frozen in" perturbations and is equal to $\Delta T/T = \Phi/3$. Between $100 \lesssim l \lesssim 1000$ are the acoustic peaks corresponding to the velocity and density perturbations at the surface of last scattering. The odd peaks correspond to Fourier modes that were overdensities at photon decoupling, the first peak being at $l \sim 220$, and the even peaks correspond to underdensities. The power falls off at large l due to Silk damping. Recombination happens over a finite timescale meaning the surface of last scattering has a width. For $l \gtrsim 1000$ these anisotropies are on a smaller scale than the width of the surface of last scattering, and are suppressed.

These anisotropies are primary anisotropies, and show how the CMB was at the surface of last scattering. The photons have travelled a long way across the Universe on their way to us, passing objects that have modified them, creating secondary anisotropies in the measured CMB. These effects include the Integrated Sachs Wolfe (ISW) effect which is dependent on dark energy parameters, making it an ideal observation for constraining cosmological parameters. Varying the dark energy equation of state, w_{DE} changes the rate of expansion in the universe and thus will change the way the temperature-temperature (TT) power spectrum looks. Shifting w_{DE} towards a value larger than -1, shifts the angular power spectrum features towards larger angular scales. The effect of varying w_{DE} is degenerate with varying the total energy density Ω. The measurements taken of the different angular power spectra can be compared with theoretical results from programs such as CMBFAST and CAMB, which evolve the Einstein equations, and component equations of motion, for a range of initial starting parameters, outputting a range of different power spectra. Assuming a ΛCDM model, WMAP7 finds the following best fit results, $\Omega_m = 0.266 \pm 0.029$, $\Omega_{DE} = 0.734 \pm 0.029$, $h = 0.710 \pm 0.025$, $z_{dec} = 1088.2 \pm 1.2$, $n_s = 0.963 \pm 0.014$, $\tau = 0.088 \pm 0.015$ and

$\Delta^2_{\mathcal{R}} = (2.43 \pm 0.11) \times 10^{-9}$. Where n_s is the scalar spectral index, τ is the reionization optical depth and $\Delta^2_{\mathcal{R}}$ is the curvature fluctuation amplitude. Using these parameters, and the CMB code CMBFAST, we have plotted a ΛCDM TT power spectrum, shown in figure 1.1 for illustration.

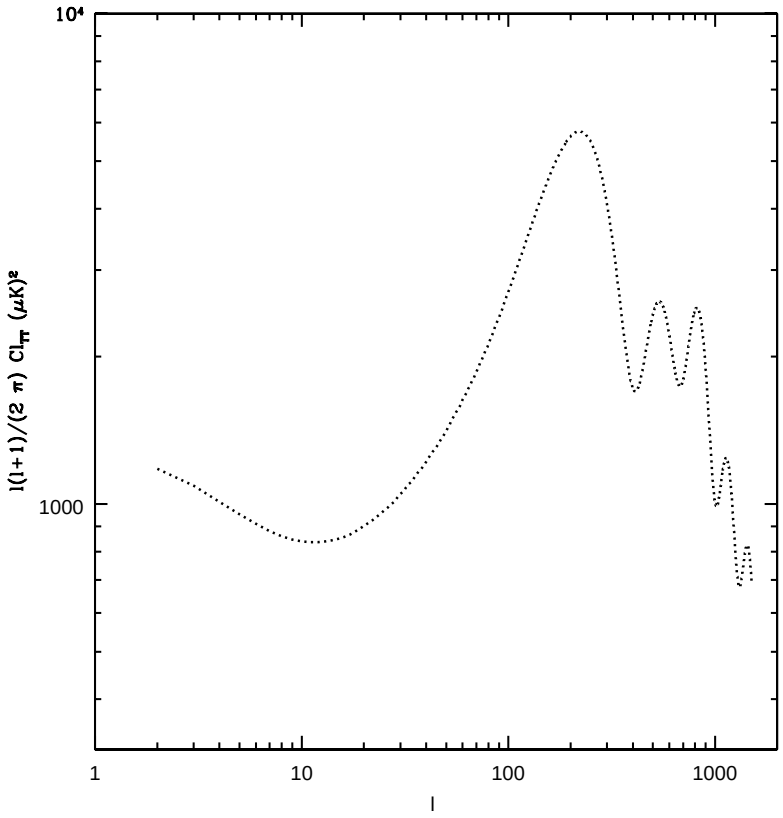

Figure 1.1: TT power spectrum for a ΛCDM model, with the following values of cosmological parameters, $\Omega_m = 0.266$, $\Omega_{DE} = 0.734$, $h = 0.71$, $z_{dec} = 1088.2$, $n_s = 0.963$, $\tau = 0.088$ and $\Delta^2_{\mathcal{R}} = 2.43 \times 10^{-9}$. The ISW effect is responsible for the raised power at $l \lesssim 10$.

1.6 Dark energy models

With no fundamental theory of dark energy, there has been a wide variety of different theories proposed in order to explain the observed acceleration of the Universe, other than a cosmological constant.

1.6.1 Quintessence

A popular alternative to a cosmological constant is a quintessence model, described by a scalar field ϕ and a potential $V(\phi)$. The energy-momentum tensor for a scalar field is given by,

$$T_{\mu\nu} = \partial_\mu\phi\partial_\nu\phi - g_{\mu\nu}\left(\frac{1}{2}g^{\alpha\beta}\partial_\alpha\phi\partial_\beta + V(\phi)\right). \tag{1.70}$$

Using equation (1.70) for a flat FRW universe and assuming $\phi = \phi(t)$, we find that,

$$\rho = \frac{1}{2}\dot{\phi}^2 + V(\phi)\,, \tag{1.71}$$

$$P = \frac{1}{2}\dot{\phi}^2 - V(\phi)\,. \tag{1.72}$$

The Hubble and acceleration equations then become,

$$H^2 = \frac{8\pi G}{3}\left(\frac{1}{2}\dot{\phi}^2 + V(\phi)\right), \tag{1.73}$$

$$\frac{\ddot{a}}{a} = -\frac{8\pi G}{3}\left(\dot{\phi}^2 - V(\phi)\right). \tag{1.74}$$

We can see from equation (1.74) that for an accelerated rate of expansion $\dot{\phi}^2 < V(\phi)$.

The equation of state for a scalar field is then given by,

$$w_\phi = \frac{P}{\rho} = \frac{\dot{\phi}^2 - V(\phi)}{\dot{\phi}^2 + V(\phi)}\,, \tag{1.75}$$

noting that $-1 \leq w_\phi \leq 1$. Then from the fluid equation (1.5),

$$\rho = \rho_0 \exp\left(-\int 3(1+w_\phi)\frac{da}{a}\right). \tag{1.76}$$

We know from the fluid equation that for an accelerated expansion, $w \leq -1/3$, and putting this together with equation (1.76) we find that for a scalar field, $\rho \propto a^{-b}$ where $0 \leq b < 2$. In the case where $V(\phi) \gg \dot{\phi}^2$, the slow roll limit, the equation of state is $w_\phi \approx -1$, and so to match observation, a scalar field will need to be slowly rolling down its potential.

An advantage of quintessence models over Λ models is quintessence can exhibit tracking behaviour with a specific potential, see for example Zlatev et al. (1999) and Steinhardt et al. (1999). A tracker model is a scalar field that is insensitive to the initial conditions. During the early radiation dominated Universe the scalar field can have a huge range of initial energy densities. The field however tracks the radiation density until matter radiation equality. Therefore two initial conditions several orders of magnitude apart will converge on the same value of energy density by matter radiation equality. Once this epoch is reached the scalar field density becomes the dominant component in the Universe and starts behaving as it is observed today. Such a model alleviates the fine tuning problem suffered by the cosmological constant.

1.6.2 Elastic dark energy

The elastic dark energy model treats the dark energy as a fluid, much like the treatment of the other components of the energy-momentum tensor, however allowing for the fluid to have rigidity and can thus be regarded as analogous to an elastic solid. The topic of elastic dark energy is discussed in depth in Battye and Moss (2007), here we briefly outline the model.

The model was originally motivated when considering frustrated networks of topological defects, such as domain walls or cosmic strings, as a candidate for dark energy. However the topic of an elastic dark energy can be studied on its own from a

phenomenological point of view. The energy-momentum tensor for a perfect elastic medium takes the form,

$$T^{\mu\nu} = \rho u^{\mu} u^{\nu} + P^{\mu\nu} \,, \tag{1.77}$$

where u^{μ} are the flow vectors, with $u^{\mu}u_{\mu} = -1$, and the $P^{\mu\nu}$ is the pressure tensor. The Lagrangian variation of this energy-momentum tensor is given by,

$$\delta_L T^{\mu\nu} = -\frac{1}{2}\left(W^{\mu\nu\rho\sigma} + T^{\mu\nu} g^{\rho\sigma}\right) \delta_L g_{\rho\sigma} \,. \tag{1.78}$$

Here $W^{\mu\nu\rho\sigma}$ is the non-orthogonal elasticity tensor, which can be decomposed as,

$$W^{\mu\nu\rho\sigma} = E^{\mu\nu\rho\sigma} + P^{\mu\nu} u^{\rho} u^{\sigma} + P^{\rho\sigma} u^{\mu} u^{\nu} - P^{\mu\rho} u^{\sigma} u^{\nu} - P^{\mu\sigma} u^{\rho} u^{\nu} - P^{\nu\sigma} u^{\rho} u^{\mu} - P^{\nu\rho} u^{\sigma} u^{\mu} - \rho u^{\mu} u^{\nu} u^{\rho} u^{\sigma} \,. \tag{1.79}$$

$E^{\mu\nu\rho\sigma}$ is the elasticity tensor, satisfying,

$$E^{\mu\nu\rho\sigma} = E^{(\mu\nu)(\rho\sigma)} = E^{\rho\sigma\mu\nu} \,, \tag{1.80}$$

and,

$$E^{\mu\nu\rho\sigma} u_{\sigma} = 0 \,. \tag{1.81}$$

The difference between the Lagrangian (moving with the perturbation) variation, δ_L, and the Eulerian (fixed with respect to a background) variations is $\delta_L = \delta_E + \mathcal{L}_{\xi}$, and hence the Lagrangian variation of the metric tensor is,

$$\delta_L g_{\mu\nu} = \delta_E g_{\mu\nu} + 2\nabla_{(\mu}\xi_{\nu)} \,, \tag{1.82}$$

and ξ^{μ} is the infinitesimal displacement field. In order to arrive at the equation of motion for the displacement field, one must evaluate the Lagrangian variation, $\delta_L(\gamma^{\mu}_{\nu}\nabla_{\mu}T^{\mu\nu}) = 0$, which gives,

$$\left(A^{\mu(\nu}{}_{\rho}{}^{\sigma)} - (\rho\gamma^{\mu}{}_{\rho} + P^{\mu}{}_{\rho})u^{\nu}u^{\sigma}\right)\delta_L\Gamma^{\rho}{}_{\nu\sigma} + \frac{1}{2}\gamma^{\mu}{}_{\rho}\gamma^{\alpha}{}_{\nu}\gamma^{\beta}{}_{\sigma}(\delta_L g_{\alpha\beta})\nabla_{\tau}E^{\rho\tau\nu\sigma} = \left(P^{\mu\nu}\dot{u}^{\sigma} - \frac{1}{2}P^{\nu\sigma}\dot{u}^{\mu} - 2A^{\mu(\nu}{}_{\rho}{}^{\tau)}\nu^{\rho}{}_{\tau}u^{\sigma} + (\rho\gamma^{\mu}{}_{\rho} + P^{\mu}{}_{\rho})\dot{u}^{\rho}u^{\nu}u^{\sigma}\right)\delta_L g_{\nu\sigma}\,. \tag{1.83}$$

Here the dots now represent $u^{\mu}\nabla_{\mu}$, covariant differentiation with respect to the flow, and $A^{\mu(\nu}{}_{\rho}{}^{\sigma)}$ is the relativistic Hadamard elasticity tensor, given by,

$$A^{\mu(\nu}{}_{\rho}{}^{\sigma)} = E^{\mu(\nu}{}_{\rho}{}^{\sigma)} - \gamma^{\mu}{}_{\rho}P^{\nu\sigma}\,, \tag{1.84}$$

and $\gamma_{\mu\nu} = g_{\mu\nu} + u_{\mu}u_{\nu}$. For an isotropic perfect elastic medium, the pressure tensor is given by, $P^{\mu\nu} = P\gamma^{\mu\nu}$ and the elasticity tensor can be written as,

$$E^{\mu\nu\rho\sigma} = \Sigma^{\mu\nu\rho\sigma} + (\beta - P)\gamma^{\mu\nu}\gamma^{\rho\sigma} + 2P\gamma^{\mu(\rho}\gamma^{\sigma)\nu}\,, \tag{1.85}$$

where $\Sigma^{\mu\nu\rho\sigma}$ is the shear tensor, obeying the same symmetry and orthogonality conditions as the elasticity tensor, and β is the bulk modulus. The shear tensor can be written in terms of the shear modulus, μ, where for a perfect fluid, $\mu = 0$, giving,

$$\Sigma^{\mu\nu\rho\sigma} = 2\mu\left(\gamma^{\mu(\rho}\gamma^{\sigma)\nu} - \frac{1}{3}\gamma^{\mu\nu}\gamma^{\rho\sigma}\right). \tag{1.86}$$

We can now combine these equations and substitute them into equation (1.78), given the perturbed energy-momentum tensor components,

$$\delta T^{0}{}_{0} = (\rho + P)\left(\partial_i\xi^i + \frac{1}{2}h\right), \tag{1.87}$$

$$\delta T^{i}{}_{0} = -(\rho + P)\dot{\xi}^i\,, \tag{1.88}$$

$$\delta T^{i}{}_{j} = -\delta^{i}{}_{j}\left(\beta - \frac{2}{3}\mu\right)\left(\partial_k\xi^k + \frac{1}{2}h\right) - \mu(2\partial_{(j}\xi^{i)} + h^{i}{}_{j})\,, \tag{1.89}$$

and from equation 1.83, the evolution of ξ^i is,

$$(\rho + P)(\ddot{\xi}^i + \mathcal{H}\dot{\xi}^i) - 3\beta\mathcal{H}\dot{\xi}^i - \beta\left(\partial^i\partial_j\xi^j + \partial^i\frac{h}{2}\right) - \mu\left(\partial^j\partial_j\xi^i + \frac{\partial^i\partial_j\xi^j}{3} + \partial^j h^{i}{}_{j} - \frac{\partial^i h}{3}\right) = 0\,, \tag{1.90}$$

where h is the trace of the metric perturbation $h^{\mu\nu}$. Combining equations (1.43), (1.44), (1.45), (1.46) with equations (1.87), (1.88), and (1.89) gives,

$$\delta\rho = -\rho(1+w)\left(k\xi^S + \frac{1}{2}(h-h_I)\right), \tag{1.91}$$

$$v^S = \dot{\xi}^S, \tag{1.92}$$

$$\delta P = -\rho(1+w)\frac{dP}{d\rho}\left(k\xi^S + \frac{1}{2}(h-h_I)\right), \tag{1.93}$$

$$\Pi^S = \frac{3}{2}\frac{1+w}{w}\Theta = \frac{3}{2}\left(c_S^2 - w\right)(1+w^{-1})\left(-\frac{\delta}{1+w} + 3(\eta-\eta_I)\right). \tag{1.94}$$

From these we arrive at the equations of motion for the elastic dark energy model,

$$\dot{\delta} = -(1+w)\left(kv^S + \frac{1}{2}\dot{h}\right), \tag{1.95}$$

$$\dot{v}^S = -\mathcal{H}\left(1 - 3\frac{dP}{d\rho}\right)v^S + \frac{dP}{d\rho}\frac{1}{1+w}k\delta - \frac{2}{3}\frac{w}{1+w}k\Pi^S. \tag{1.96}$$

1.6.3 Other dark energy models

Since there is no fundamental theory for dark energy, there are a large range of different dark energy models which given the correct parameters, can reproduce the CMB anisotropies using the CMB codes. For example, k-essence is a scalar field model of dark energy which relies on modifications to the kinetic energy, instead of the potential energy, in order to reproduce the accelerated expansion (Malquarti et al. (2003), de Putter and Linder (2007), Armendariz-Picon et al. (2001)). Another fluid based model is the Chaplygin gas dark energy model (Kamenshchik et al. (2001), Bento et al. (2002)). In this model dark energy has an equation of state given by $P = -A/\rho^\alpha$ where A is a positive constant and $0 < \alpha < 1$. At early times a Chaplygin gas exhibits the characteristics of a pressureless gas, while at later times the gas behaves like a cosmological constant. Most models of dark energy set its equation of state greater than or equal to

-1. Since observational evidence doesn't necessarily place $w = -1$ as the lower bound, see for example Komatsu et al. (2009) and Hicken et al. (2009)), it is reasonable to consider the possibility of an equation of state less than -1. One such model is phantom dark energy, where the sum of the density and pressure is negative. The energy density increases with time for a phantom energy model, leading to a Big Rip scenario, where the phantom energy overcomes all other forces of nature (Caldwell et al. (2003)).

Each of these models can predict how such a universe will look at a given time, dependent on, among other things, specific dark energy parameters that may be unique to that model of dark energy. While it is very difficult to say which specific model is a true representation of the actual phenomenon, given no fundamental theory of dark energy, we can compare observations with theoretical predictions, and thus constrain given dark energy parameters.

2

Constraints from weak lensing

In the framework of general relativity freely moving particles travel along geodesics, the shortest path between two points. In the presence of a gravitational potential, this path will appear curved to an external observer. Photons travel along null geodesics, and so when light travels through the Universe its direction is modified when in the vicinity of mass such as galaxies and galaxy clusters. This effect is known as gravitational lensing and is an important tool for cosmology as any deflection that the photons undergo is due solely to the response of the photons to a gravitational field, irrespective of the gravitational source and physical properties.

It was gravitational lensing that gave the first confirmation of the theory of general relativity back in 1919. In a trip to Prncipe off the coast of Africa, Arthur Eddington observed, during a solar eclipse, the angular shift in the position of a star when it was in close proximity to the Sun. Such a shift proved that the mass of the Sun had deflected the light rays from the distant star, and thus confirmed a crucial prediction of general relativity. With this knowledge it became theoretically possible map out the mass overdensities within the Universe, as opposed to measuring light from galaxies to infer galaxy distributions.

2.1 Introduction

Gravitational lensing can be categorized into two distinct types, strong gravitational lensing and weak gravitational lensing. Strong gravitational lensing heavily distorts background sources, producing noticeable distortions such as multiple images, Einstein rings, and arcs within images of clusters. In order to observe strong gravitational lensing images, one must be aligned in such a way that a background source is almost directly behind a foreground source. Weak lensing produces a more subtle effect on a large number of background sources. As the light from the background sources such as distant galaxies traverse the Universe, the photon paths are slightly modified when passing foreground mass. This leads to a slight modification to the observed shape and size of the source. Since we cannot know the intrinsic size, shape and orientation of a given galaxy before it undergoes any distortion, coupled with the fact we don't know exactly where every underdense and overdense region appears on the night sky, many light sources must be analysed and statistical patterns need to be detected. Therefore weak lensing measurements are purely statistical in nature, such as correlation functions and power spectra. Figure 2.1 shows simple representation of what weak lensing can do to a background source. Given that dark energy modifies the matter-matter power spectrum and the distance redshift relation, both of which are related to weak lensing parameters, observations of weak lensing can lead to independent constraints on dark energy parameters.

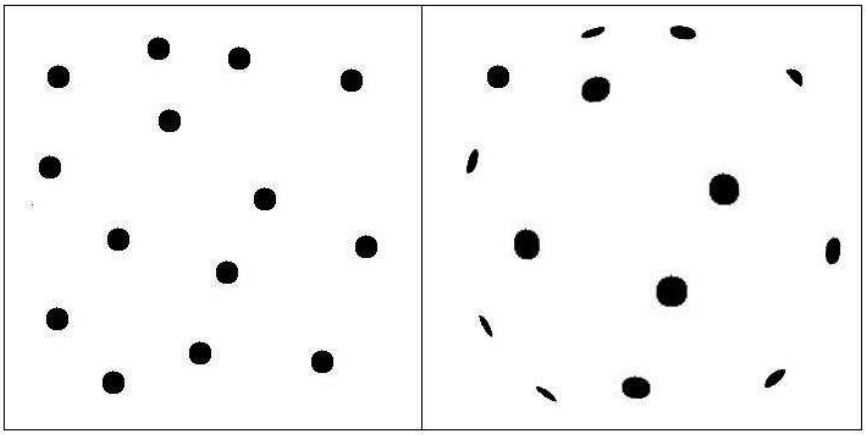

Figure 2.1: The left image shows points representing galaxies in a typical arrangement one may find before any weak lensing effects are added. The right image shows what effect weak lensing would have on the background source. Both shape, and magnification have been modified.

2.2 Weak lensing geodesic equations

So far we have a given a brief qualitative account of weak lensing, but in order to proceed we must have a mathematical description. We follow a similar description given in Dodelson (2003). We start by solving the geodesic equation for a given photon travelling from a background source to us. The geodesic equation, given earlier, (1.15), is,

$$\frac{d^2x^\alpha}{d\lambda^2} = -\Gamma^\alpha_{\beta\gamma}\frac{dx^\beta}{d\lambda}\frac{dx^\gamma}{d\lambda}\,. \tag{2.1}$$

Both the right and left hand side of the geodesic equation (2.1) can be rearranged using the chain rule of differentiation,

$$\frac{d\chi}{d\lambda}\frac{d}{d\chi}\left[\frac{d\chi}{d\lambda}\frac{dx^i}{d\lambda}\right] = -\Gamma^\alpha_{\beta\gamma}\frac{dx^\beta}{d\chi}\frac{dx^\gamma}{d\chi}\frac{d\chi}{d\lambda}\frac{d\chi}{d\lambda}\,, \tag{2.2}$$

where we have only consider the spatial parts of x^α, and split the three spatial parts into radial, $x^3 = \chi$, and traverse, $x^i = \theta^i\chi$, distances. Because we are making use of the

small angle approximation, it follows that any perturbation in the metric multiplied by $\theta^i\chi$ can be taken to be zero. Also note that $d\chi$ is numerically interchangeable with $\pm d\tau$ with the speed of light set to $c = 1$. $d\tau/d\lambda$ can be worked out using the knowledge that, because photons are massless,

$$g_{\alpha\beta}\frac{dx^\alpha}{d\lambda}\frac{dx^\beta}{d\lambda} = 0\,, \tag{2.3}$$

or,

$$g_{\alpha\beta}\frac{dx^\alpha}{d\lambda}\frac{dx^\beta}{d\lambda} = g_{00}\frac{d\tau}{d\lambda}\frac{d\tau}{d\lambda} + g_{ij}\frac{dx^i}{d\lambda}\frac{dx^j}{d\lambda}\,, \tag{2.4}$$

and from this we get, for photons,

$$g_{00}(P^0)^2 + p^2 = 0\,, \tag{2.5}$$

where we have defined $P^0 = \frac{d\tau}{d\lambda}$ and photon momentum $p^2 = g_{ij}\frac{dx^i}{d\lambda}\frac{dx^j}{d\lambda}$. By simple rearrangement we have,

$$P^0 = p(1 - \Psi)\,, \tag{2.6}$$

where Ψ is the temporal perturbation to the metric. There are four possible combinations in the sum on the right of geodesic equation. These are: $\beta = \gamma = 0$; $\beta = 0$, $\gamma = j$; $\beta = j$, $\gamma = 0$; and $\beta = j$, $\gamma = k$. The non zero perturbed Christoffel symbols in the Newtonian gauge are,

$$\Gamma^i_{00} = \partial^i\Psi a^2\,, \tag{2.7}$$

$$\Gamma^i_{0j} = \Gamma^i_{j0} = \mathcal{H}\delta^i_j - \dot{\Phi}\delta^i_j\,, \tag{2.8}$$

$$\Gamma^i_{jk} = \partial^i\Phi a^2\delta_{jk} - \partial_j\Phi\delta^i_k - \partial_k\Phi\delta^i_j\,, \tag{2.9}$$

where Φ is the spatial perturbation in the metric. Putting this all together, the geodesic equation becomes,

$$p^2 \frac{d}{d\chi}\left(\frac{1}{a^2}\frac{d(\chi\theta^i)}{d\lambda}\right) = -\frac{p^2}{a^2}(1-\psi)\left(a^2\partial^i\Psi + a^2\partial^i\Phi + 2\mathcal{H}\frac{d(\chi\theta^i)}{d\chi}\right), \tag{2.10}$$

making use of the fact that $\frac{d(pa)}{d\chi}$ is constant. This reduces to,

$$\frac{d^2(\chi\theta^i)}{d^2\lambda} = -\delta^{ij}\left(\partial_j\Psi + \partial_j\Phi\right). \tag{2.11}$$

In cosmological models where there is an absence of anisotropic stress at late times, $\Psi = \Phi$, and thus the right hand side of equation (2.11) would be $-2\delta^{ij}\partial_j\Phi$. Here we can see that a gravitational perturbation leads directly to a perturbed viewing angle at a given position, whereas a uniform potential ($\nabla\Phi = 0$) leads to $\frac{d(\chi\theta^i)}{d\chi}$ being constant. We can integrate equation (2.11) twice with respect to χ which will allow us to know the original source angle, θ_s, before it was distorted by the gravitational potential.

$$\theta_s^i = -\int_0^\chi d\chi'\left(\partial^i\Psi(\chi') + \partial^i\Phi(\chi')\right)\left(1 - \frac{\chi'}{\chi}\right) + \theta^i. \tag{2.12}$$

The constant from the integration must be the observed angle θ^i as in the absence of any metric perturbations, the source angle θ_s will equal θ^i. Distortions in the shape of a background source can then be characterised by the 2×2 symmetric shear matrix defined as,

$$A_{ij} \equiv \frac{\partial\theta_s^i}{\partial\theta^j} \equiv \begin{pmatrix} 1-\kappa-\gamma_1 & -\gamma_2 \\ -\gamma_2 & 1-\kappa+\gamma_1 \end{pmatrix}, \tag{2.13}$$

where κ is the convergence, describing contractions and dilations which are proportional to the projected mass along the line of sight. The shear, γ, characterises stretching and compression of the image. From equation (2.13) the convergence and shear are given by,

$$\kappa = -\left(\frac{A_{11} + A_{22}}{2}\right) + 1, \tag{2.14}$$

$$\gamma_1 = -\left(\frac{A_{11} - A_{22}}{2}\right), \tag{2.15}$$

$$\gamma_2 = -A_{12}\,. \tag{2.16}$$

From these equations and the fact that the dominant contribution comes from transverse fluctuations, we can write the convergence, $\kappa(\theta)$, caused by a given source at redshift z,

$$\kappa(\theta) = -\frac{1}{2}\int_0^{\chi} d\chi' W(\chi')\left(k^2\Psi(\chi') + k^2\Phi(\chi')\right). \tag{2.17}$$

We have written the Newtonian potentials in Fourier space ($\nabla^2\Phi = -k^2\Phi$), and W(z) is our window function, given by,

$$W(\chi) = \chi\int_{\chi}^{\infty} d\chi' n(\chi')\left(1 - \frac{\chi}{\chi'}\right), \tag{2.18}$$

and $n(z)$ is the normalised source galaxy distribution. Typically in weak lensing literature, late time shear is assumed to be zero, and thus the quantity $k^2\Phi + k^2\Psi = 2k^2\Phi$. This can then be written using the Poisson fluid equation,

$$k^2\Phi = \sum_x \frac{3H_0^2\Omega_x\delta_x}{2a}\,. \tag{2.19}$$

With no knowledge of the intrinsic size and shape of a given background source, our weak lensing observations must be statistical measurements. One such statistical quantity is the convergence auto correlation function,

$$C_{\kappa\kappa} = \langle\kappa(\theta)\kappa(\theta')\rangle\,, \tag{2.20}$$

which, when transformed into multipole space, is defined as,

$$< \kappa_{lm}\kappa_{l'm'} >= \delta_{l_1l_2}\delta_{m_1m_2}P_\kappa(l)\,, \tag{2.21}$$

where $P_\kappa(l)$ is the convergence power spectrum. Limber's approximation ($l \approx k\chi$) allows us to write $P_\kappa(l)$ as,

$$P_\kappa(l) = \sum_x \frac{9H_0^4\Omega_x^2}{4}\int_0^{\chi_s} d\chi \frac{W^2(\chi)}{\chi^2 a^2(\chi)} P_x\left(\frac{l}{\chi};\chi\right). \tag{2.22}$$

where $P_x\left(\frac{l}{\chi};\chi\right)$ is the power spectrum of species x. From the convergence power spectrum several other second order cosmic shear quantities may be calculated. These include the two point correlation functions $\xi_\pm(\theta)$, the aperture mass variance $\langle M_{ap}^2\rangle(\theta)$ and the shear variance $\langle|\overline{\gamma}|^2\rangle(\theta)$.

The two point correlation functions $\xi_\pm(\theta)$ are defined as

$$\xi_\pm(\theta) = \xi_{tt}(\theta) \pm \xi_{\times\times}(\theta)\,. \tag{2.23}$$

where the subscripts tt and $\times\times$ are the tangential and 45° rotated ellipticity correlation functions respectively, which can be directly inferred from observations. They can also be calculated theoretically from the convergence power spectrum via,

$$\xi_\pm(\theta) = \frac{1}{2\pi}\int_0^\infty dl\, l P_\kappa(l) J_{0,4}(l\theta)\,. \tag{2.24}$$

Where θ is the angle separating galaxy pairs and $J_{0,4}$ are Bessel functions of the first kind. The shear variance is defined as the variance of the average shear in circular areas of differing radii on the sky. As pointed out in Schneider et al. (2002), when trying to determine the shear variance directly, gaps in the observational data can make this difficult. The shear variance can however be computed from the measured correlation function, using,

$$\langle|\overline{\gamma}|^2\rangle(\theta) = \int \frac{\vartheta d\vartheta}{\theta^2}\xi_+(\vartheta) S_+\left(\frac{\vartheta}{\theta}\right), \tag{2.25}$$

where,

$$S_+(x) = \frac{1}{\pi}\left(4\arccos\left[\frac{x}{2}\right] - x\sqrt{4-x^2}\right). \tag{2.26}$$

The shear variance can also be calculated using the theoretical convergence power spectrum via Bartelmann and Schneider (2001),

$$\langle|\overline{\gamma}|^2\rangle(\theta) = \frac{1}{2\pi}\int_0^\infty dl P_\kappa(l)\frac{4{J_1}^2(l\theta)}{l\theta^2}\,, \tag{2.27}$$

with J_1 being a Bessel function of the first kind. The shear variance is a low-pass estimate of the convergence power spectrum. The third statistic is the aperture mass, which can be measured experimentally via,

$$M_{ap}(\theta) = \int d^2\vartheta Q(|\vartheta|)\gamma_t(\vartheta)\,, \tag{2.28}$$

where $\gamma_t(\vartheta)$ is the tangential shear relative to the centre of a circular aperture of angular radius θ, and Q is a filter function. Directly observing the aperture mass variance, $\langle M_{ap}^2\rangle$, suffers the same problems as the shear variance. Like the shear variance, the aperture mass variance can be written in terms of the correlation functions,

$$\langle M_{ap}^2\rangle(\theta) = \frac{1}{2}\int\frac{\vartheta d\vartheta}{\theta^2}\left(\xi_+(\vartheta)T_+\left[\frac{\vartheta}{\theta}\right] + \xi_-(\vartheta)T_-\left[\frac{\vartheta}{\theta}\right]\right)\,, \tag{2.29}$$

with,

$$T_+(x) = 576\int_0^\infty\frac{dt}{t^3}J_0(xt)\left[J_4(t)\right]^2\,, \tag{2.30}$$

and,

$$T_-(x) = 576\int_0^\infty\frac{dt}{t^3}J_4(xt)\left[J_4(t)\right]^2\,. \tag{2.31}$$

The aperture mass variance can also be given by the theoretical convergence power spectrum,

$$\langle M_{ap}^2\rangle(\theta) = \frac{1}{2\pi}\int_0^\infty dl P_\kappa(l)\frac{576{J_4}^2(l\theta)}{l^3\theta^4}\,. \tag{2.32}$$

The aperture mass variance is a bandpass estimate of the convergence power spectrum. All three of these measurements are essentially just integrals over the power spectrum but with differing window functions, and therefore probing different parts of the convergence power spectrum. Given the fact that elastic dark energy is a linear theory, we

are constrain to the linear regime, and so shear variance is a better quantity to calculate and compare with observations as the aperture mass is a more localised measurement. One can work down to $\sim 30'$ with shear variance before non-linear effects take over. With the aperture mass non-linear effects become dominate at much larger angles $\sim 80'$ (Fu et al. (2008)).

2.3 Codes to compute weak lensing observables

CMBFAST calculates the temperature autocorrelation function and the polarization power spectra for a given set of cosmological parameters. A typical power spectrum can be computed via,

$$C_l = (4\pi)^2 \int k^2 dk P_\psi(k) |\Delta_a(k, \eta = \eta_0) \Delta_b(k, \eta = \eta_0)| \,, \tag{2.33}$$

where P_ψ is the initial power spectrum, Δ_a and Δ_b are the numerically computed transfer functions. Seljak and Zaldarriaga (1996) showed that the anisotropy term can be split up into a source term and a geometric term, given by,

$$\Delta(k, \mu, \eta_0) = \int_0^{\tau_0} d\tau e^{ik\mu(\tau - \tau_0)} S(k, \mu, \tau) \,, \tag{2.34}$$

where μ is the cosine of the angle separating the incoming photon with the wavenumber k. If one multiplies both sides by the Legendre polynomial $\mathcal{P}_l(\mu)$ and then integrates over μ the following result is obtained,

$$\Delta_l(k, \eta_0) = \int_0^{\tau_0} d\tau S(k, \tau) j_l[k(\eta_0 - \eta)] \,, \tag{2.35}$$

where j_l is the spherical Bessel function. CMBFAST calculates the temperature and polarisation anisotropies in this way, where the only difference between each calculation is what is used for the source. Corasaniti et al. (2005) modified CMBFAST to include a scalar field type dark energy model (see Bean and Doré (2004)), and also added a feature so that the matter-matter and ISW-matter power spectra (see Chapter

3 for more details on the ISW-matter power spectrum) could be calculated by adding new source terms. These terms for matter and ISW are given respectively by,

$$S_M = W(z) b_g \delta_M \,, \tag{2.36}$$

$$S_{ISW} = e^{-\kappa}(\dot{\Phi} + \dot{\Psi}) \,, \tag{2.37}$$

where $W(z)$ is a window function, Φ and Ψ are Newtonian potentials, and b_g is the galaxy bias. The C_l's for the matter-matter, ISW-matter correlations can now be computed via,

$$C_l^{gg} = (4\pi)^2 \int k^2 dk P_\psi(k) |\Delta_{gg}(k, \eta = \eta_0) \Delta_{gg}(k, \eta = \eta_0)| \,, \tag{2.38}$$

$$C_l^{gT} = (4\pi)^2 \int k^2 dk P_\psi(k) |\Delta_{gg}(k, \eta = \eta_0) \Delta_{TT}(k, \eta = \eta_0)| \,. \tag{2.39}$$

We can perform a similar modification in order to calculate the convergence power spectrum (2.22), by defining the source term,

$$S_\kappa = -\frac{1}{2} k^2 (\Phi + \Psi) W(z) \,, \tag{2.40}$$

where $W(z)$ is the window function given in (2.18). In the case where $\Psi = \Phi$, the equation reduces to $-k^2 \Phi W(z)$. This has allowed us to modify CMBFAST to output the convergence power spectrum. We ran the code for a range of different dark energy parameters, using a galaxy distribution given by,

$$n(z) = \frac{z^2}{0.5^3} \exp\left(-\frac{z}{0.5}\right) \,, \tag{2.41}$$

as in Huterer (2002), normalised so,

$$\int_0^\infty n(z) dz = 1 \,. \tag{2.42}$$

In figure (2.2) we have plotted the convergence power spectra for a ΛCDM, scalar field, and elastic dark energy model with a selection of different values for the sound speed

and equation of state. For the other cosmological parameters we used the WMAP7 best fit values. We have also plotted the aperture mass variance and shear variance for each convergence power spectra in figures 2.3 and 2.4 respectively.

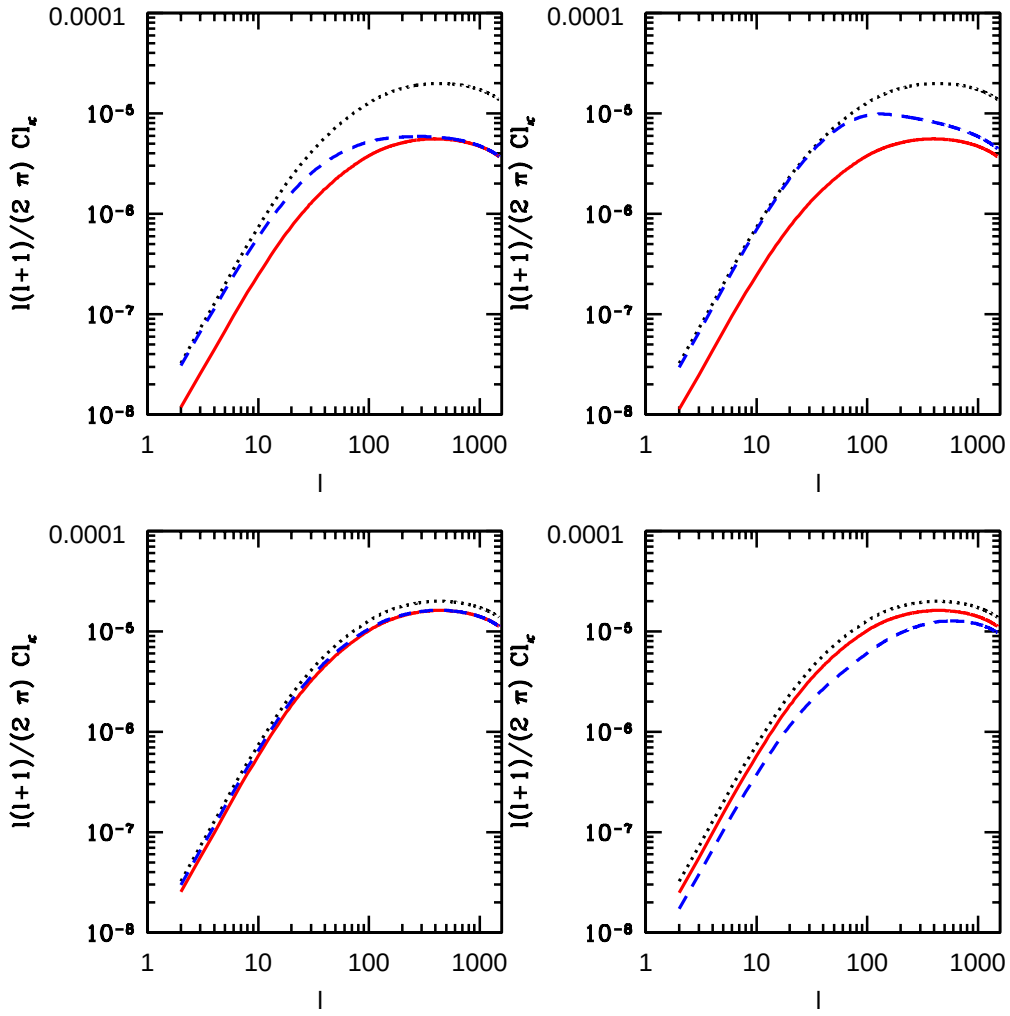

Figure 2.2: These plots show the linear convergence power spectra. The plots on the left are scalar field models and the plots on the right are elastic dark energy model. The plots on the top have $w = -0.4$, the plots on the bottom have $w = -0.8$. The black dotted line in all plots is a ΛCDM model, the blue lines correspond to $c_s^2 = 10^{-4}$, and the red lines to $c_s^2 = 1$.

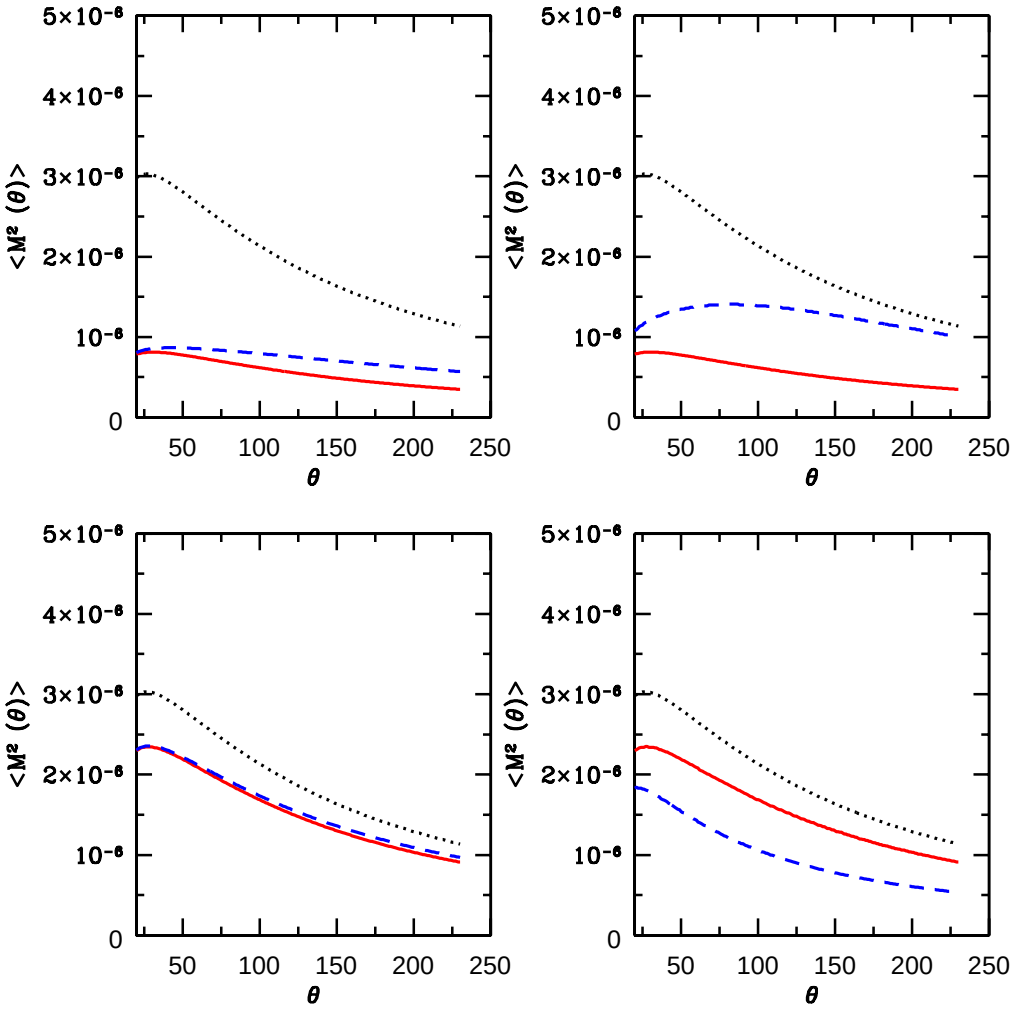

Figure 2.3: These plots show the aperture mass variance, given by equation (2.32). The plots are laid out the same as figure (2.2). θ has units of arcmins.

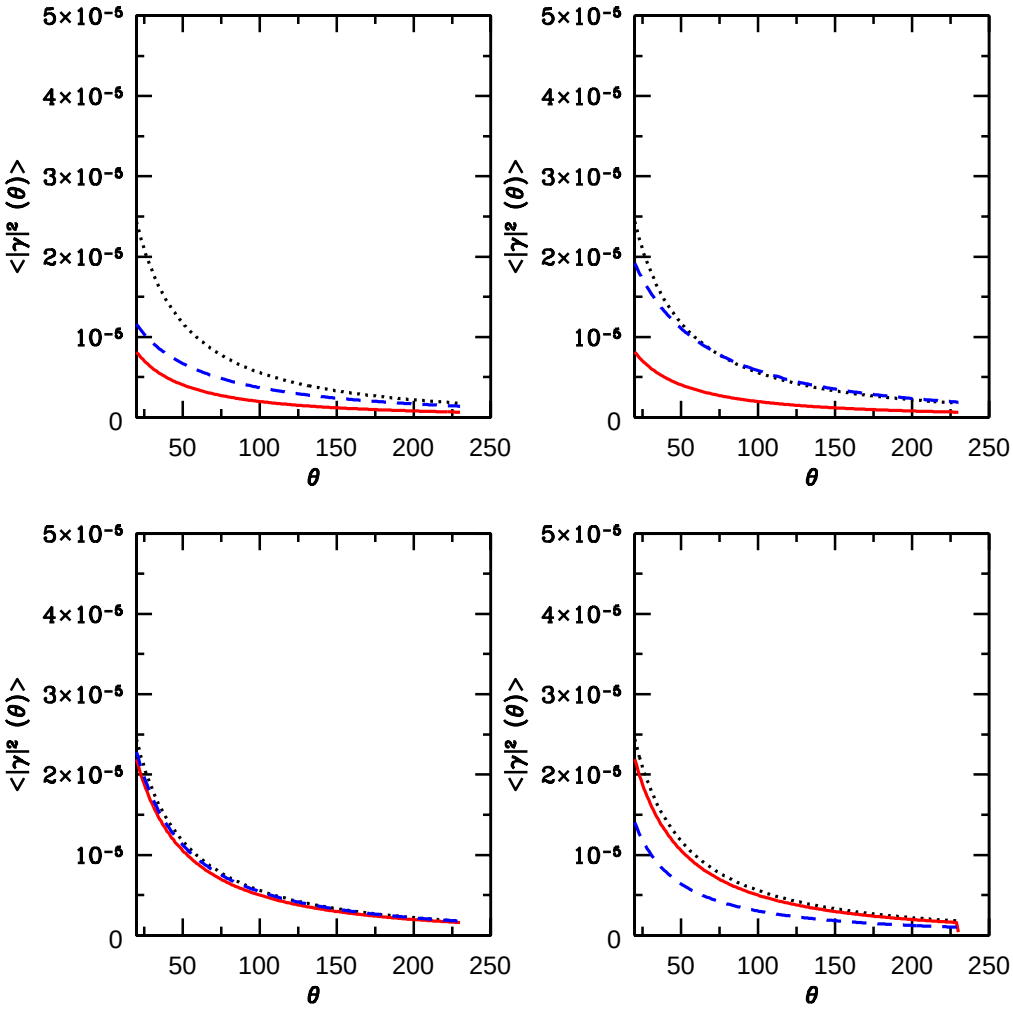

Figure 2.4: These plots show the shear variance, given by equation (2.27). The plots are laid out the same as figure (2.2). θ has units of arcmins.

There is very little between the models when $c_s^2 = 1$, but as the sound speed is lowered, differences start to appear. When the elastic dark energy has an equation of state $w = -0.8$, lowering the sound speed reduces the amplitude of the convergence power spectrum. In the case where $w = -0.4$, the opposite happens, and lower sound speeds lead to larger amplitudes. If we were to only consider $4\pi G\delta_x/3 = -k^2\Phi$ for our weak lensing source, in our convergence equation, then as the sound speed was reduced,

the amplitude would always increase. The reduction at certain values comes from the competing effects of shear and density. Because we are using $\frac{1}{2}k^2(\Phi + \Psi)$ in the convergence equation, with $k^2\Psi = k^2\Phi - 12\pi G a^2\rho(1 + w)\Theta$, and Θ always has the same sign as Φ, meaning $|\Psi|$ is always lower than $|\Phi|$. We have illustrated this effect in figure 2.5, where we have plotted Φ, Ψ and $|\Phi + \Psi|$ for both models. The plots on the left have $c_s^2 = 1$, and show the models are indistinguishable. This explains why there is very little difference in the red lines in figures 2.2, 2.3, and 2.4 between each model, for a given w. The plots on the right of figure 2.5 have $c_s^2 = 10^{-4}$, and now show large differences in Φ and Ψ for the elastic dark energy model. There is no late time difference between the two potentials in the scalar field model as Θ is negligible. The value of $|\Phi + \Psi|$ is larger for elastic dark energy than the scalar field when $w = -0.4$, but the opposite is true for when $w = -0.8$.

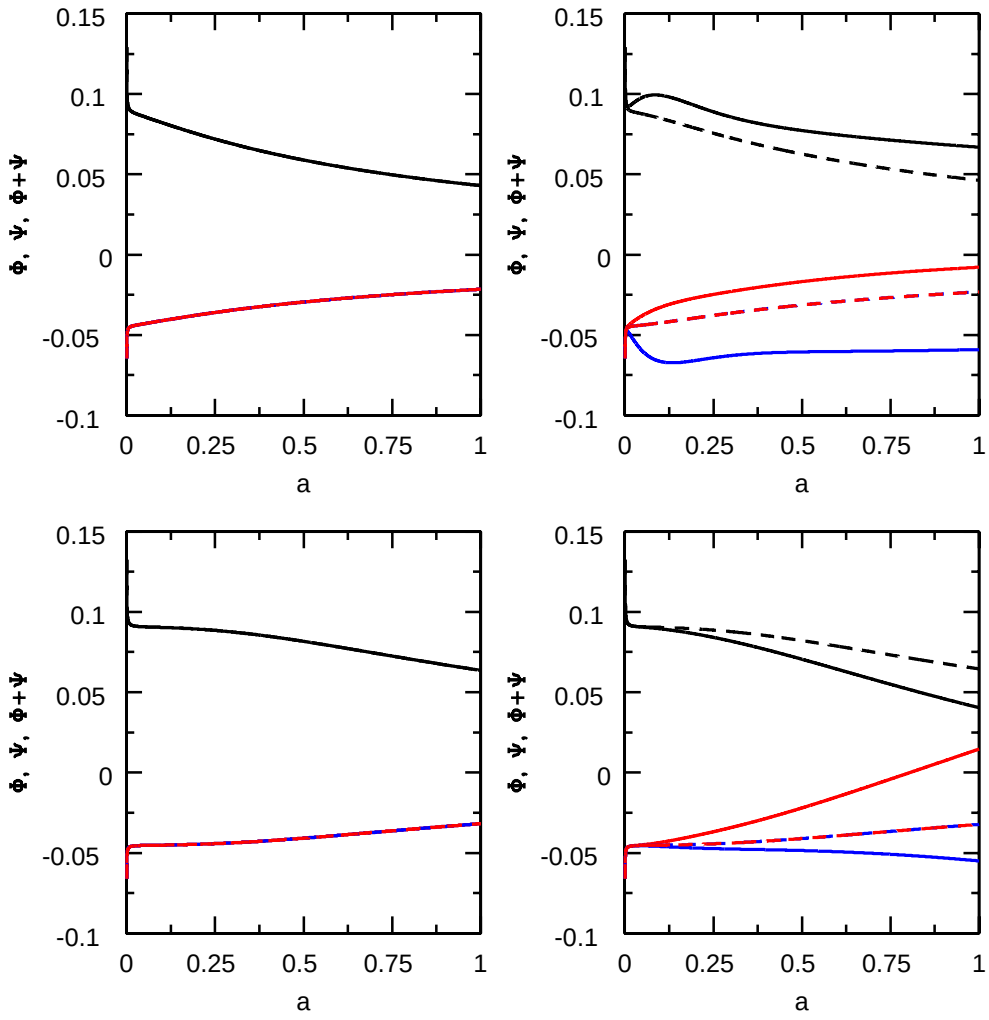

Figure 2.5: These plots demonstrate the evolution of the metric perturbations with respect to the scale factor. The blue lines are Φ, and the red are Ψ. Solid lines denote use of an elastic dark energy model, and dotted lines a scalar field model. The black lines are $|\Phi + \Psi|$. Plots on the left have $c_s^2 = 1$, plots on the right have $c_s^2 = 10^{-4}$. Plots on the top have $w = -0.4$, plots on the bottom have $w = -0.8$.

2.4 CosmoMC results using WMAP5 and SNIa data

We have shown in the last section, using a modified version of CMBFAST, that differences in the convergence power spectrum between elastic dark energy and a scalar field model can occur for certain values of w and c_s. Ultimately we would like to test the theoretical predictions against observed data, and in doing so help constrain these dark energy parameters. We found it useful to put the weak lensing equations into the CMB code, CAMB (Lewis et al. (2000)). Due to the close similarities between CAMB and CMBFAST, it was relatively straight forward to modify CAMB to compute the convergence power spectra and associated correlation functions using the same method. The advantage with CAMB aside from being noticeably quicker than CMBFAST, is that CosmoMC (Lewis and Bridle (2002)) has been written to work with CAMB. Using a Markov Chain Monte Carlo algorithm, CosmoMC runs CAMB many times varying selected cosmological parameters and compares the output to observable data, finding best fit parameters for a given model, and produces marginalized statistics for different cosmological parameters such as w, c_s, Ω_x, h, and n_s. Of particular interest to us are the dark energy parameters, w and the sound speed, c_s. When c_s is ~ 1 it is difficult to distinguish between a scalar field model and an elastic dark energy model as seen in the previous section. As the sound speed approaches zero however, large differences in the power spectra appear and it is these differences that will allow us to constrain the parameters. Given how sensitive elastic dark energy is to low sound speeds, CosmoMC will allow us to define a lower limit to this sound speed, as well as show preferred values of all other parameters for each model.

We ran CosmoMC on the Computation of Mathematical Astrophysics (COMA) cluster at the Jodrell Bank Centre for Astrophysics. COMA is installed with 312 virtual cores, allowing us to run multiple chains on multiple cpus. CAMB was written with multithreading in mind, and by utilising OpenMP, one instance of CAMB can be run over several CPUs, greatly speeding up the computational time. Not only this, since CosmoMC is a hybrid MPI/OpenMP code, we can also run several chains simul-

taneously. Each time we ran CosmoMC we used the API's MPICH2, and OpenMP to run 4 chains, with each chain running on 4 virtual cores, using a total of 16 virtual cores. Using MPI, the code can compare chains as it is running in real time, and check whether the chains are converging.

We ran CosmoMC with the option, MPI Converge Stop = 0.03, enabled. This option checks each of the parameter's "variance of chain means" divided by the "mean of chain variances", An et al. (1998), also known as the Gelman and Rubin R statistic. Typically for convergence one would want $R - 1 < 0.2$. Initially we ran CosmoMC using just WMAP5 data (Dunkley et al. (2009)), and as we expected these showed minimal differences between the elastic dark energy and scalar field model. CosmoMC allows other CMB datasets to be used, including data from the Arcminute Cosmology Bolometer Array Receiver (ACBAR) (Reichardt et al. (2009)), the Cosmic Background Imager (CBI) (Padin et al. (2000)), however since the differences between elastic dark energy and the scalar field model occur at low values of l in the CMB cross correlation functions, smaller angle observations do not aid significantly in distinguishing the two models. Table 2.1 shows the cosmological parameters used with the initial values from our params.ini file. All other options and parameters were left at their default settings.

Parameter	Start Center	Min	Max	Starting Width	σ estimate
$\Omega_b h^2$	0.0223	0.005	0.1	0.001	0.001
$\Omega_c h^2$	0.105	0.01	0.99	0.01	0.01
θ	1.04	0.5	10	0.002	0.002
w	-0.8	-0.999	0	0.02	0.02
n_s	0.95	0.5	1.5	0.02	0.01
$\log[10^{10} A_s]$	3	2.7	4	0.01	0.01
$\log[c_s]$	0	-5	0	0.02	0.02

Table 2.1: Initial cosmological parameters used in all CosmoMC runs, unless otherwise stated.

We used the default CosmoMC installation which imposes priors on H_0 and the age of the Universe as, $40\,\mathrm{km\,s^{-1}\,Mpc^{-1}} < H_0 < 100\,\mathrm{km\,s^{-1}\,Mpc^{-1}}$ and $10\,\mathrm{Gyr} <$ age $<$

20 Gyr. Unless mentioned, we used these settings, and the values in table 2.1 on all CosmoMC runs. 1D and 2D marginalized plots are shown in figures 2.6 and 2.7 in a variety of parameter planes, where we have overlaid scalar field and elastic dark energy contours on the same plots.

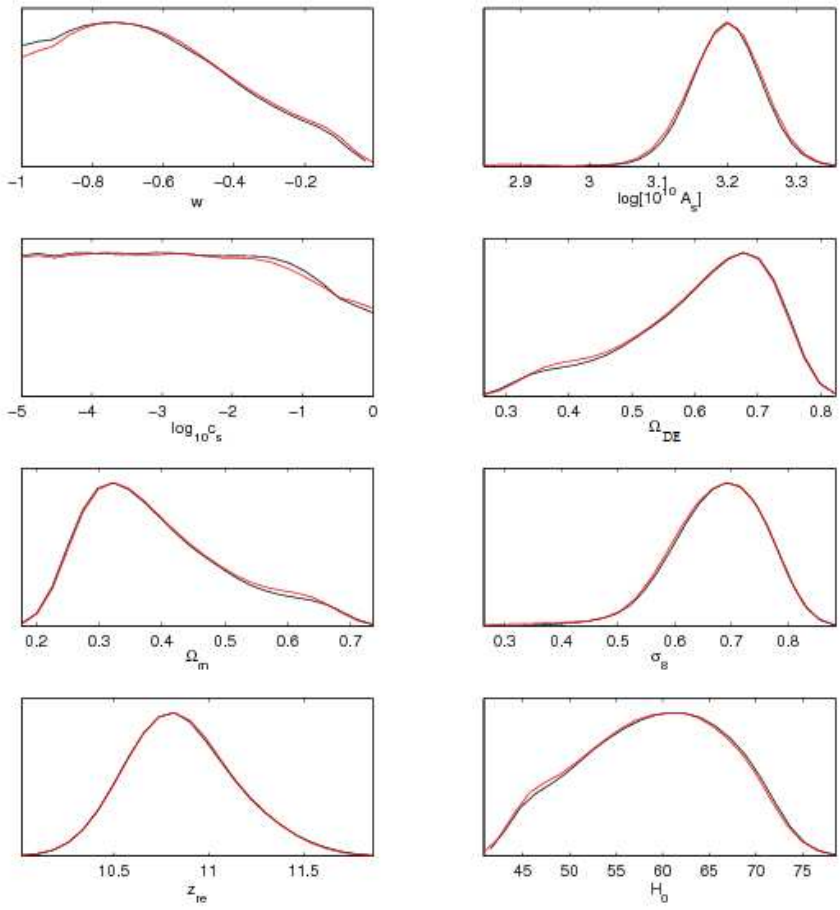

Figure 2.6: 1D marginalized plots for cosmological parameters using WMAP5 data for a scalar field (black) and elastic dark energy (red) model. We see very little difference between models.

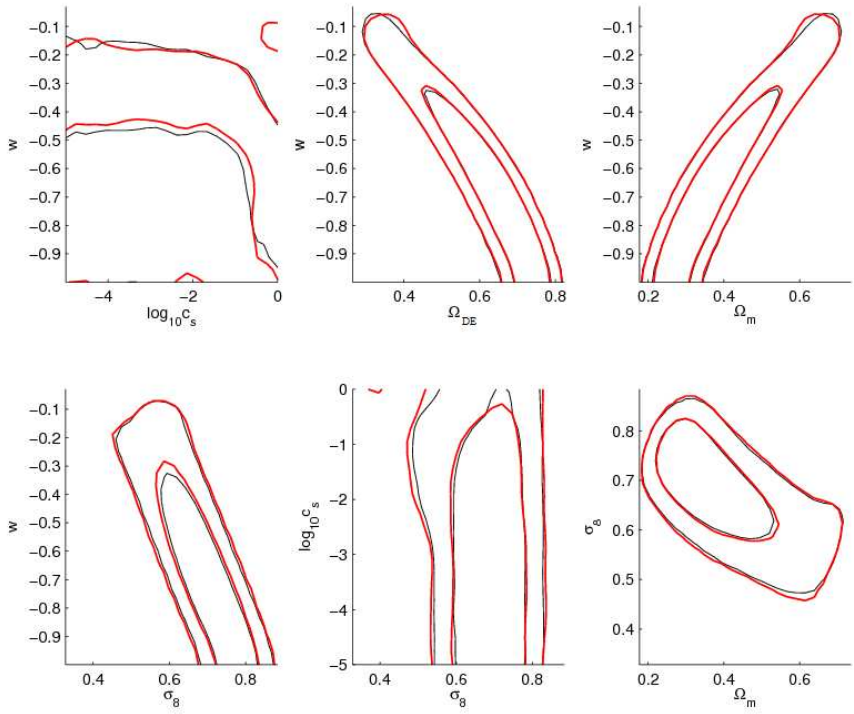

Figure 2.7: 2D marginalized plots for cosmological parameters using WMAP5 data for a scalar field (black) and elastic dark energy (red) model. Both models produce similar results, with no lower bound on the sound speed, c_s.

Using WMAP5 data on its own does not give a lower bound to the sound speed, and does not really help with differentiating between models. We then ran CosmoMC using WMAP5 and type Ia supernova (SNIa) data taken from the Union SNIa compilation, Kowalski et al. (2008), where the authors had complied data from the Supernova Legacy Survey, ESSENCE survey, and recent observations of high redshift SNIa made by the Hubble Space Telescope. This work was one of the most up to date SNIa compilation when we carried out our analysis. Our results are presented in figures 2.8 and 2.9. Although the inclusion of the SNIa data has tightened the constraint on the cosmological parameters, it has done nothing to help constrain c_s, and does not aid telling the two models apart. Both models allow the same range of cosmological parameters.

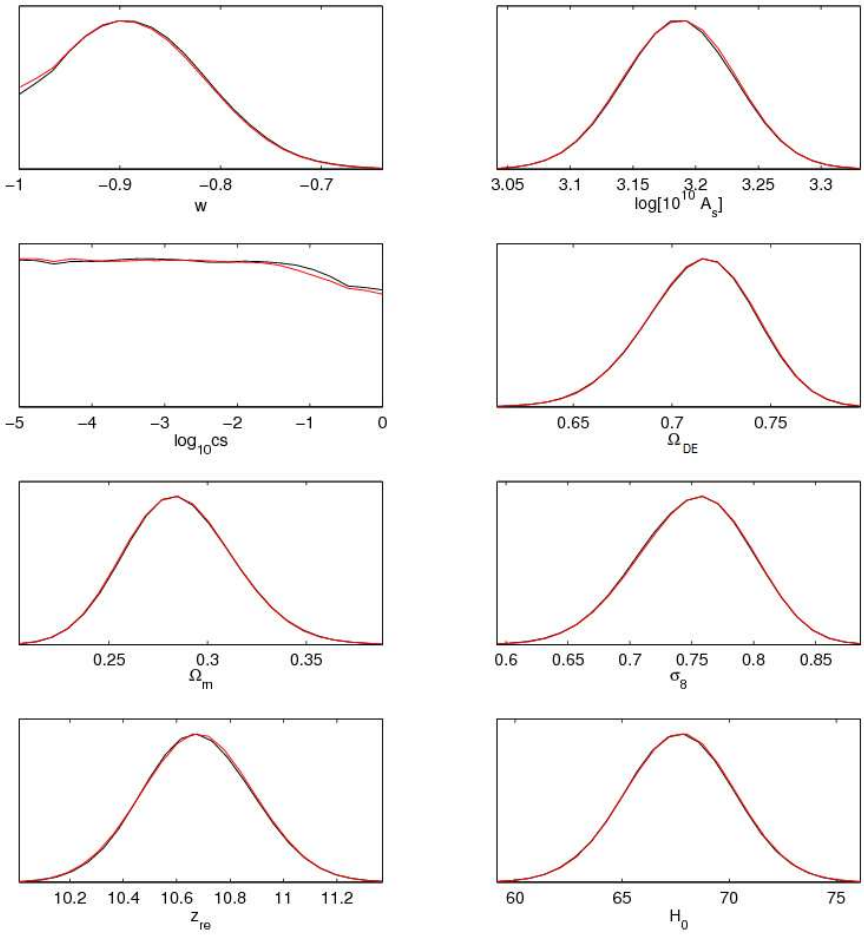

Figure 2.8: 1D marginalized plots for cosmological parameters using WMAP5 + SNIa data for a scalar field (black) and elastic dark energy (red) model. Again the models give near identical results.

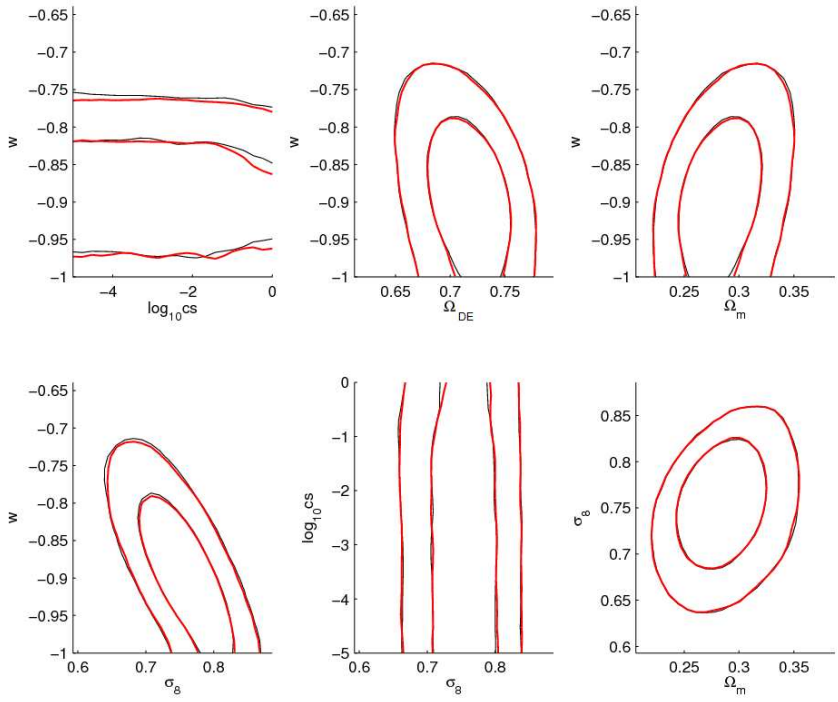

Figure 2.9: 2D marginalized plots for cosmological parameters using WMAP5 + SNIa data for a scalar field (black) and elastic dark energy (red) model.

2.5 Constraining parameters with weak lensing data

2.5.1 Including weak lensing

Weak lensing shear observations have been detected by many groups over the last decade, see for example, Kaiser et al. (2000), Hoekstra et al. (2002), Hamana et al. (2003), Maoli et al. (2000), Chang et al. (2004), and Jee et al. (2006). Most observations of weak lensing shear probe small angles, where non-linear effects in the evolution of the growth of structure are prevalent. We use the weak lensing data taken from the 3rd year Canada-France-Hawaii Telescope Legacy Survey (CFHTLS) Wide data release (Fu et al. (2008)). One of the primary goals of the CFHTLS is to use weak lensing measurements to explore the dark matter power spectrum and its evolution.

Utilising the CFHT MEGAPRIME/MEGACAM instrument the project has produced high quality weak lensing shear data. The CFHTLS Wide survey was designed to explore angular scales of up to 8 degrees, a fact that makes this survey ideal for our work. Our equations are linear and so only give accurate results at large angles, or low ℓ values. The data from Fu et al. (2008), based on the third year CFHTLS Wide data release, is predominantly set in the linear regime making it the perfect data to compare with. Figure 2.10 shows the measured aperture mass and shear variance from this data set.

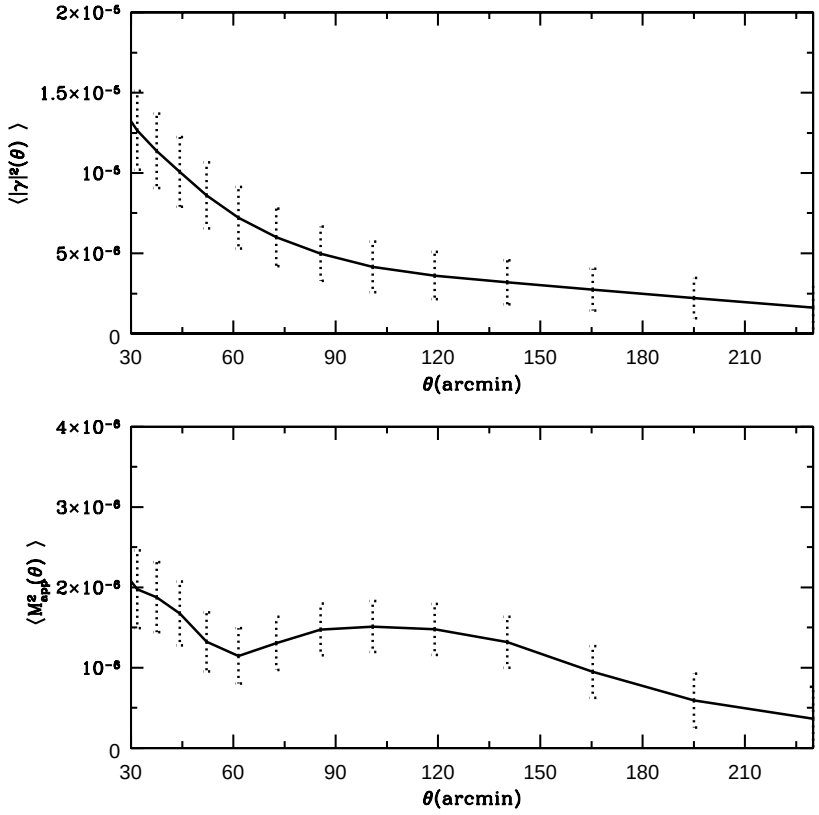

Figure 2.10: Aperture mass variance (bottom) and shear variance (top) from 3rd year CHFTLS Wide data (Fu et al. (2008)).

By introducing weak lensing data into our analysis we can improve upon the results from WMAP5 and SNIa data alone as, shown in the previous section, large differences

occur for certain parameter values. Massey et al. (2007), produced a module for CosmoMC allowing calculation of the convergence power spectrum, their data however was largely within the non-linear regime ranging from 0.1 to 40 arcmins. Given that we don't have a non-linear description of dark energy within CAMB, we have to confine ourselves to the linear part of the spectrum. The linear scale for shear variance is approximately $> 30'$, and with aperture mass variance it is larger at $> 80'$. However we use the Massey et al. (2007) module as a basic template for calculating the 2nd order weak lensing effects, shear variance and aperture mass variance. To avoid issues with non-linearity, we choose to use the shear variance data, and discarded any data observed at an angle lower than $30'$. The selection function was replaced with the one used by Fu et al. (2008) for the observable data, given by,

$$n(z) = A\frac{z^{0.612} + z^{0.621\times 8.125}}{z^{8.125} + 0.620}\,, \tag{2.43}$$

where A is a constant set to meet the condition that,

$$\int n(z)dz = 1\,. \tag{2.44}$$

1D and 2D marginalized plots obtained from CosmoMC for WMAP + weak lensing are shown in figures 2.11 and 2.12.

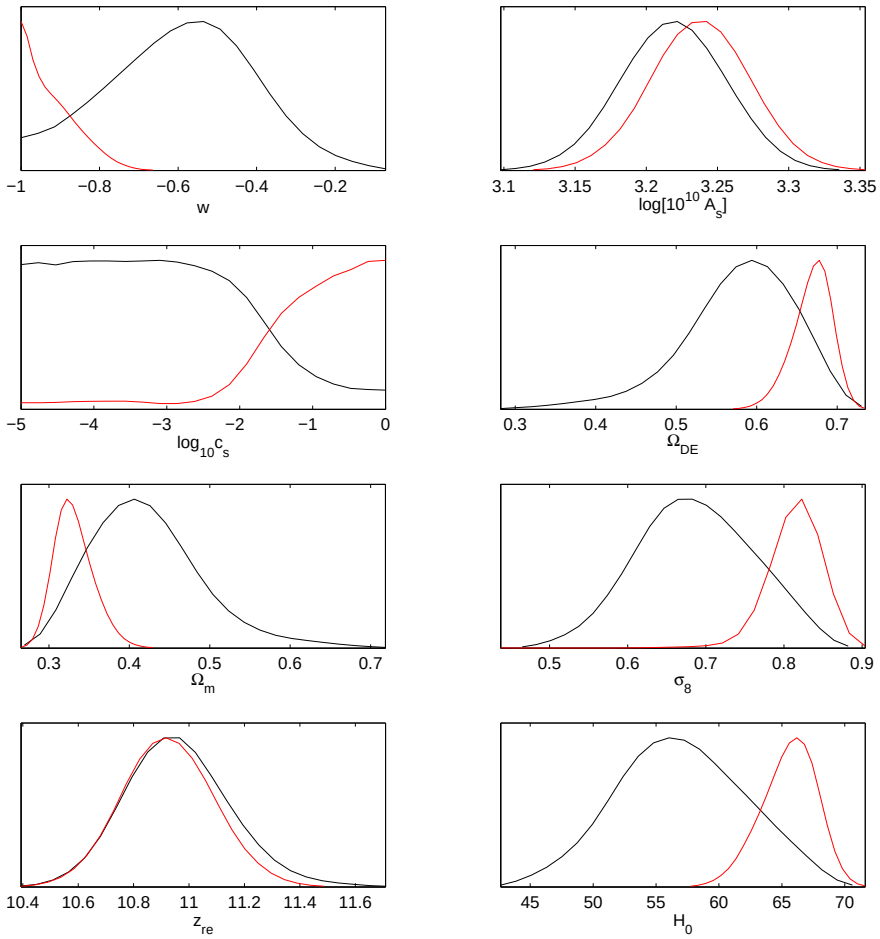

Figure 2.11: 1D marginalized plots for cosmological parameters using WMAP5 + weak lensing data for a scalar field (black) and elastic dark energy (red) model. We can now see there is a sharp reduction at low values in the likelihood for the sound speed in an elastic dark energy model.

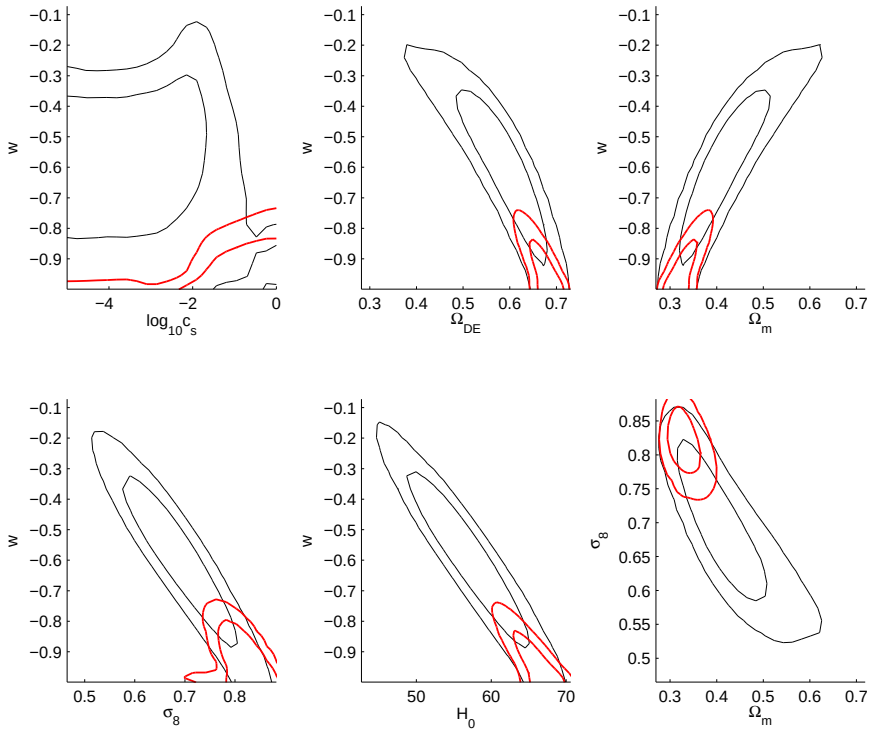

Figure 2.12: 2D marginalized plots for cosmological parameters using WMAP5 + weak lensing data for a scalar field (black) and elastic dark energy (red) model. Elastic dark energy is more tightly bound than the scalar field model.

With the inclusion of the weak lensing data there are now noticeable differences between the two CosmoMC outputs for the scalar field and elastic dark energy models. Elastic dark energy appears to be far more tightly constrained than the scalar field model. The most significant difference appears to be in the sound speed values that the two models can take. Referring to figure 2.11, we see that the elastic dark energy is almost cut off around $\log_{10} c_s \gtrsim -2.5$, whereas in contrast the scalar field prefers a lower sound speed. The elastic dark energy is not completely cut off due to the fact that when w approaches 1, the sound speed has less effect on the power spectra, meaning for $w \sim -0.99$, any c_s value will not significantly change the power spectra. This effect can be seen in the 2D plot in figure 2.12, where $\log_{10} c_s$ against w plot shows that as w approaches -1, $\log_{10} c_s$ can take on any value at the 98% confident limit. We find a

2σ lower bound to the sound speed to be $\log_{10} c_s \geq -3.35$. The equation of state, w, for the elastic dark energy model appears to be much more tightly constrained with the other parameters than in the scalar field case. The 2σ upper bound on the equation of state for elastic dark energy is $w \leq -0.79$, whereas for the scalar field we find a value of $w \leq -0.3$.

2.5.2 Results using WMAP5 + SNIa + weak lensing

We can combine the SNIa data with the WMAP5 + weak lensing data. Figures 2.13 and 2.14 shows the resulting plots for when SNIa data is used alongside WMAP5 and weak lensing data.

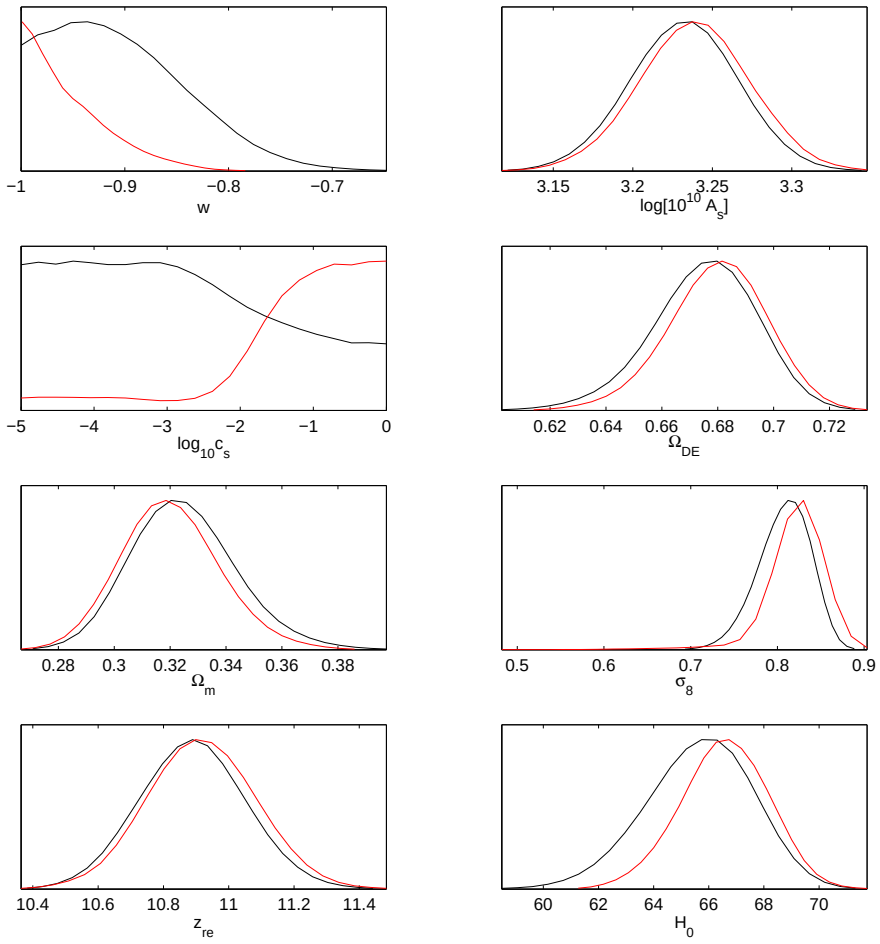

Figure 2.13: 1D marginalized plots for cosmological parameters using WMAP5 + SNIa + weak lensing data for a scalar field (black) and elastic dark energy (red) model. The sharp reduction in the likelihood of the sound speed for an elastic dark energy model is still present.

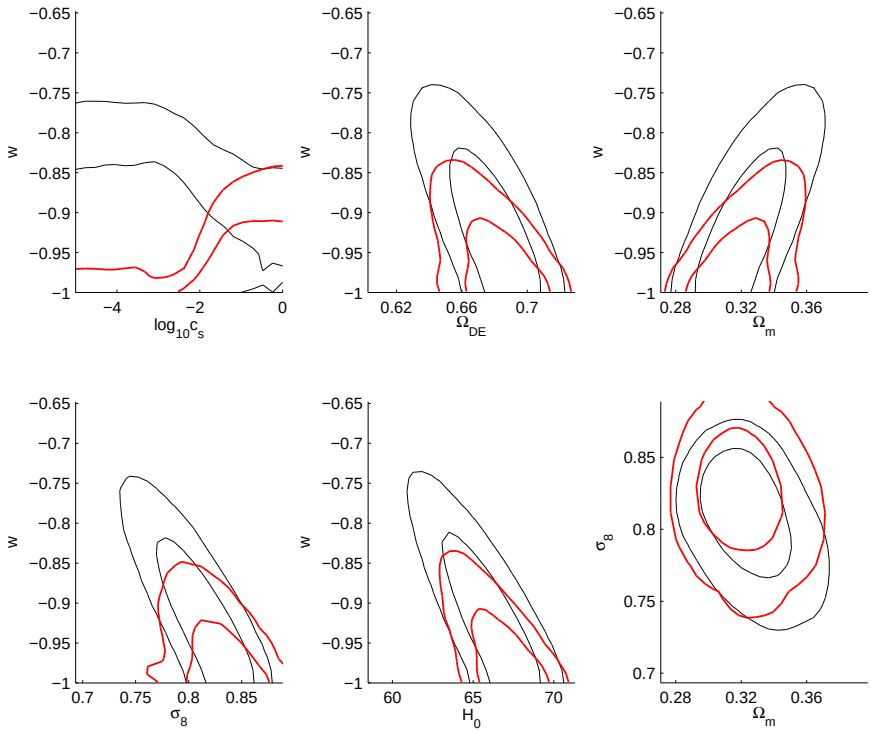

Figure 2.14: 2D marginalized plots for cosmological parameters using WMAP5 + SNIa + weak lensing data for a scalar field (black) and elastic dark energy (red) model. Both models are now more tightly bound when including the SNIa data.

The addition of the SNIa data tightens the range of values that the equation of state can take for both models, although this has had a more noticeable effect on the scalar field, which previously could take a much larger range. We find a 2σ upper bound for the equation of state for the elastic dark energy model to be $w \leq -0.872$, and for the scalar field, $w \leq -0.787$. With w more tightly constrained, so too are the values for Ω_m and $\Omega_{\rm DE}$. The same sound speed behaviour is observed as with just using WMAP5 and weak lensing data, with elastic dark energy displaying a sharp decline in likelihood at $\log_{10} c_s \gtrsim -2.5$, and the scalar field model preferring a lower sound speed. We find a 2σ lower bound for the elastic dark energy sound speed to be $\log_{10} c_s \geq -3.84$. No such bound is found for the scalar field model.

2.5.3 Varying type Ia supernova

The supernova data is based on observations of type Ia supernova, which are assumed to be standard candles. When a star reaches the Chandrasekhar limit, the maximum mass a body can have before the degenerate electron pressure is overcome by the gravitational pressure, it can no longer support itself and collapses, resulting in a supernova. Typically type Ia supernova occur in binary systems where a white dwarf strips the other star of its mass, slowly increasing the white dwarfs mass. Once the white dwarf reaches the Chandrasekhar limit, it becomes a supernova. Because the mass of the star is known due to the Chandrasekhar limit, it is assumed that the peak luminosity is then the same no matter where the supernova is in the Universe, that is, it is a standard candle. This means that by measuring the difference between apparent and absolute magnitude, one can compute the distance of the galaxy that the supernova occurred in. This can then be compared with the redshift of the galaxy. Conventionally the differences between apparent m and absolute M magnitude is expressed as,

$$m - M = 5 \log \left(\frac{d_L}{10\text{pc}} \right) + K \,, \tag{2.45}$$

where K is to account for the shifting of the photon wavelength as the Universe expands, and d_L is the luminosity distance and is defined as,

$$d_L \equiv \frac{\chi}{a} \,. \tag{2.46}$$

The specific properties that may affect the way in which the star undergoes this dramatic change, such as the local environment and its exact composition can be different at different redshifts. We mentioned that SNIa originate from a single degenerate system (a white dwarf and a companion), but as pointed out in Riess and Livio (2006), there is no evidence to say that SNIa cannot occur in double degenerate systems. These two progenitor systems differ in delay time to the explosion and local environment thus introducing an uncertainty into the evolution effects of SNIa, should double degenerate systems produce SNIa. Without a detailed understanding it is hard not to imagine the

possibility that SNIa luminosity may not be independent of redshift. At its extreme, such a conclusion could call into question the very fact that the Universe is undergoing an accelerated expansion. Ferramacho et al. (2008) examined what would happen if the peak magnitude of a supernova was able to vary linearly with time by defining,

$$\Delta m(z) = snK\left(\frac{t_0 - t(z)}{t_0 - t_1}\right), \tag{2.47}$$

where t_0 is the present age of the Universe, $t(z)$ is the time at the redshift of the supernova, t_1 is the age of the Universe at a redshift of 1, and snK represents the change of magnitude at this redshift. In order to see what effect this would have on our models we incorporated the parameter snK into our version of CosmoMC. We have plotted the resulting 1D and 2D marginalized plots in Figures 2.15 and 2.16 respectively.

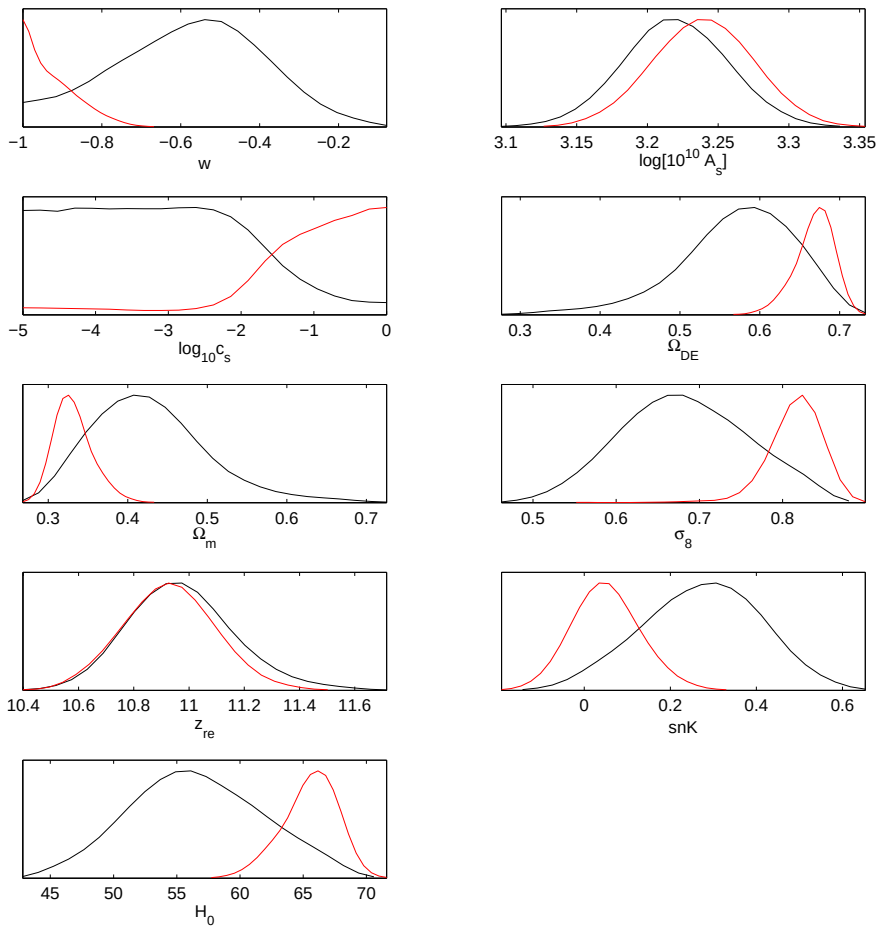

Figure 2.15: 1D marginalized plots for cosmological parameters using WMAP + SNIa + *snK* + weak lensing data for scalar field (black) and elastic dark energy (red). The scalar field is more sensative to the *snK* parameter, allowing a wider range of values than in the elastic dark energy case.

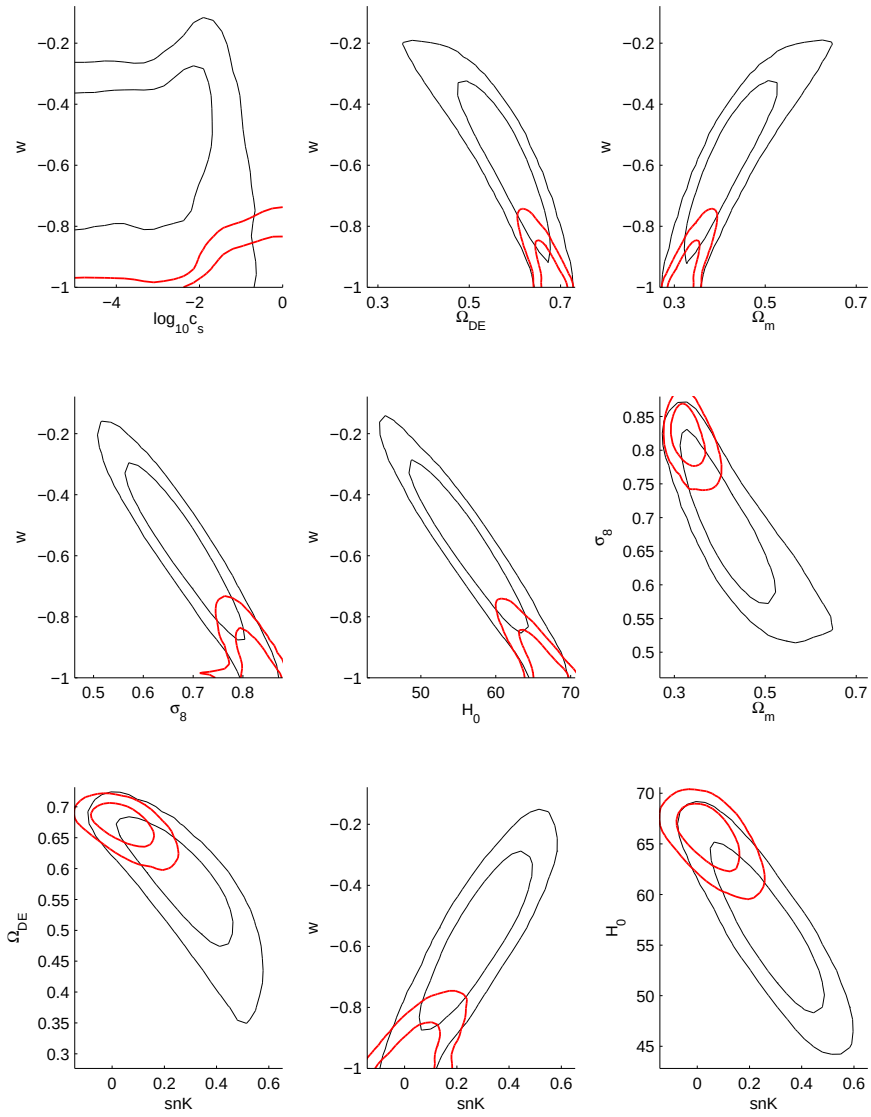

Figure 2.16: 2D marginalized plots for cosmological parameters using WMAP + SNIa + *snK* + weak lensing data for scalar field (black) and elastic dark energy (red).

Not surprisingly, allowing the supernovae to evolve with time has reduced the constraints for both models on all parameters, but this has not qualitatively changed our previous result. We find a lower bound on the elastic dark energy sound speed still exists, with a 2σ lower bound being $\log_{10} c_s \geq -3.50$. No such lower bound exists for the scalar field. The equation of state for the scalar field model is poorly constrained, and highly degenerate with *snK*. We find that the 2σ upper bound on w is $w \leq -0.795$

for elastic dark energy and $w \leq -0.293$ for the scalar field. When *snK* is positive, distant objects appear brighter, and when *snK* is negative distant objects are dimmer. By modifying this distance-redshift relation, we change the amount of dark energy, and its equation of state, needed to agree with observations. Looking at figure 2.16 we can see that *snK* is degenerate with $\Omega_{\rm DE}$, w and H_0.

2.6 Conclusion

The aim of the work encompassed within this chapter was to ascertain if, using weak gravitational lensing, coupled with WMAP5 and SNIa data, we could distinguish between an elastic dark energy and a scalar field model, and place a lower limit on the sound speed of elastic dark energy. Since the weak lensing effect on a photon's path only depend on the gravitational force created by a body, and not on its make up, weak lensing is a powerful method in obtaining cosmological parameters.

It is known that as the sound speed of elastic dark energy is lowered, it can behave more like dark matter, exhibiting clustering properties (Battye and Moss (2007)). If such behaviour is occurring within our Universe, elastic dark energy will be modifying the gravitational potentials throughout space. The strength of this clustering is directly related to the sound speed, and so elastic dark energy's sound speed would directly impact on weak lensing effects. First we demonstrated that using WMAP5 and SNIa data alone does not give a lower bound on the sound speed for either model, nor help with differentiating between the models (figures 2.8 and 2.9). From the scalar field point of view, this agrees with work carried out by a number of authors. For example, Weller and Lewis (2003) did not detect a significant constraint on the sound speed using the first year WMAP data combined with large scale structure and supernovae observations. A similar analysis, given in Bean and Doré (2004), obtained a 1σ upper limit on the sound speed $c_s^2 < 0.04$, but could not detect a lower limit. The difficulty in putting a significant set of constraints on the sound speed of a scalar field model was also pointed out in Hannestad (2005), where, using CMB, SNIa and large scale struc-

ture data the author showed that placing such constraints on the sound speed was not currently possible. We then showed that combining WMAP5 with the shear variance data from the 3rd year CFHTLS Wide data release (Fu et al. (2008)), does show differences between the models (figures 2.11 and 2.12). The elastic dark energy model's equation of state is more likely to be closer to -1 than the scalar field model, which itself can take on a range of values with the marginalised curve peaking at $w \sim -0.55$. The models are very different with respect to sound speed, with elastic dark energy showing a sharp drop off in the marginalised sound speed, with 2σ lower bounds of $\log_{10} c_s \geq -3.35$ when using WMAP5 and weak lensing data, and $\log_{10} c_s \geq -3.84$ when using WMAP5, SNIa and weak lensing data. The reason that the 2σ bound is lower when including the SNIa data is to do with the fact that when the equation of state is close to -1, the sound speed can take on a larger range of values. Including SNIa data tightens the constraints on the equation of state, forcing it closer to -1, and this in turns lowers the bound on the sound speed.

The scalar field model shows no cut off in its sound speed when combining the weak lensing data with WMAP5 and the SNIa data. Using these data sets we find a 2σ upper bound on w for the scalar field to be $w \leq -0.787$, larger than the elastic dark energy's upper bound of $w \leq -0.872$.

Finally we investigated the possibility that SNIa are not standard candles, but vary in brightness as a function of redshift. We used a model where peak luminosity is linearly evolving with redshift, with the parameter *snK* representing this change. In general the constraints on all parameters are not as tight (figures 2.15 and 2.16). The data mirrors what we saw with just using WMAP5 and weak lensing data, where the scalar field could take on a large range of values for the cosmological parameters, and had no lower bound to the sound speed. Elastic dark energy is still more tightly constrained than the scalar field, and we can place a 2σ lower bound on the sound speed of $\log_{10} c_s \geq -3.50$.

2.7 Tables

Below we have tabulated the marginalised statistics for all weak lensing runs on CosmoMC.

	Scalar Field		**Elastic Dark Energy**	
Parameter	Mean	σ	Mean	σ
$\Omega_b h^2$	0.0223	0.0006	0.0225	0.0005
$\Omega_c h^2$	0.111	0.005	0.119	0.0028
θ	1.03	0.003	1.04	0.0029
w	-0.590	0.178	-0.918	0.065
n_s	0.954	0.013	0.958	0.013
$\log[10^{10} A_s]$	3.21	0.04	3.23	0.03
$\log_{10} c_s$	-3.13	1.15	-1.08	0.941
$\Omega_{\rm DE}$	0.577	0.069	0.668	0.024
Age/GYr	14.2	0.319	13.8	0.129
Ω_m	0.422	0.069	0.331	0.024
σ_8	0.686	0.073	0.813	0.034
z_{re}	10.9	0.185	10.9	0.161
H_0	56.9	5.02	65.5	2.14

Table 2.2: Scalar field and elastic dark energy statistics from the CosmoMC runs using WMAP5 and weak lensing data.

	Scalar Field		**Elastic Dark Energy**	
Parameter	Mean	σ	Mean	σ
$\Omega_b h^2$	0.0224	0.0005	0.0225	0.0006
$\Omega_c h^2$	0.117	0.0028	0.119	0.0029
θ	10.4	0.0029	10.4	0.0029
w	-0.903	0.064	-0.951	0.04
n_s	0.957	0.012	0.957	0.018
$\log[10^{10} A_s]$	3.23	0.033	3.23	0.034
$\log_{10} c_s$	-2.87	1.34	-1.22	1.05
Ω_{DE}	0.674	0.018	0.679	0.017
Age/GYr	13.8	0.13	13.8	0.12
Ω_m	0.325	0.018	0.320	0.017
σ_8	0.807	0.029	0.820	0.034
z_{re}	10.8	0.157	10.9	0.162
H_0	65.6	1.89	66.5	1.54

Table 2.3: Scalar field and elastic dark energy statistics from the CosmoMC runs using the WMAP5, SNIa and weak lensing data

	Scalar Field		**Elastic Dark Energy**	
Parameter	Mean	σ	Mean	σ
$\Omega_b h^2$	0.0222	0.0006	0.0225	0.0006
$\Omega_c h^2$	0.111	0.0051	0.119	0.0029
θ	1.03	0.003	1.04	0.003
w	-0.581	0.182	-0.921	0.064
n_s	0.953	0.013	0.957	0.013
$\log[10^{10} A_s]$	3.21	0.036	3.23	0.035
$\log_{10} c_s$	-3.13	1.15	-1.11	0.976
snK	0.270	0.134	0.0488	0.0778
Ω_{DE}	0.573	0.07	0.668	0.024
Age/GYr	14.2	0.331	13.8	0.13
Ω_m	0.426	0.07	0.331	0.024
σ_8	0.683	0.074	0.815	0.031
z_{re}	10.9	0.190	10.9	0.165
H_0	56.6	5.12	65.5	2.14

Table 2.4: Scalar field and elastic dark energy statistics from the CosmoMC runs using the WMAP5, SNIa and weak lensing data and using the *snK* parameter

3

Constraints from the ISW effect

As well as weak lensing, there is another cosmological observation we can use to constrain dark energy parameters, and potentially discriminate elastic dark energy from a scalar field dark energy. This observation is the Integrated Sachs-Wolfe (ISW) effect (Sachs and Wolfe (1967)). Like the Sachs-Wolfe (SW) effect, the ISW effect arises when photon energies are modified in the presence of a gravitational field. The difference is that while the SW effect occurs when CMB photons leave the surface of last scattering, the ISW effect occurs as these CMB photons travel through the evolving Universe. Encountering evolving potentials leads to a late time shifting of CMB photon energies, giving rise to secondary anisotropies on the CMB power spectrum.

3.1 Introduction

As a photon leaves the surface of last scattering it will encounter many potential wells set up by the uneven distribution of matter throughout the Universe. These gravitational potential wells cause a photon's wavelength to be blueshifted as it falls into a well, and then redshifted as it climbs out. During periods of matter domination the gravitational potentials are constant with time, $\dot{\Phi} = 0$, and so the energy gained by a photon falling into a well is lost climbing out of the well. If at some point the Universe were to become dominated by a dark energy component, the gravitational potentials

would begin to decay. A CMB photon now falling into a potential well gains a given amount of energy, but as the potential is being reduced, the photon will lose less energy climbing out and thus the photon experiences a net change in energy. This shift in photon energy is known as the ISW effect, where the term 'integrated' refers to the fact that the energy shift is due to the sum of all the potential wells a given photon encounters between the surface of last scattering and the observer. Therefore, the ISW effect gives rise to a further anisotropy in the CMB TT power spectrum on large scales, $l < 10$, caused at late times ($z < 2$) when the Universe becomes dominated by dark energy. The very existence of an ISW effect is further proof of an accelerated expansion, reinforcing the inferences made using SNIa data (Perlmutter et al. (1999), Riess et al. (1998)).

The ISW signature imprinted on the CMB TT power spectrum cannot be separated from the primary CMB anisotropies laid down at the time of last scattering, furthermore the amplitude of the ISW component will be much lower than that of the primary anisotropies. However, given that the decaying gravitational perturbations give rise to this net photon energy shift, there should be a direct correlation between tracers of the large scale structures in the Universe and the temperature anisotropies in the CMB. This was first suggested in Crittenden and Turok (1996). If any such correlation between the temperature differences and the matter distribution are detected, it will be due to the ISW effect since the primary temperature anisotropies were formed well before large scale structure formation. Since CMB and matter correlations are relatively weak, in order to reduce the chance of accidental correlations a near full sky map of the matter distribution is needed. The ISW effect was first detected by Boughn and Crittenden (2004) by correlating the first year WMAP maps (Bennett et al. (2003)), with the NRAO VLA sky survey (NVSS) of radio galaxies (Condon et al. (1998)), which was generated using the Very Large Array (VLA) in New Mexico, and the hard X-ray background data from the HEAO-1 satellite (Boldt (1987)). These surveys mapped out radio and X-ray emissions respectively, emanating from active galaxies out to a redshift of order 1, and due to the large sky coverage allow large angular scales to be

probed. Since its initial detection the ISW effect has now been observed by numerous groups, using a variety of different density tracers and probing different redshift ranges from $z \sim 0.1$ to $z \sim 1.5$. See for example the work of Scranton et al. (2003), Fosalba et al. (2003), Afshordi et al. (2004), Nolta et al. (2004), Giannantonio et al. (2006), McEwen et al. (2007), and Rassat et al. (2007). Typical ISW matter correlations have been detected at significances between a $2 \sim 3\sigma$ significance, and are consistent with a ΛCDM model.

3.2 A theoretical description of the ISW effect

Here we outline the equations used to describe the ISW effect. If Φ and Ψ are the gravitational potentials in the conformal Newtonian gauge, then the expected temperature perturbation of a given photon coming in the direction $\hat{\mathbf{n}}$ is given by,

$$\frac{\Delta T(\hat{\mathbf{n}})}{T} = \int_{\tau_{\rm dec}}^{\tau_0} d\tau \left(\dot{\Phi}[(\tau_0 - \tau)\hat{\mathbf{n}}, \tau] + \dot{\Psi}\left[(\tau_0 - \tau)\hat{\mathbf{n}}, \tau\right] \right) , \tag{3.1}$$

where $\dot{\Phi}$ and $\dot{\Psi}$ are derivatives with respect to conformal time and $\tau_{\rm dec}$ is the time of decoupling. As mentioned in the introduction, potentials that vary with time modify the net energy gain of photons passing through them, and so one would expect a correlation with nearby large scale structure if the Universe is undergoing an accelerated expansion. The observed density contrast of galaxies in the direction $\hat{\mathbf{n}}$ is given by,

$$\delta_g(\hat{\mathbf{n}}) = \int b_g(z) W(z) \delta_m(\hat{\mathbf{n}}, z) dz \, , \tag{3.2}$$

where it is assumed that the galaxy overdensity traces the CDM density contrast δ_m, and b_g is the linear galaxy bias. The cross correlation and auto correlation functions of these quantities are defined as,

$$C_{Tg}(\theta) \equiv \langle \frac{\Delta T(\hat{\mathbf{n}}_1)}{T} \delta_g(\hat{\mathbf{n}}_2) \rangle \, , \tag{3.3}$$

$$C_{gg}(\theta) \equiv \langle \delta_g(\hat{\mathbf{n}}_1) \delta_g(\hat{\mathbf{n}}_2) \rangle \, , \tag{3.4}$$

$$C_{TT}(\theta) \equiv \langle \frac{\Delta T(\hat{\mathbf{n}}_1)}{T} \frac{\Delta T(\hat{\mathbf{n}}_2)}{T} \rangle \,. \tag{3.5}$$

These can be decomposed into a Legendre series,

$$C_{xx}(\theta) = \sum_{l=2}^{\infty} \frac{2l+1}{4\pi} C_l^{xx} P_l(\cos\theta) \,, \tag{3.6}$$

which now gives the auto/cross correlation in harmonic space. The C_l^{xx} are the corresponding auto/cross correlation power spectra, and P_l are the Legendre polynomials. Seljak and Zaldarriaga (1996) split the theoretical calculation of a power spectrum into source and geometric terms, which lead to a more efficient way of calculating numerical results, and was implemented in CMBFAST. The equivalent source terms in the CMB codes for $\delta_g(\hat{\mathbf{n}})$ and $\frac{\Delta T(\hat{\mathbf{n}})}{T}$ were given in Corasaniti et al. (2005), and stated earlier (see equations (2.36) and (2.37)) as,

$$S_m = W(z) b_g \delta_m(z) \,, \tag{3.7}$$

$$S_{ISW} = e^{-\kappa}(\dot{\Phi} + \dot{\Psi}) \,, \tag{3.8}$$

where $W(z)$ is a window function and the exponential term is known as the visibility function, which accounts for further scattering of the CMB photons post-reionization. The ISW effect changes the TT power spectrum by increasing power at the larger angular scales, or lower values of l. Using CMBFAST we have plotted the TT power spectrum for both an elastic dark energy and scalar field model, with a variety of different values for the dark energy equation of state, w, and its sound speed, c_s. These are presented in figure 3.1. As with the weak lensing convergence power spectra, a larger value of w gives greater differences between the power spectra as the sound speed is varied in both models.

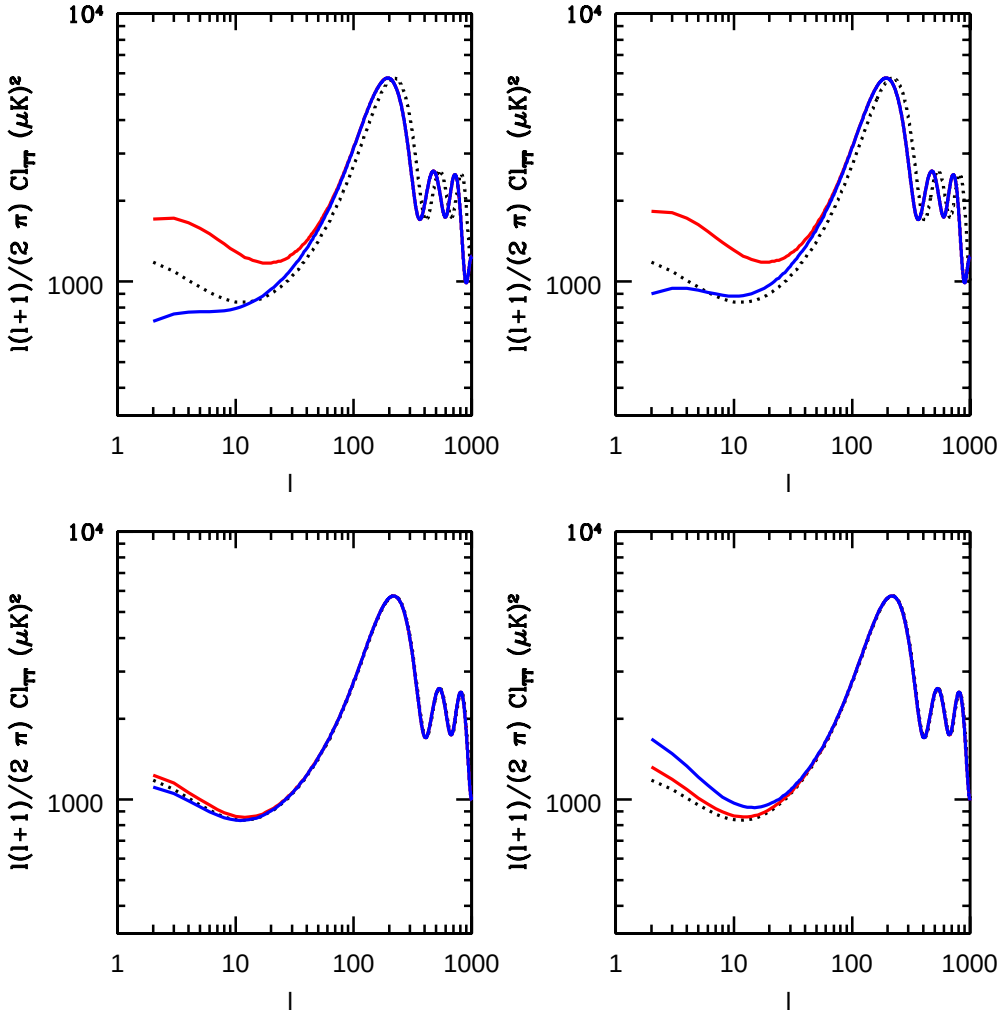

Figure 3.1: Here we have plotted the TT power spectra for different values of w and c_s. The plots on the left are scalar field models and the plots on the right are elastic dark energy model. The plots on the top have $w = -0.4$, the plots on the bottom have $w = -0.9$. The black dotted line in all plots is a ΛCDM model, the blue lines correspond to $c_s^2 = 10^{-4}$, and the red lines to $c_s^2 = 1$. The other cosmological parameters are set as $\Omega_m = 0.266$, $\Omega_{DE} = 0.734$, $h = 0.71$, $z_{\rm dec} = 1088.2$, $n_s = 0.963$, $\tau = 0.088$ and $\Delta^2_{\mathcal{R}} = 2.43 \times 10^{-9}$.

3.2.1 Modification to CMB codes for elastic dark energy

In the case of a cosmological constant, or dark energy that does not cluster, equation (3.7) is sufficient to calculate the ISW galaxy power spectrum, and subsequent quantities. As with the weak lensing case, when considering elastic dark energy some modifications must be made due to the fact that elastic dark energy can cluster if $c_S \approx 0$. We therefore replace equation (3.7), with

$$S_m = W(z) b_g \left(\Omega_m \delta_m + \Omega_{DE} \delta_{DE}\right) , \tag{3.9}$$

where δ_{DE} is the density contrast of the elastic dark. If there is no dark energy perturbation, it is clear that equation (3.9) is going to be smaller by a factor of Ω_m than the original equation it has replaced, equation (3.7). As will be explained when used in CosmoMC, the factor, b_g, will effectively correct for this discrepancy. We have plotted the temperature matter (Tg) power spectrum and corresponding cross correlation function, $C_{Tg}(\theta)$, for an elastic dark energy, scalar field, and ΛCDM model, with a variety of different dark energy parameters, shown in figures 3.2 and 3.3 respectively.

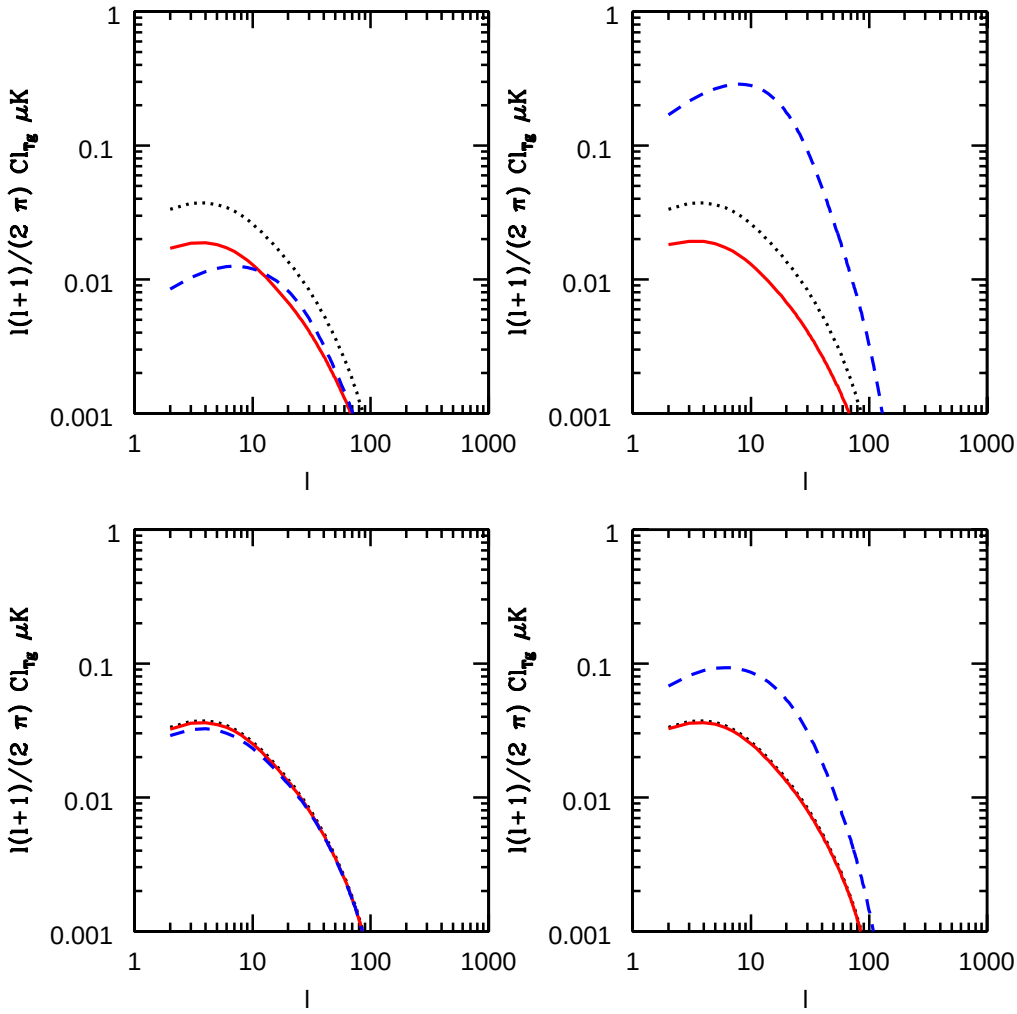

Figure 3.2: We have plotted the ISW-galaxy power spectra. The plots on the left are scalar field models and the plots on the right are elastic dark energy model. The plots on the top have $w = -0.4$, the plots on the bottom have $w = -0.9$. The black dotted line in all plots is a ΛCDM model, the blue lines correspond to $c_s^2 = 10^{-4}$, and the red lines to $c_s^2 = 1$. The other cosmological parameters are set as in figure 3.1.

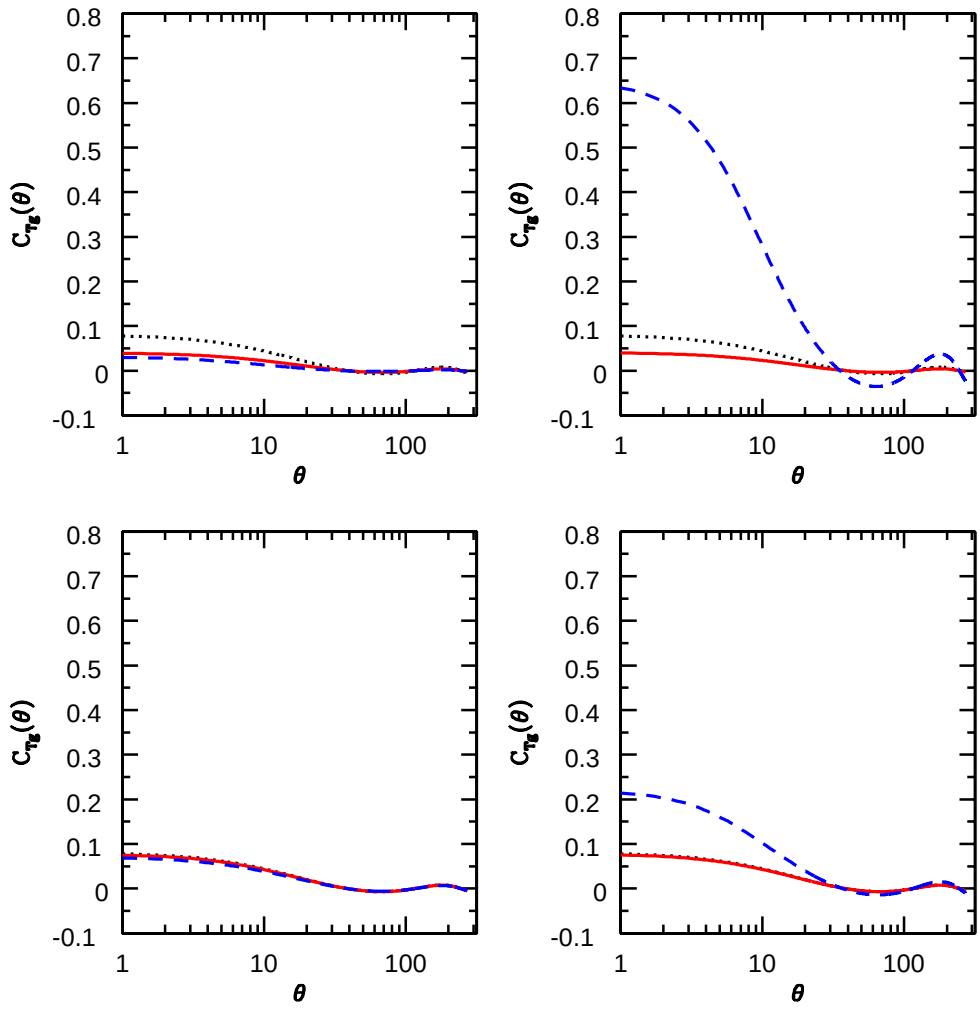

Figure 3.3: These plots are of the ISW-galaxy correlation function, laid out as figure 3.2. We see that in the elastic dark energy models on the right, much larger differences appear when the sound speed is lowered compared with the scalar field case.

3.3 Constraining parameters with ISW data

3.3.1 The ISW data

We choose to use the publicly available ISW data provided in Gaztanaga et al. (2006) (henceforth we refer to this as the ISW data). This data has been obtained from five independent collaborations where the CMB anisotropies have been cross correlated with galaxy surveys, spanning a range in median redshift of $0.1 < \bar{z} < 1$, and extending over the electromagnetic spectrum from the infra-red to the X-ray waveband. Because the ISW effect occurs at large angles, there are no non-linear effects that we need to take into account, as there were in the weak lensing case. The compilation of the data was averaged over fixed angular scale of $\theta = 6^{\circ}$, and the bias was removed by comparing the galaxy auto-correlation function, with the theoretical matter correlation function,

$$b = \sqrt{\frac{C_{GG}}{C_{mm}}}, \tag{3.10}$$

where C_{GG} is the observed galaxy auto-correlation function, and C_{mm} the theoretical prediction of $\langle \delta_m(\hat{\mathbf{n}}_1)\delta_m(\hat{\mathbf{n}}_2)\rangle$. Although bias is a function of redshift, Gaztanaga et al. (2006) fixed the bias as a constant at the median redshift of the given survey, $b = b(\bar{z})$. The data is then presented as C_{Tg}/b, normalised to the cosmic concordance model (CCM). This data is shown in table 3.1.

$\bar{z}$	C_{Tg}/b	b	Catalogue	Band
0.1	0.7 ± 0.32	1.1	2MASS	infra-red ($2\mu m$)
0.15	0.35 ± 0.17	1.0	APM	optical (b_j)
0.3	0.26 ± 0.14	1.0	SDSS	optical (r)
0.5	0.216 ± 0.096	2.4	SDSS high z	optical (r+colours)
0.9	0.043 ± 0.015	1.2	NVSS+HEAO	radio and X-rays

Table 3.1: ISW data and surveys used in our analysis, taken from Gaztanaga et al. (2006).

For any other model, we must compute a relative bias given by,

$$b = \sqrt{\frac{C_{mm}^{CCM}}{C_{mm}^{mod}}}, \tag{3.11}$$

where C_{mm}^{CCM} is the matter auto-correlation function in the CCM measured at $8h^{-1}$Mpc for a given median redshift, and C_{mm}^{mod} is the matter autocorrelation function for a given cosmological model. According to Gaztanaga et al. (2006) where one chooses to measure this relative bias has a negligible effect on the outcome. Because we are defining the bias in this way, in the absence of dark energy perturbations, the factor of Ω_m in equation (3.9) will be accounted for. To take into account the error in the median redshift when calculating χ^2, we use,

$$\sigma_i^2 = \sigma_C^2 + \left(\frac{d(C_{Tg}/b)}{dz}\right)^2 \sigma_z^2, \tag{3.12}$$

where σ_C^2 is the error in C_{Tg} and σ_z^2 the error in median redshift. However as shown in Gaztanaga et al. (2006), this extra error term for median redshift makes very little difference to the final answer. To approximate the galaxy redshift distribution, we use a generic window function also used by Gaztanaga et al. (2006), given as,

$$W(z) = \frac{1}{\Gamma\left(\frac{m+1}{\beta}\right)}\beta\frac{z^m}{z_0^{m+1}}e^{-\left(\frac{z}{z_0}\right)^\beta}. \tag{3.13}$$

The parameters β and m modify the shape of the selection function. We have plotted this window function in figure 3.4 for illustration. Gaztanaga et al. (2006) set the values for these parameters as $\beta = 1.5$ and $m = 2$ for there analysis, assuming that this was a similar representation to the actual galaxy redshift distribution. Since we are using the same data as these authors, we also use $\beta = 1.5$ and $m = 2$. The authors note that setting $\beta = 2.5$ and $m = 4$ did not change the results by a significant margin. We can also confirm this, while quantitatively different, the qualitative differences between elastic dark energy and a scalar field were the same for these two choices of parameters.

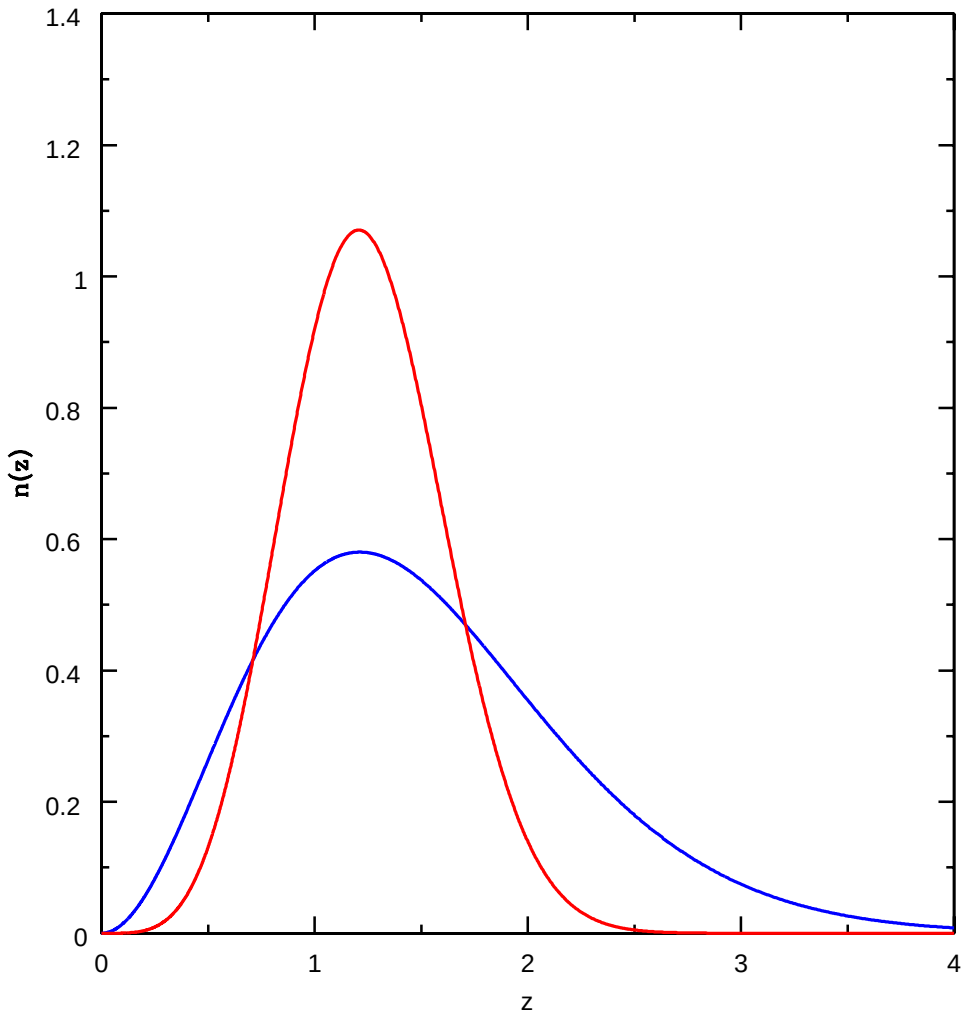

Figure 3.4: The galaxy distribution as a function of redshift n(z) is plotted for $\beta = 1.5$ and $m = 2$ (blue line) and $\beta = 2.5$ and $m = 4$ (red line).

When combining surveys in this way, some consideration must be given to possible overlapping in sky position or redshift, which could lead to covariance between the data sets. Gaztanaga et al. (2006) chose data which complemented each other, leading to a 1% volume overlap in the surveys. When two data sets overlap heavily in sky position for instance, there is a negligible overlap in the redshift. Since the individual sampling errors are of order 30%, the overlap impact on the analysis can be considered

negligible. At the time this work was carried out, Gaztanaga et al. (2006) was was the most up to date combined analysis of the ISW effect. Since then a more thorough approach to combining data sets and analysing the ISW effect has been undertaken by Giannantonio et al. (2008). Here, the authors reanalysed the ISW observation in a consistent way, and measured the covariances between each data set using a variety of different methods. This analysis concluded that the overall significance of the ISW detection was $\sim 4.5\sigma$, and was consistent with the CCM, albeit favouring models with a slightly lower value of Ω_m.

3.3.2 Results using WMAP5 + ISW

As with our weak lensing analysis, we ran CosmoMC on the COMA cluster at the Jodrell Bank Centre for Astrophysics. For each run we used the MPICH2 and OpenMP allowing us to run 4 chains, with each chain being made up of 4 threads, running on 4 virtual cores. We again tested the convergence using the MPI Converge Stop function set at 0.03. We first ran our code in CosmoMC using the WMAP5 and the ISW data. Table 3.2 shows the cosmological parameters used with the initial values from our params.ini file. All other options and parameters were left at their default settings.

Parameter	Start Center	Min	Max	Starting Width	σ estimate
$\Omega_b h^2$	0.0223	0.005	0.1	0.001	0.001
$\Omega_c h^2$	0.105	0.01	0.99	0.01	0.01
θ	1.04	0.5	10	0.002	0.002
w	-0.8	-0.999	0	0.02	0.02
n_s	0.95	0.5	1.5	0.02	0.01
$\log[10^{10} A_s]$	3	2.7	4	0.01	0.01
$\log[c_s]$	0	-5	0	0.02	0.02

Table 3.2: Initial cosmological paramters used in all CosmoMC runs, unless otherwise stated.

As before we use the default CosmoMC installation which imposes priors on H_0 and

the age of the Universe as, $40\,\mathrm{km\,s^{-1}\,Mpc^{-1}} < H_0 < 100\,\mathrm{km\,s^{-1}\,Mpc^{-1}}$ and $10\,\mathrm{Gyr} <$ age $< 20\,\mathrm{Gyr}$. Unless otherwise stated, we used these settings, and the values in table 3.2 on all CosmoMC runs. The results are presented below, with 1D marginalized plot shown in figure 3.5 and the 2D marginalized plots are shown in figure 3.6. As in the weak lensing case, the values for the elastic dark energy model are more tightly constrained than the scalar field model, albeit not as much. Comparing the 2D marginalized plot of w against $\log_{10} c_s$ in the weak lensing, and ISW cases (figures 2.12 and 3.6), we see that the ISW data confines w to values closer to $w = -1$ than using the weak lensing data. Having a smaller range of w leads to tighter constraints on all other parameters. The same cut off appears in the sound speed for elastic dark energy although there is now a peak at $\log_{10} c_s \approx -1.7$. The 2σ lower bound on the elastic dark energy sound speed is $\log_{10} c_s \geq -3.13$.

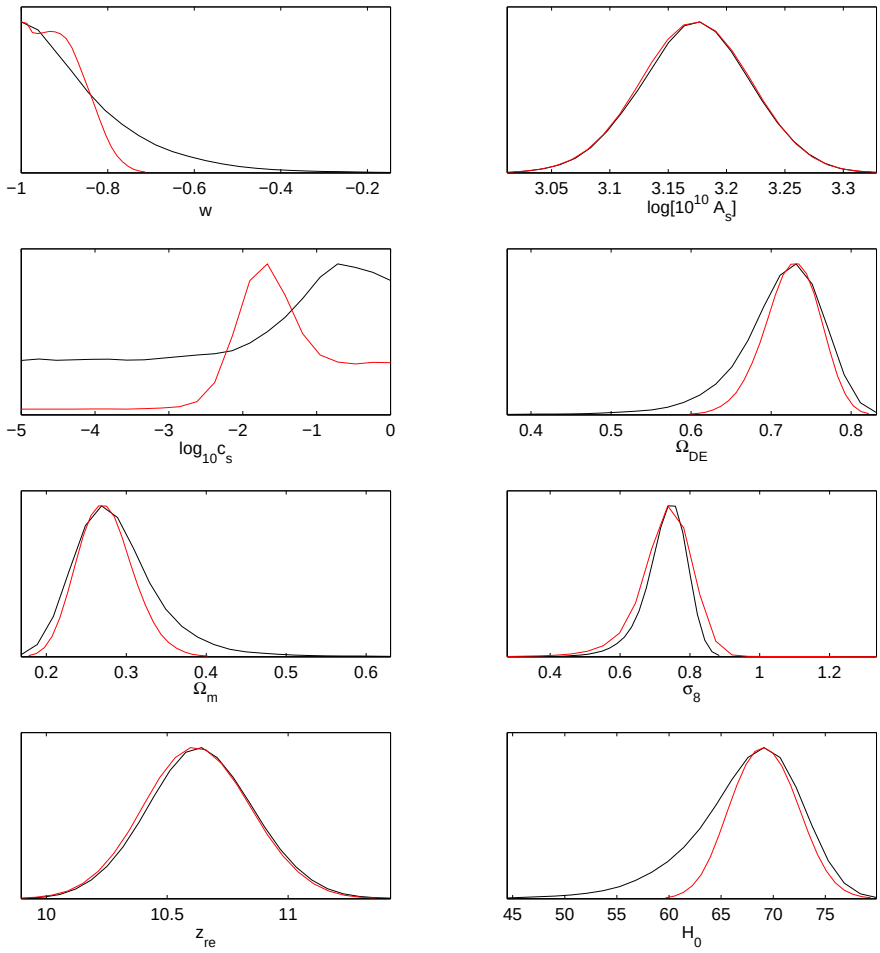

Figure 3.5: 1D marginalized plots for cosmological parameters using WMAP5 + ISW data for a scalar field (black) and elastic dark energy (red) model. The models give similar results, but are quite different with respect to sound speed.

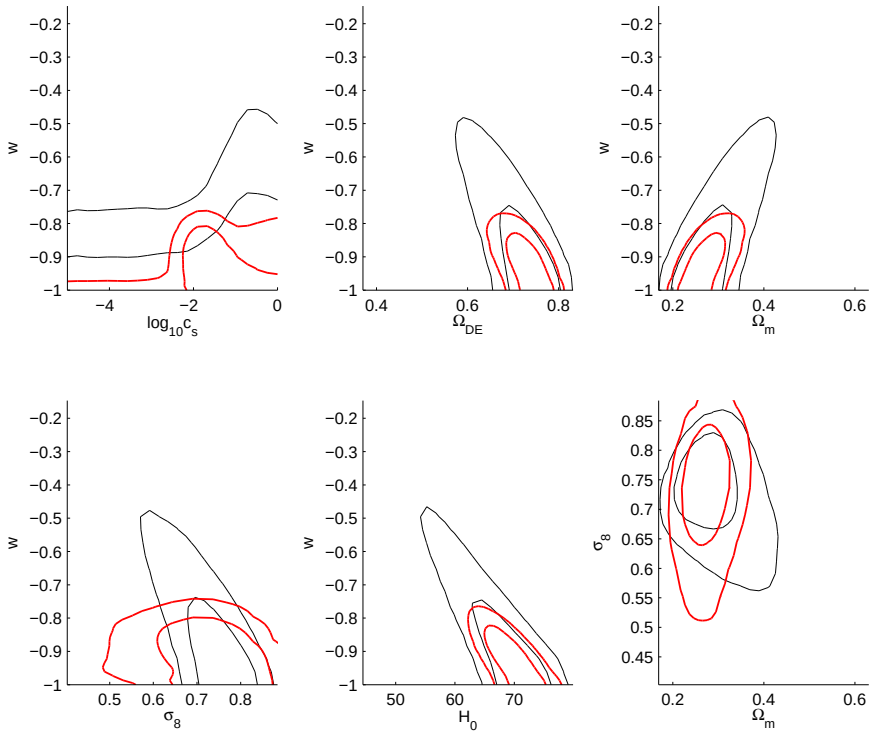

Figure 3.6: 2D marginalized plots for cosmological parameters using WMAP5 + ISW data for a scalar field (black) and elastic dark energy (red) model.

3.3.3 Results using WMAP5 + ISW + SNIa

Like with the weak lensing case, we also included the SNIa data (Kowalski et al. (2008)) in our analysis. The results are plotted in figures 3.7 and 3.8.

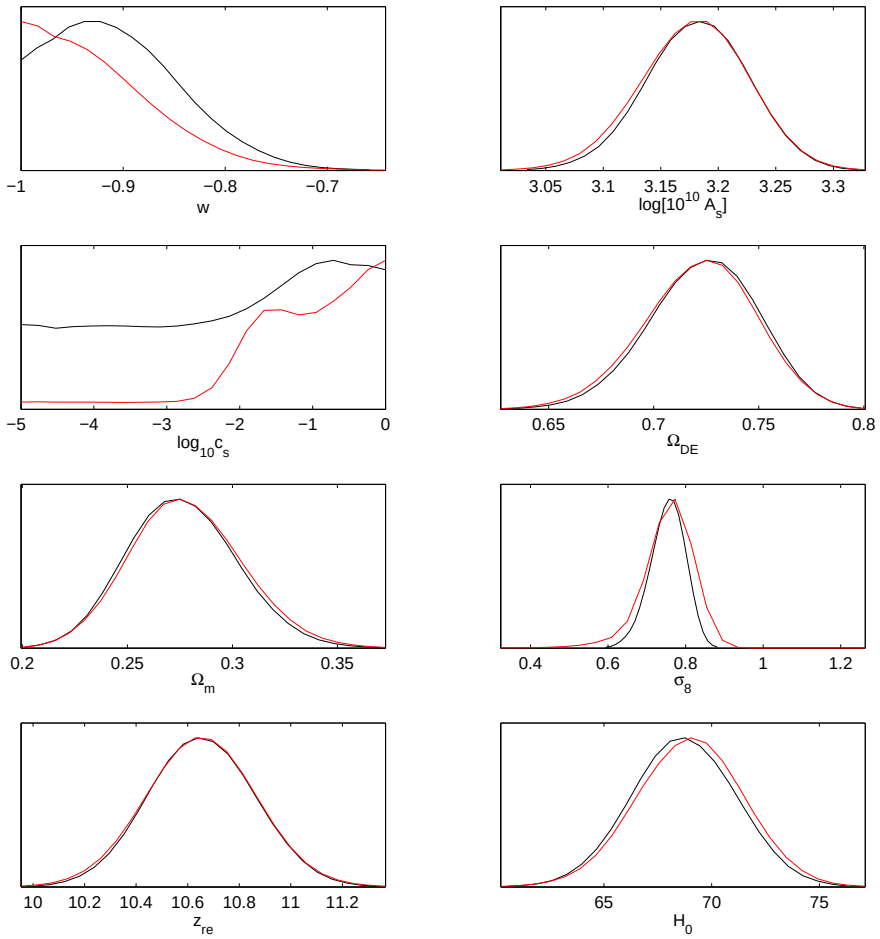

Figure 3.7: 1D marginalized plots for cosmological parameters using WMAP5 + SNIa + ISW data for a scalar field (black) and elastic dark energy (red) model. Again we see the models are similar, but different with respect to the sound speed.

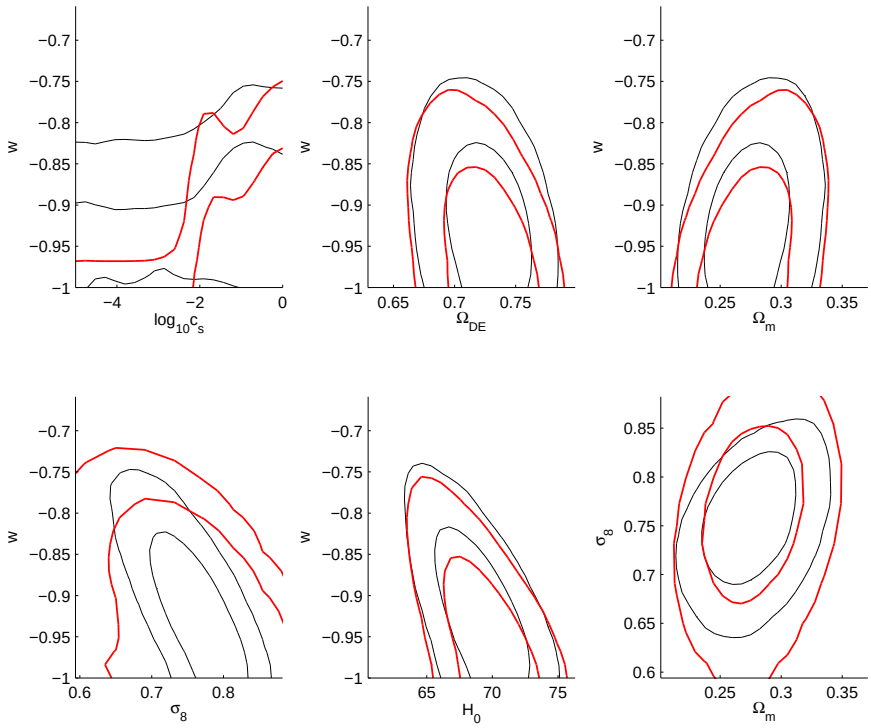

Figure 3.8: 2D marginalized plots for cosmological parameters using WMAP5 + SNIa + ISW data for a scalar field (black) and elastic dark energy (red) model.

Aside from the now familiar cut off in sound speed of the elastic dark energy, the two models appear quite similar. As w approaches -1, the two models tend towards a ΛCDM model and are thus indistinguishable. It is therefore of no surprise that as w is forced closer to -1, achieved by including the SNIa data, smaller differences appear between the two models. We find no lower bound on the scalar field sound speed, but do find a 2σ lower bound of $\log_{10} c_s \geq -3.22$ on the elastic dark energy sound speed.

3.3.4 Varying type Ia supernova

We again include the possibility that the absolute magnitude of a type Ia supernova may vary with redshift, using (Ferramacho et al. (2008)),

$$\Delta m(z) = snK\left(\frac{t_0 - t(z)}{t_0 - t_1}\right), \tag{3.14}$$

The results are shown in figures 3.9 and 3.10. Allowing the variable *snK* to vary has drastically changed the results for an elastic dark energy model. There is now a bimodal solution, corresponding to $w = -1$ and $w = -0.45$. Looking at the 2D plots, we can see that the $w = -1$ solution more closely fits a universe with parameters matching the CCM model. The solution with $w = -0.45$ is correlated with a universe with almost equal amounts of matter and dark energy, $\Omega_\Lambda \sim \Omega_m \sim 0.5$. The scalar field in contrast is less affected by varying *snK* than when using the weak lensing data, with the mean value of *snK* closer to zero.

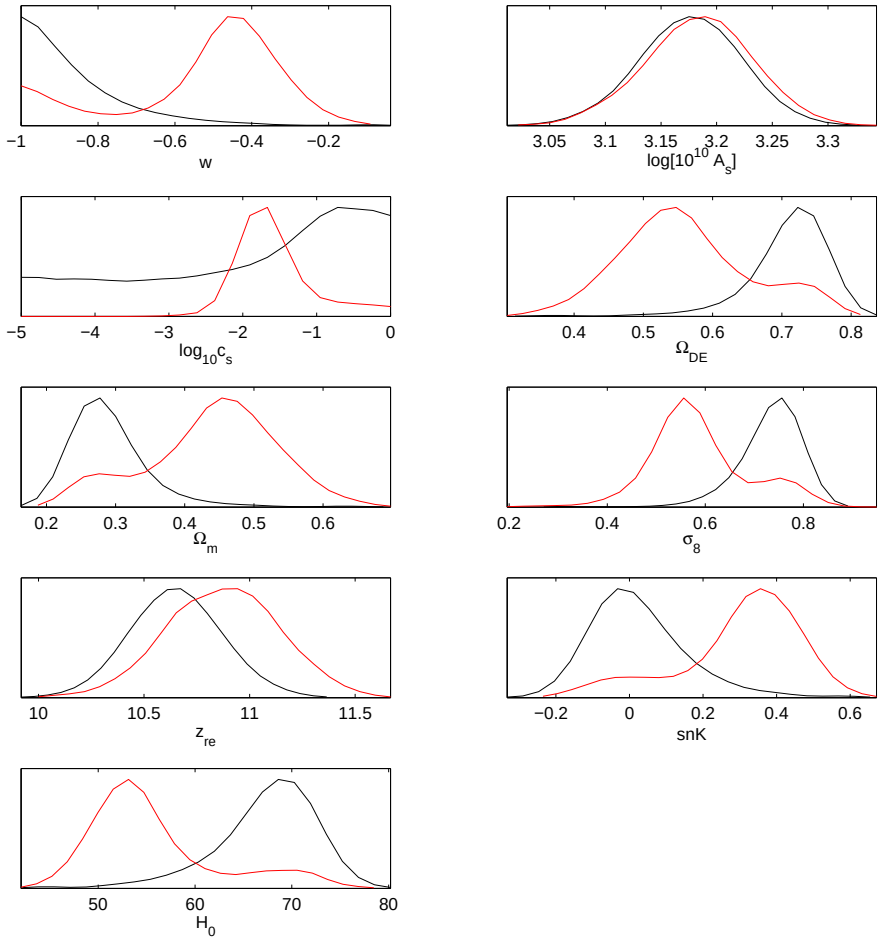

Figure 3.9: 1D marginalized plots for cosmological parameters using WMAP5 + SNIa + *snK* + ISW data for a scalar field (black) and elastic dark energy (red) model. A bimodal solution exists for the elastic dark energy model.

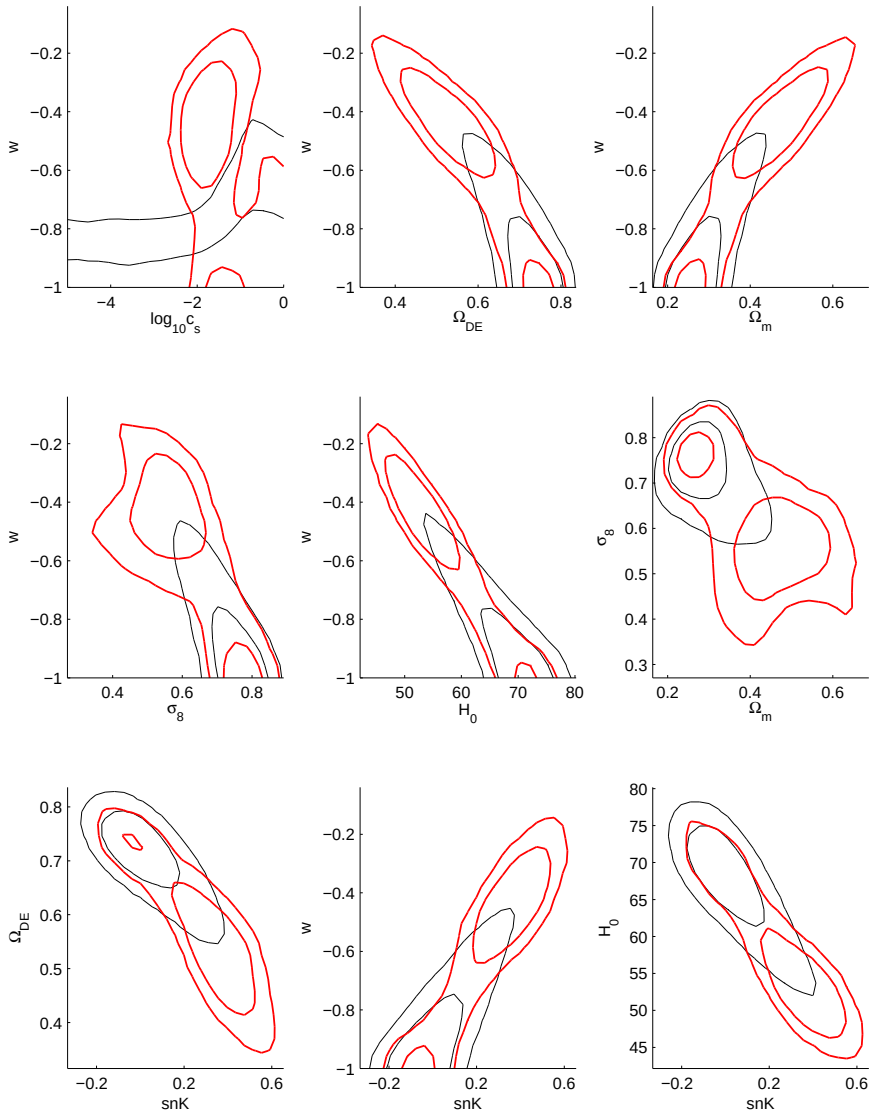

Figure 3.10: 2D marginalized plots for cosmological parameters using WMAP5 + SNIa + *snK* + ISW data for a scalar field (black) and elastic dark energy (red) model.

3.4 Conclusion

In the previous chapter, we were able to show that when using weak lensing data combined with WMAP5 and SNIa observations, a 2σ lower bound in the elastic dark energy speed was found to be $\log_{10} c_s \geq -3.84$. The purpose of the work carried out

within this chapter was to perform a similar analysis and ascertain if a similar result could be obtained, and thus independently confirm a cut off in elastic dark energy sound speed. The ISW effect is observed when correlating matter tracers with CMB anisotropies, and gives us independent evidence of a dark energy component. Such a correlation has been detected numerous times, but at very weak significance levels. In order to constrain cosmological parameters using ISW observations it is better to combine individual measurements of the ISW effect, spanning different redshifts, sky positions, and electromagnetic spectra.

This approach has been done several times before by, among others, Cooray et al. (2005), Corasaniti et al. (2005), Gaztanaga et al. (2006), and Giannantonio et al. (2008). With the necessary modifications to our CAMB and CosmoMC code we were able to confirm the result obtained when using weak lensing data. Referring to figures 3.7 and 3.8 we see that there is a lower limit to the sound speed in the dark energy case. The drop off in likelihood occurs for the same order of magnitude, $\log_{10} c_s \sim -2.5$, as in the weak lensing analysis, and we find a 2σ lower bound of $\log_{10} c_s \geq -3.13$. A significant cut off in w exists for the elastic dark energy model, with a 2σ upper bound of $w \leq -0.81$, whereas the scalar field model is less well bounded, with a 2σ upper bound of $w \leq -0.57$. This was also the case when using the WMAP5 and weak lensing data. A feature also shared with the weak lensing analysis is that the scalar field model is not as tightly constrained, demonstrated in the 2D marginalized plots. This is a direct result of the fact that the sound speed has a much more dramatic effect on elastic dark energy density perturbations, than on the scalar field perturbations, allowing it to take on a greater range of values, and still match observation. By including the SNIa data (figures 3.7 and 3.8), the models look fairly similar, now that the scalar field is more tightly constrained in w. There is still no lower limit to the sound speed for the scalar field, however. As in the previous chapter, this agrees with Weller and Lewis (2003), Bean and Doré (2004) and Hannestad (2005), where the authors argued that placing a lower limit on the sound speed of the scalar field model was not currently possible. In the elastic dark energy case, the 2σ lower bound is $\log_{10} c_s \geq -3.22$. We also find at

the 2σ level, for the elastic dark energy, $w \leq -0.808$ and for the effective scalar field, $w \leq -0.791$. If we compare the marginalised statistics, for each model in the WMAP5 + SNIa + ISW analysis, and the WMAP5 + SNIa + weak lensing analysis, given in tables 3.4 and 2.3 respectively, we see that the numerical results of w and $\log_{10} c_s$ largely agree, within one standard deviation. We notice the ISW analysis favours a larger value of Ω_{DE}, and hence a lower Ω_m, than in the weak lensing analysis.

As in the weak lensing analysis, we explored the possibility that SNIa are not standard candles, where peak luminosity is also a function of redshift. Using the model given in Ferramacho et al. (2008), we can place a 2σ lower bound of $\log_{10} c_s \geq -2.09$ on the sound speed for the elastic dark energy, while we find no lower bound for the scalar field case. A curious result is that a bimodal solution exists for the elastic dark energy model, with an almost even mixture of dark energy and matter. Such a model can in principal be ruled out due to independent measurements on the amount of matter in the universe (see Chapter 1).

3.5 Tables

Below we have tabulated the marginalised statistics for all ISW runs on CosmoMC.

	Scalar Field		**Elastic Dark Energy**	
Parameter	Mean	σ	Mean	σ
$\Omega_b h^2$	0.0224	0.0006	0.0225	0.0006
$\Omega_c h^2$	0.106	0.0059	0.107	0.0056
θ	1.03	0.003	1.04	0.003
w	-0.851	0.133	-0.91	0.0574
n_s	0.962	0.0132	0.964	0.0136
$\log[10^{10} A_s]$	3.17	0.0457	3.17	0.0458
$\log_{10} c_s$	-1.95	1.45	-1.54	0.852
Ω_{DE}	0.710	0.054	0.725	0.033
Age/GYr	13.8	0.202	13.7	0.135
Ω_m	0.289	0.0538	0.274	0.0334
σ_8	0.729	0.0601	0.730	0.0734
z_{re}	10.6	0.214	10.6	0.213
H_0	67.3	5.02	69.1	3.04

Table 3.3: Scalar field and elastic dark energy statistics from the CosmoMC runs using WMAP5 and ISW.

	Scalar Field		**Elastic Dark Energy**	
Parameter	Mean	σ	Mean	σ
$\Omega_b h^2$	0.0224	0.0006	0.0226	0.0006
$\Omega_c h^2$	0.107	0.006	0.109	0.006
θ	10.3	0.003	10.4	0.003
w	-0.9	0.061	-0.92	0.059
n_s	0.96	0.013	0.96	0.014
$\log[10^{10} A_s]$	3.18	0.0431	3.17	0.0454
$\log_{10} c_s$	-2.17	1.46	-1.18	0.966
Ω_{DE}	0.72	0.025	0.721	0.026
Age/GYr	13.8	0.132	13.7	0.131
Ω_m	0.276	0.025	0.278	0.026
σ_8	0.753	0.044	0.755	0.0062
z_{re}	10.6	0.2	10.6	0.21
H_0	68.7	2.34	68.9	2.4

Table 3.4: Scalar field and elastic dark energy statistics from the CosmoMC runs using WMAP5, SNIa and ISW.

	Scalar Field		**Elastic Dark Energy**	
Parameter	Mean	σ	Mean	σ
$\Omega_b h^2$	0.0224	0.0006	0.0225	0.0006
$\Omega_c h^2$	0.106	0.0059	0.108	0.0057
θ	1.03	0.003	1.03	0.003
w	-0.855	0.141	-0.559	0.228
n_s	0.961	0.0132	0.962	0.0148
$\log[10^{10} A_s]$	3.17	0.0451	3.18	0.0471
$\log_{10} c_s$	-1.9	1.44	-1.6	0.69
snK	0.0248	0.131	0.267	0.184
Ω_{DE}	0.709	0.058	0.578	0.102
Age/GYr	13.8	0.221	14.2	0.379
Ω_m	0.29	0.0575	0.421	0.102
σ_8	0.732	0.0642	0.605	0.111
z_{re}	10.6	0.214	10.8	0.271
H_0	67.3	5.17	57.1	7.75

Table 3.5: Scalar field and elastic dark energy statistics from the CosmoMC runs using WMAP5, SNIa, ISW and using the *snK* parameter.

4

Dark energy voids and clustering

For a cosmological constant, the energy density of the dark energy component is homogeneous and isotropic. As we have discussed in the previous chapters, this needn't be the case with other models of dark energy where *w* is not equal to -1. How dark energy density perturbations evolve and their effect on CDM density perturbations is of great interest, and has been explored numerous times within the literature. For example, the implications of dark energy perturbations on observable quantities such as the ISW effect was discussed in Bean and Doré (2004). The authors commented on the increased clustering effect of the scalar field model when lowering its sound speed. Using the first year WMAP data, the authors obtained a 1σ constraint on the sound speed $c_s^2 < 0.04$. A similar analysis performed by Weller and Lewis (2003) did not find a significant constraint on the sound speed, and similarly, no such constraint was found in Hannestad (2005). Other papers on the clustering of dark energy and how such clustering affects CDM perturbations are given in, for example, Bartolo et al. (2004), Hu and Scranton (2004), Nunes and Mota (2006), Unnikrishnan et al. (2008), Avelino et al. (2008), and Basilakos et al. (2009). The clustering in this scalar field model is very weak, making it challenging to constrain its sound speed, a fact demonstrated in the previous two chapters. It has been shown in Battye and Moss (2007), that elastic dark energy density perturbations can be several orders of magnitude larger than a scalar field with the same equation of state and sound speed, a property due to

its intrinsic anisotropic stress.

They showed that lowering the sound speed of dark energy, increased power on small scales in $\delta(k)$. To illustrate this point, we have plotted the power spectrum $P_\delta(k)$ for both dark energy models in figures 4.1 and 4.2. We have assumed $P_\delta(k) = |\delta_{\text{total}}|^2$ and defined $\delta(k) \equiv \sum_i \Omega_i \delta(k)_i$. We have evolved the equations of motion given in Battye and Moss (2007), setting the initial matter and dark energy density and velocity perturbations to zero, and perturbed the metric. It should be noted that the dark energy density contrast, $\delta_{\text{DE}}(k)$, for both the elastic dark energy and scalar field add coherently with the matter perturbation, $\delta_m(k)$. We see that the sound speed for the scalar field makes very little differences to the power spectrum, and hence, as shown in the previous chapters, a scalar field can take on a large range of sound speed values and still agree with observations. When comparing this with the elastic dark energy model and we see the dramatic effect that a lower sound speed has on the power spectrum. As the elastic dark energy speed is lowered, the matter power spectrum is reduced, a property not seen in the scalar field case. Such large changes are what allow us to put a lower limit on the elastic dark energy sound speed.

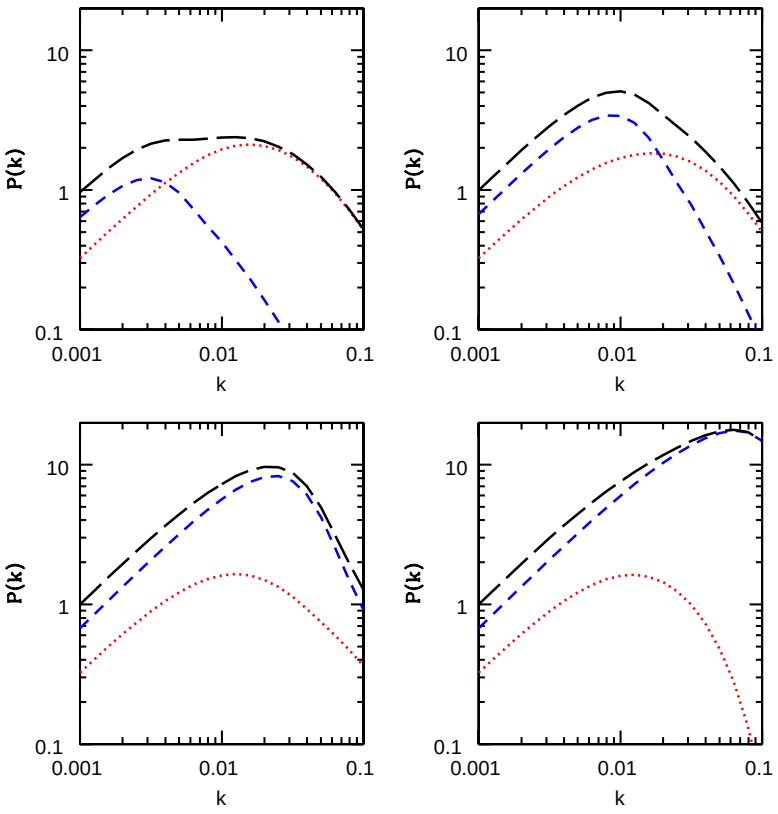

Figure 4.1: A demonstration of the clustering effect of the elastic dark energy model. The black line is the total power spectrum defined as $P_\delta(k) = |\delta_{\text{total}}|^2$ with $\delta_{\text{total}} \equiv \sum_i \Omega_i \delta_i$. The blue and red lines are the individual components making up the total power spectrum, matter and dark energy respectively. The total power spectrum has been normalised at $k = 10^{-3} h\,\text{Mpc}^{-1}$. The dark energy parameters are $w = -2/3$ and starting from the top left and moving clockwise, $c_s^2 = 10^{-2}$, $c_s^2 = 10^{-3}$, $c_s^2 = 10^{-4}$ and $c_s^2 = 10^{-5}$.

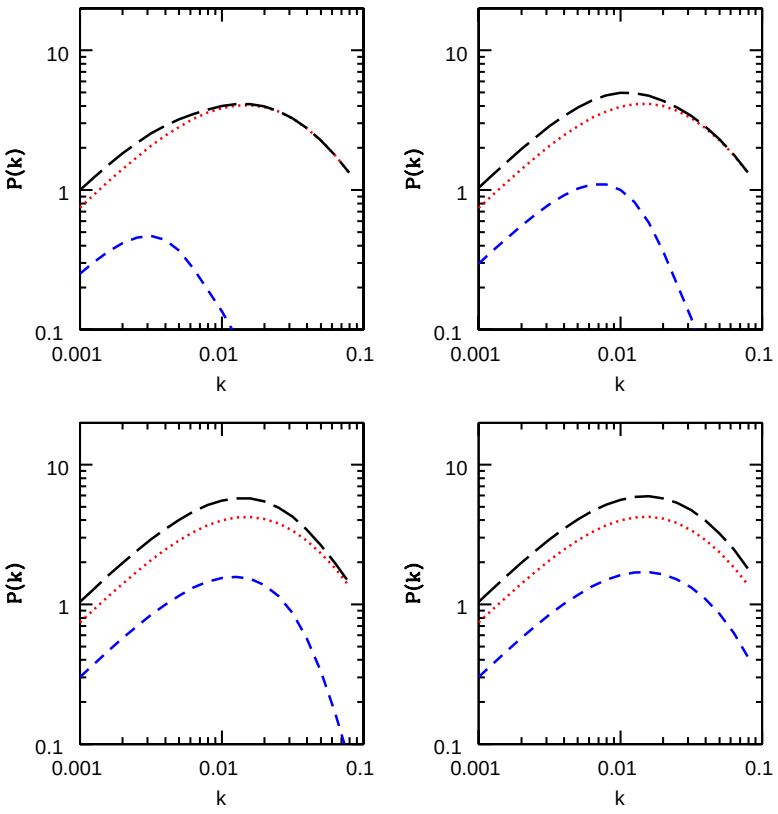

Figure 4.2: The clustering effect of the scalar field dark energy model. The black line is the total power spectrum defined as $P_\delta(k) = |\delta_{\text{total}}|^2$ with $\delta_{\text{total}} \equiv \sum_i \Omega_i \delta_i$. The blue and red lines are the individual components making up the total power spectrum, matter and dark energy respectively. The total power spectrum has been normalised at $k = 10^{-3} h\,\text{Mpc}^{-1}$. The dark energy parameters are $w = -2/3$ and starting from the top left and moving clockwise, $c_s^2 = 10^{-2}$, $c_s^2 = 10^{-3}$, $c_s^2 = 10^{-4}$ and $c_s^2 = 10^{-5}$.

Given the fact that these models allow density perturbations to form, we need to know how dark energy clustering correlates with matter perturbations in the Universe. An interesting suggestion was made by Dutta and Maor (2007), who evolved the equations of motion for a classical scalar field, ϕ, and found that in the presence of collapsing matter, the dark energy density perturbation became negative, forming a void. They found that the opposite was true for regions where there was an underdensity in

the matter density field, the dark energy density perturbation becomes positive.

This work was carried out in the linear regime, with the authors noting that given the sharp increase in scalar field density at late times, a non-linear approach might lead to some interesting results. A different approach was undertaken in Mota et al. (2008), where the authors used the method of matched asymptotic expansion to obtain analytical expressions for the dark energy perturbations that are valid in the linear, quasi-linear, and fully non linear regimes. In the linear and quasi-linear regime the authors showed, as in Dutta and Maor (2007), that the scalar field density contrast became negative in the presence of collapsing matter on super cluster scales. However for virialized clusters of matter, the scalar field density was found to be positive. They argued that while in the results agree with the work of Dutta and Maor (2007) for linear overdensities, ($\delta_m \ll 1$), as these perturbations virialize and their growth becomes non-linear, the dark energy perturbations become positive. A similar result was found by Wang and Fan (2009). They developed an iterative algorithm which was used to examined the evolution of the density perturbations within a scalar field dark energy, in both linear and non-linear regimes, in the presence of a collapsing dark matter halo. While using a different method to Mota et al. (2008), their results do broadly agree, in that underdensities can form within the scalar field, but when entering the non-linear regime, these voids become overdensities.

In this chapter we set up a similar code used in the work of Dutta and Maor (2007), using the elastic dark energy and effective scalar field model (we will refer to the scalar field model we have been using as an effective scalar field in order to distinguish it from the model used in Dutta and Maor (2007)), and evolved our equations of motion in the presence of collapsing matter to ascertain if voids in the dark energy are created with these models.

4.1 The approach of Dutta and Maor

Here we present a reproduction of the results of Dutta and Maor (2007) who solved for δ_ϕ, the density contrast of the scalar field. The line element used by Dutta and Maor (2007) is given by,

$$ds^2 = dt^2 - U(t,r)dr^2 - V(t,r)(d\theta^2 + \sin^2\theta d\phi^2)\,, \tag{4.1}$$

where $U(t,r) = a(t)^2 e^{2\zeta(t,r)}$ and $V(t,r) = r^2 a(t)^2 e^{2\psi(t,r)}$, where, as before $a(t)$ is the scale factor, r is the distance from the centre of the perturbation and ψ and ζ are the metric perturbations. Given the line element the Ricci tensor components are found to be,

$$R_{tt} = \frac{1}{4}\frac{\dot{U}^2}{U^2} + \frac{1}{2}\frac{\dot{V}^2}{V^2} - \frac{1}{2}\frac{\ddot{U}}{U} - \frac{\ddot{V}}{V}\,, \tag{4.2}$$

$$R_{rr} = \frac{1}{2}\ddot{U} + \frac{1}{2}\frac{\dot{V}\dot{U}}{V} - \frac{1}{4}\frac{\dot{U}^2}{U} + \frac{1}{2}\frac{V'U'}{VU} + \frac{1}{2}\frac{V'^2}{V^2} - \frac{V''}{V}\,, \tag{4.3}$$

$$R_{\theta\theta} = \frac{R_{\phi\phi}}{\sin^2\theta} = \frac{1}{2}\ddot{V} + \frac{1}{4}\frac{\dot{V}\dot{U}}{U} + \frac{1}{4}\frac{V'U'}{U^2} + -\frac{1}{2}\frac{V''}{U} + 1\,, \tag{4.4}$$

$$R_{tr} = \frac{1}{2}\frac{\dot{V}V'}{V^2} - \frac{\dot{V}'}{V} + \frac{1}{2}\frac{V'\dot{U}}{VU}\,, \tag{4.5}$$

where dots now refers to derivatives with respect to real time. The Ricci scalar is given by,

$$R = \frac{1}{2}\frac{\dot{U}^2}{U^2} + \frac{1}{2}\frac{\dot{V}^2}{V^2} - \frac{\ddot{U}}{U} - 2\frac{\ddot{V}}{V^2} - \frac{1}{2}\frac{V'^2}{UV^2} + 2\frac{V''}{UV} - \frac{\dot{U}\dot{V}}{UV} - \frac{U'V'}{U^2V} - \frac{2}{V}\,. \tag{4.6}$$

The Ricci tensor can be related to the energy-momentum tensor via an alternate version of Einstein's equations than the one given in Chapter 1,

$$R_{\mu\nu} = K\left(T_{\mu\nu} - \frac{1}{2}g_{\mu\nu}T^{\alpha}_{\alpha}\right)\,, \tag{4.7}$$

where $K = 8\pi$G.

The dark energy component is modelled as a classical scalar field, ϕ, which has an energy-momentum tensor given by,

$$T_{\mu\nu} = \partial_\mu\phi\partial_\nu\phi - g_{\mu\nu}\mathcal{L}\,, \tag{4.8}$$

and the Lagrangian is,

$$\mathcal{L} = \frac{1}{2}(\partial_\mu\phi)^2 - V(\phi)\,. \tag{4.9}$$

The matter component is modelled by a perfect, pressureless fluid which, following Dutta and Maor (2007) has an energy-momentum tensor,

$$T^\mu{}_\nu = \begin{pmatrix} \rho & 0 & 0 & 0 \\ 0 & 0 & 0 & 0 \\ 0 & 0 & 0 & 0 \\ 0 & 0 & 0 & 0 \end{pmatrix}. \tag{4.10}$$

Being uncoupled, both energy-momentum tensors are subject to separate energy conservation constraints, given by,

$$\nabla_\mu T^{\mu\nu}(m) = 0, \quad \nabla_\mu T^{\mu\nu}(\phi) = 0\,. \tag{4.11}$$

From these equations we can now describe the unperturbed background evolution of H, ρ, and ϕ from the following differential equations,

$$3H^2 - K\left[\rho + V + \frac{1}{2}\dot{\phi}^2\right] = 0\,, \tag{4.12}$$

$$\dot{H} + 3H^2 - K\left[\frac{1}{2}\rho + V\right] = 0\,, \tag{4.13}$$

$$\dot{\rho} + 3H\rho = 0\,, \tag{4.14}$$

$$\ddot{\phi} + 3H\dot{\phi} + \frac{dV}{d\phi} = 0\,. \tag{4.15}$$

The next step is to introduce a perturbation in the matter density and scalar field,

$$\rho(t,r) = \rho(t) + \delta\rho(t,r)\,, \tag{4.16}$$

$$\phi(t,r) = \phi(t) + \delta\phi(t,r)\,, \tag{4.17}$$

$$V(\phi + \delta\phi) = V(\phi) + \delta V(\phi, \delta\phi)\,. \tag{4.18}$$

By defining the parameter $\chi \equiv \dot{\zeta} + 2\dot{\psi}$, which is $3\delta H$, the variation in the Hubble parameter around the perturbation, Dutta and Maor (2007) obtained the perturbed Einstein equations, along with the equations of motion. When using a spherical coordinate system, problems can arise when equations have r in the denominator, since when $r \to 0$, infinities can arise. Dutta and Maor (2007) avoid such problems by combining several of the perturbation equations in such a way that $1/r$ terms cancel. There are three perturbation equations to solve, which to linear order are,

$$\delta\dot{\rho} + 3H\delta\rho + \rho\chi = 0\,, \tag{4.19}$$

$$\delta\ddot{\phi} + 3H\delta\dot{\phi} + \delta V' + \dot{\phi}\chi - \frac{1}{a^2}\nabla^2\delta\phi = 0\,, \tag{4.20}$$

$$\dot{\chi} + 2H\chi + K\left(\delta\rho - \delta V + 2\dot{\phi}\delta\dot{\phi}\right) = 0\,. \tag{4.21}$$

We consider the potential $V(\phi) = \frac{1}{2}m^2\phi^2$, as in Dutta and Maor (2007). They also considered a more complex double exponential, but find that both potentials produce the same qualitative result. In our analysis, we choose to factor the units out of the evolution equations by the following redefinitions,

$$\hat{t} = H_0 t\,, \tag{4.22}$$

$$\hat{H} = \frac{H}{H_0}\,, \tag{4.23}$$

$$\hat{\rho} = \frac{\rho}{\rho_{crit}}\,, \tag{4.24}$$

$$\hat{\phi} = \frac{\phi}{M_{pl}}\,, \tag{4.25}$$

$$\hat{m} = \frac{m}{H_0}\,, \tag{4.26}$$

$$\hat{\chi} = \frac{\chi}{H_0}\,, \tag{4.27}$$

where M_{pl} is the Planck mass. These redefinitions give us the following evolution equations, where we have moved to Fourier space,

$$\dot{a} = a\sqrt{\left[\hat{\rho} + \frac{1}{6}\left(\dot{\hat{\phi}}^2 + \hat{m}^2\hat{\phi}^2\right)\right]}, \tag{4.28}$$

$$\dot{\hat{\rho}} = -3\hat{H}\hat{\rho}\,, \tag{4.29}$$

$$\ddot{\hat{\phi}} = -3\hat{H}\dot{\hat{\phi}} - \hat{m}^2\hat{\phi}\,, \tag{4.30}$$

$$\delta\dot{\hat{\rho}}_k + 3\hat{H}\delta\hat{\rho}_k + \hat{\rho}\hat{\chi}_k = 0\,, \tag{4.31}$$

$$\delta\ddot{\hat{\phi}}_k + 3\hat{H}\delta\dot{\hat{\phi}}_k + \left(\hat{m}^2 + \frac{k^2}{H_0^2 a^2}\right)\delta\hat{\phi}_k + \dot{\phi}\hat{\chi}_k = 0\,, \tag{4.32}$$

$$\dot{\hat{\chi}}_k + 2\hat{H}\hat{\chi}_k + \left(\frac{3}{2}\delta\hat{\rho}_k - \hat{m}^2\hat{\phi}\delta\hat{\phi}_k + 2\dot{\hat{\phi}}\delta\dot{\hat{\phi}}_k\right) = 0\,. \tag{4.33}$$

We then evolved these equations with the same matter perturbation given in Dutta and Maor (2007),

$$\delta_m = A\exp\left(-\frac{r^2}{\sigma^2}\right). \tag{4.34}$$

We set $\hat{M} = 1$, $\sigma = 0.01H_{\text{initial}}$, and set other initial conditions so that they give the present day values, $\Omega_m = 0.3$ and $\Omega_\phi = 0.7$. We find that, as in Dutta and Maor (2007), at the centre of an initial matter perturbation, the scalar field component forms underdensities, thus confirming their work. Figure 4.3 shows a plot of the scalar field density perturbation at the centre of the matter perturbation.

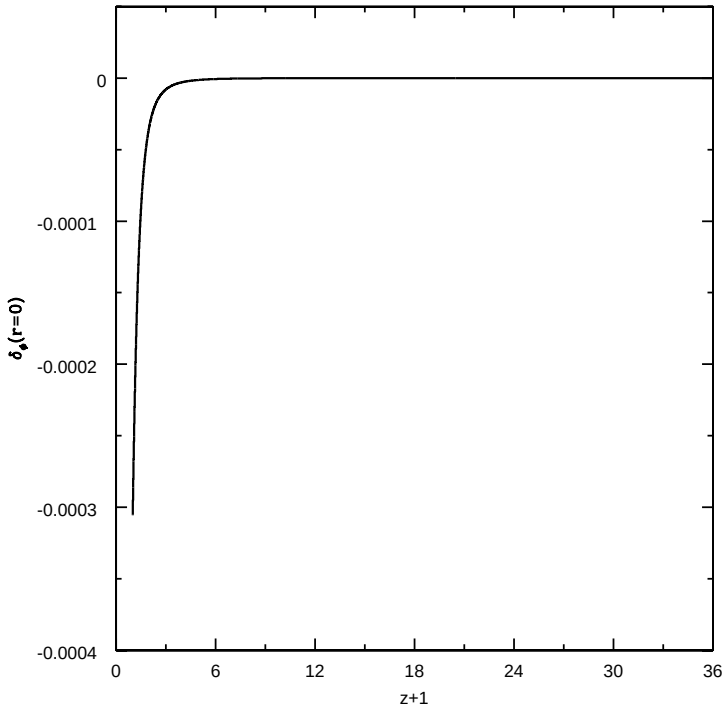

Figure 4.3: Scalar field density plotted against redshift, z, where $z = \frac{1}{a} - 1$, at the centre of the initial matter perturbation. The scalar field density is negative at late times, thus forming a void.

Dutta and Maor (2007) reasoned that a dark energy void is created due to the fact that in a region of space containing a matter overdensity, the expansion is slower than the background due to the force of gravity. This in turn means that the local Hubble value within a matter perturbation is lower than the background value and so offers less Hubble damping to $\delta\ddot{\phi}$. This allows the scalar field to accelerate down its potential at an increased rate to the background. The linear scalar field dark energy density perturbation is given by $\delta\rho_\phi = \dot{\phi}\delta\dot{\phi} + m^2\phi\delta\phi$ where the first term is the kinetic term and the last is the potential term. Initially the kinetic part dominates and the dark energy density increases. The absolute value of $\delta\ddot{\phi}$, initially grows, and then weakens at lower redshift but crucially does not change sign. As such $\delta\dot{\phi}$ tends toward a constant value, and $\delta\phi$ continues to grow. Therefore, at late times the $m^2\phi\delta\phi$ part of $\delta\rho_\phi$ becomes the

dominate term, and since $\delta\phi$ and ϕ have opposite signs, $m^2\phi\delta\phi$ is negative, and hence a dark energy void is formed.

4.2 Elastic dark energy and effective scalar field clustering

Having written a code that confirmed the results found by Dutta and Maor (2007), we now turn our attention to modifying the equations to include an elastic dark energy and effective scalar field with constant equation of state, to ascertain how the models respond to collapsing matter.

4.2.1 Effective scalar field

We can show that a classical scalar field with constant w, where $\rho = \frac{1}{2}\dot{\phi}^2 + V$ and $P = \frac{1}{2}\dot{\phi}^2 - V$ is the same as the effective scalar field model we used earlier in the CMB codes, with the sound speed set at $c_S = 1$. Working in conformal time, where dots indicate derivatives with respect to conformal time, τ, and $\mathcal{H} = \frac{1}{a}\frac{da}{d\tau}$, when w is constant,

$$\dot{\phi}^2 = a^2(1+w)\rho_\phi\,, \tag{4.35}$$

and,

$$V = \frac{1}{2}(1-w)\rho_\phi\,. \tag{4.36}$$

Then, using the chain rule,

$$\frac{dV}{d\phi} = \frac{\dot{V}}{\dot{\phi}} = \frac{\frac{1}{2}(1-w)\dot{\rho}_\phi}{a\sqrt{(1+w)\rho_\phi}} = -\frac{3}{2a}(1-w)\sqrt{1+w}\mathcal{H}\sqrt{\rho_\phi}\,, \tag{4.37}$$

and,

$$\frac{d^2V}{d\phi^2} = -\frac{3(1-w)}{2a^2}\left(\dot{\mathcal{H}} - \frac{1}{2}(5+3w)\mathcal{H}^2\right). \tag{4.38}$$

The equations of motion for the classical scalar field are given in (Hu et al. (1998)),

$$\ddot{\phi} + 2\mathcal{H}\dot{\phi} + a^2\frac{dV}{d\phi} = 0\,, \tag{4.39}$$

$$\delta\ddot{\phi} + 2\mathcal{H}\delta\dot{\phi} + \left(k^2 + a^2\frac{d^2V}{d\phi^2}\right)\delta\phi = S_\phi\,, \tag{4.40}$$

$$\delta\rho_\phi = \frac{\dot{\phi}\delta\dot{\phi}}{a^2} + \frac{dV}{d\phi}\delta\phi\,, \tag{4.41}$$

$$\theta_\phi = \frac{k^2\delta\phi}{\dot{\phi}}\,, \tag{4.42}$$

where S_ϕ is the perturbed metric term, which in the synchronous gauge is $S_\phi = 2\dot{h}\dot{\phi}$. The conformal time derivative of the density contrast, δ_ϕ, is,

$$\frac{d}{dt}\left(\frac{\delta\rho_\phi}{\rho_\phi}\right) = \frac{\delta\dot{\rho}_\phi}{\rho_\phi} + 3\mathcal{H}(1+w)\frac{\delta\rho_\phi}{\rho_\phi}\,, \tag{4.43}$$

which, when combining the equations above, becomes,

$$\dot{\delta_\phi} = -3(1-w)\mathcal{H}\left(\delta_\phi + 3\mathcal{H}(1+w)\frac{V_\phi}{k^2}\right) + (1+w)(S_\phi - V_\phi)\,. \tag{4.44}$$

In a similar manner, the divergence of the fluid velocity, is,

$$\dot{\theta}_\phi = k^2\left(\frac{\delta\dot{\phi}}{\dot{\phi}} - \frac{\ddot{\phi}\delta\phi}{\dot{\phi}^2}\right), \tag{4.45}$$

which, after substitution, becomes,

$$\dot{\theta}_\phi = -2\mathcal{H}\theta_\phi + \frac{k^2}{1+w}\delta_\phi\,. \tag{4.46}$$

These equations are the same as used in our modified CMBFAST and CAMB codes when $c_s^2 = 1$.

4.2.2 Method

We follow a similar method to that shown previously, but with some differences. First we choose to work in the conformal Newtonian gauge for simplicity, since we are only interested in scalar perturbations, coupled with the fact the analysis is done within the horizon. The conformal Newtonian gauge has a line element given in Ma and Bertschinger (1995),

$$ds^2 = a^2(\eta)\left(-d\eta^2\left[1+2\Psi\right] + dx^i dx_i\left[1-2\Phi\right]\right). \tag{4.47}$$

We are also now working in conformal time. The elastic dark energy equations of motion, along with the Einstein equations must be worked out. The curvature part of the Einstein equations are already well known, and are given in Ma and Bertschinger (1995), as,

$$k^2\Phi + 3\mathcal{H}\left(\dot{\Phi} + \mathcal{H}\Psi\right) = -4\pi G a^2 \delta\rho\,, \tag{4.48}$$

$$k\left(\dot{\Phi} + \mathcal{H}\Psi\right) = 4\pi G a^2 \rho(1+w)v^S\,, \tag{4.49}$$

$$\ddot{\Phi} + \mathcal{H}(\dot{\Psi} + 2\dot{\Phi}) + \left(2\frac{\ddot{a}}{a} - \frac{\dot{a}^2}{a^2}\right)\Psi + \frac{k^2}{3}(\Phi - \Psi) = -4\pi G a^2 \delta P\,, \tag{4.50}$$

$$k^2(\Phi - \Psi) = 12\pi G a^2 \rho(1+w)\Theta\,. \tag{4.51}$$

By combining equations 4.48 and 4.49 we arrive at an expression for Φ,

$$k^2\Phi = -4\pi G a^2 \rho\left[\delta + 3\mathcal{H}(1+w)\frac{V_s}{k}\right]. \tag{4.52}$$

Using Battye and Moss (2007) and Carter (1982), we find the the equations of motion for an elastic dark energy model in the conformal Newtonian gauge are,

$$\dot{\delta} = -(1+w)\left[kv^S - 3\dot{\Phi}\right], \tag{4.53}$$

$$\dot{v}^S = -\mathcal{H}(1-3w)v^S + 3\Phi(w-c_s^2)k + \left(\frac{c_s^2\delta}{1+w}\right)k + \Psi k\,. \tag{4.54}$$

As a quick check, we can confirm these are the correct equations by converting them from the conformal gauge to the synchronous gauge, where the latter appear in Battye and Moss (2007). To convert we use the following substitutions, which are given in Ma and Bertschinger (1995),

$$\delta_{con} = \delta_{syn} - 3H\alpha(1+w)\,, \tag{4.55}$$

$$v^S_{con} = v^S_{syn} + \alpha k\,, \tag{4.56}$$

$$\Phi = \eta - \mathcal{H}\alpha\,, \tag{4.57}$$

$$\Psi = \dot{\alpha} + \mathcal{H}\alpha\,, \tag{4.58}$$

where,

$$\alpha = \frac{1}{2k^2}\left(\dot{h} + 6\dot{\eta}\right)\,. \tag{4.59}$$

Substituting these expressions into (4.53) and (4.54), give,

$$\dot{\delta} = -(1+w)\left[kv^S + \frac{\dot{h}}{2}\right]\,, \tag{4.60}$$

$$\dot{v}^S = -v^S\mathcal{H}(1-3w) + 3k\eta(w-c_s^2) + \left(\frac{c_s^2k\delta}{1+w}\right)\,, \tag{4.61}$$

which are the equations given in Battye and Moss (2007), thus confirming that (4.53) and (4.54) are correct. We evolve the spatial perturbation to the metric, Φ, using equation (4.48). By rearranging equation (4.51) we can get an expression for the temporal perturbation to the metric, Ψ, given by,

$$\Psi = \frac{-12\pi G a^2 \rho (1+w)\Theta}{k^2} + \Phi\,, \tag{4.62}$$

where Θ is given by,

$$\Theta = \frac{2}{3}\frac{w}{1+w}\Pi = (c_s^2 - w)\left(\frac{-\delta}{1+w} + 3(\Phi - \Phi_{ini})\right). \tag{4.63}$$

We use the same initial conditions as in the previous section, starting the equations at $z = 35$, and define the same matter perturbation given by,

$$\delta_m = A \exp\left(-\frac{r^2}{\sigma^2}\right). \tag{4.64}$$

When converting this to Fourier space, we note that the imaginary part is an odd integrand, so integrating over a symmetrical range is just zero. The Fourier Transform of a Gaussian is another Gaussian. We are also only considering one perturbation and as such, no phase information is lost in our approach. We set $A = 0.1$ and $\sigma = 0.01\mathcal{H}_{ini}$. We set all other values to zero, except Φ which is dependent on δ_m. Since we are using the conformal Newtonian gauge we choose to output the density contrast in the gauge invariant quantity, $\delta = \delta_{con} + 3\mathcal{H}(1+w)v_c/k$, which is the density contrast in the rest frame of the fluid. We only consider what happens at the centre of the matter perturbation, $r = 0$.

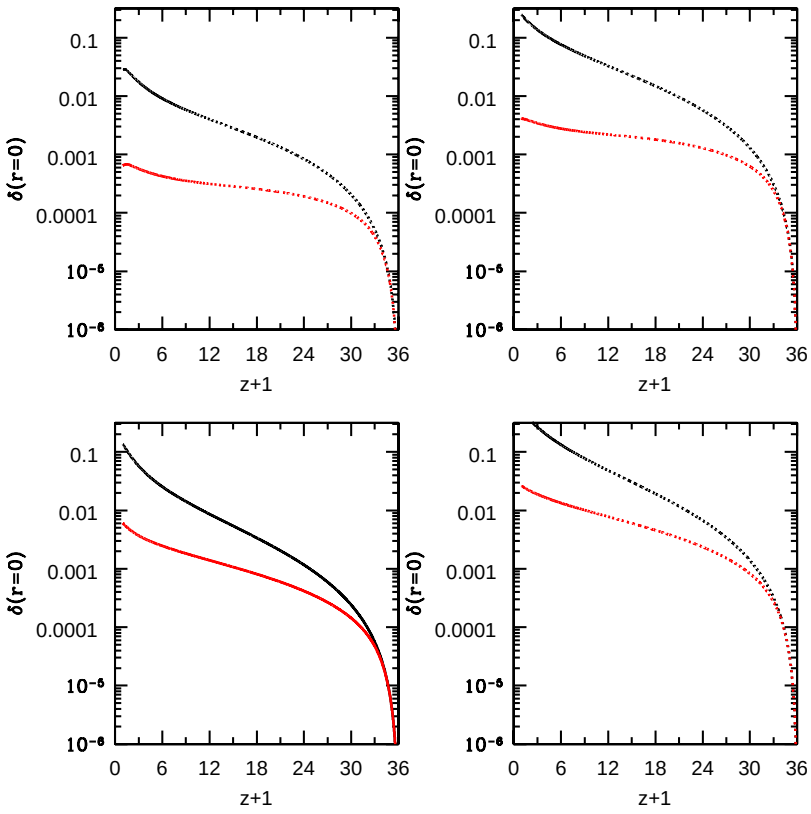

Figure 4.4: Plots showing how the density perturbation of the dark energy, at the centre of the matter perturbation, evolve with time. From bottom left, moving clockwise, elastic dark energy with $w = -0.9$, scalar field with $w = -0.9$, scalar field with $w = -0.4$, and elastic dark energy with $w = -0.4$. The black lines have $c_s^2 = 10^{-4}$ and the red lines have $c_s^2 = 1$.

We see that in figure 4.4 neither the elastic dark energy, nor the effective scalar field model form voids. Instead the density perturbations grow, with the gradient being relatively large at first. The gradient weakens, before increasing again for all models. Larger equations of state for the dark energy give a smaller density perturbation for both matter and dark energy components. This is not surprising as looking at equation (4.60), the term $(1 + w)$ means that the larger w, the larger the absolute value of $\dot{\delta}$. Lowering the sound speed increases the magnitude of the density perturbation which

has been shown earlier. If we display the matter and dark energy density perturbations on the same plot we see that the dark energy density perturbation, after increasing by several orders of magnitude in a short time scale, begin to level out and follow the matter density perturbation, as we can see in figure 4.5.

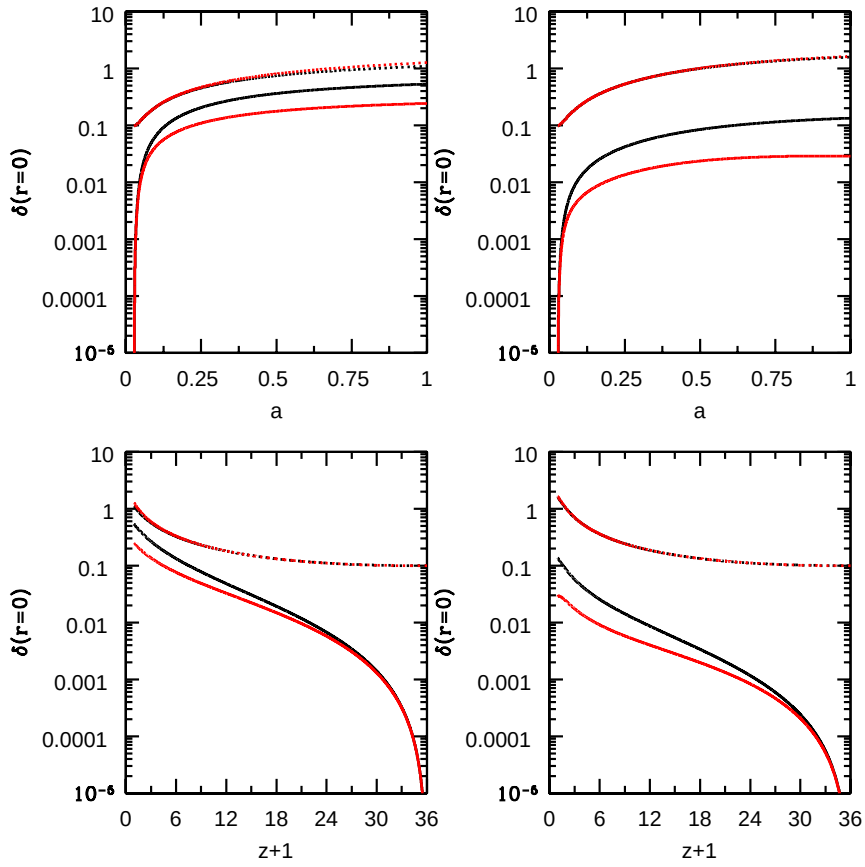

Figure 4.5: Plots showing the dark energy, and matter density perturbation evolving as a function of a, and $1 + z$. The plots on the left have $w = -0.4$, the plots on the right have $w = -0.9$. The sound speed is set at $c_s^2 = 10^{-4}$. The dotted lines are the matter density perturbations and the solid lines the dark energy density perturbations. Top plots are against the scale factor a, and the bottom plots are against $1 + z$. The red line corresponds to using an effective scalar field model, and the black line corresponds to an elastic dark energy model.

4.3 Conclusion

In this chapter we set out to determine whether, using the same method as in Dutta and Maor (2007), elastic dark energy and the effective scalar field would create voids as a response to collapsing matter. Considering only two components, non relativistic matter and dark energy, we evolved the cosmological equations, along with the perturbed equations of motion for the matter and dark energy components. We set a positive initial Gaussian matter perturbation and kept the initial dark energy perturbation at zero. Looking at figures 4.4 and 4.5 we see that the growth of the dark energy perturbation is initially very rapid. This is a consequence of the artificial initial conditions, where the dark energy perturbation has been set to zero. This sharp gradient occurs in the first few time steps, no matter what time we start evolving our equations from. In the case studied in Dutta and Maor (2007), after an initial growth, the scalar field density contrast become negative, turning over at $z \sim 10-11$, depending on the initial width of the matter perturbation. In both the elastic dark energy, and effective scalar field models, the density contrast remains positive, and continues to grow. Perhaps unsurprisingly the elastic dark energy density contrast is always larger than the effective scalar field's. We have seen that elastic dark energy's effect on observable quantities is to in general enhance them over the effective scalar field model. An interesting observation is that the matter density contrast is lower when using an elastic dark energy model than when using the effective scalar field model. In figure 4.6 we have replotted the top left plot of figure 4.5 to better illustrate this.

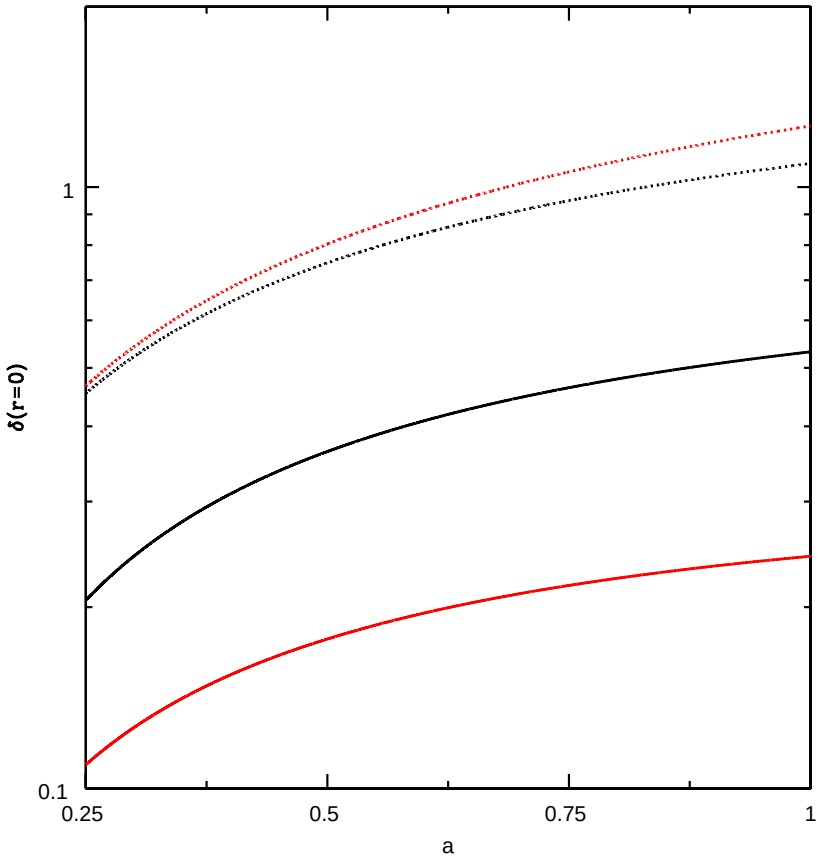

Figure 4.6: A plot highlighting the reduced power in the matter perturbation when using an elastic dark energy model. The dotted lines correspond to δ_m and the solid lines to $\delta_{\rm DE}$. The red lines indicate when an effective scalar field is used, and black when an elastic dark energy model is used. The equation of state is $w = -0.4$, and the sound speed is $c_s^2 = 10^{-4}$.

In figure 4.7 we have plotted $\left(\frac{\delta_m(\text{ESF})}{\delta_m(\text{EDE})} - 1\right) \times 100\%$ against the scale factor, where δ_m(ESF) refers to the matter density perturbation using an effective scalar field, and δ_m(EDE) refers to the matter density perturbation using an elastic dark energy model. We see that the suppression of the matter density contrast is highly dependent on both the dark energy equation of state, with a larger w causing a greater difference, and the sound speed, with a lower sound speed increasing the difference. It must be stressed

that our analysis has only be conducted in the linear regime, and our results are applicable on the order of the supercluster scale ($\sim$ 100 Mpc), since elastic dark energy is a linear theory. Therefore whether this lack of growth continues into the non-linear regime is unknown.

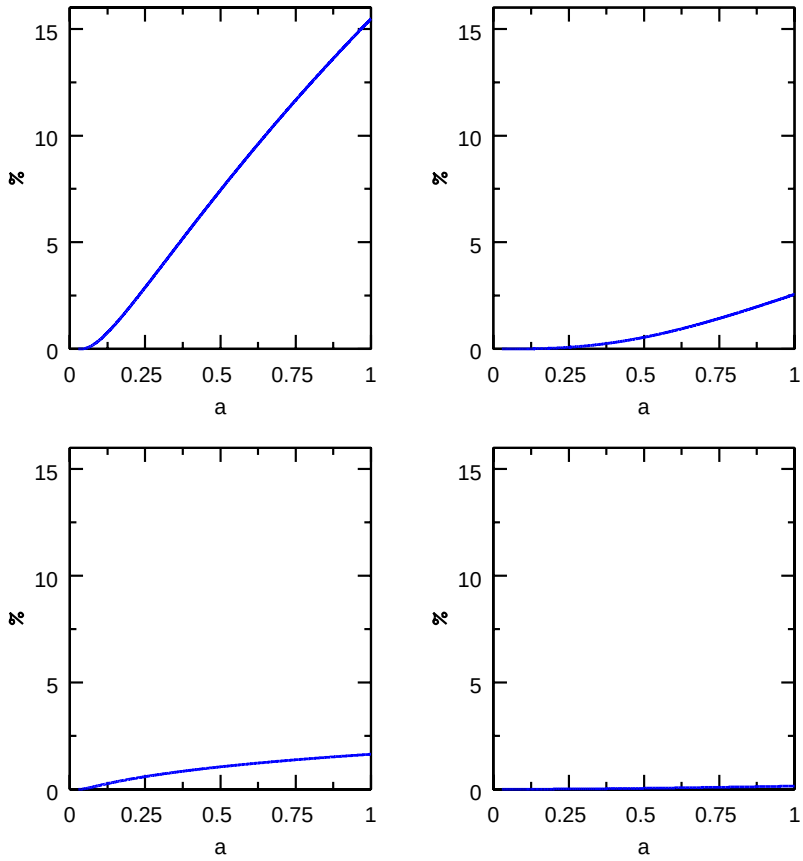

Figure 4.7: Highlighting the percentage difference between the matter perturbation, when using an effective scalar field, and elastic dark energy. We have plotted $\left(\frac{\delta_m(\text{ESF})}{\delta_m(\text{EDE})} - 1\right) \times 100\%$ against the scale factor, a. The top plots have $c_s^2 = 10^{-4}$ and the bottom have $c_s^2 = 1$. The plots on the left have $w = -0.4$ and the plots on the right have $w = -0.9$.

The fact that the matter density contrast is lower when using elastic dark energy than when using the effective scalar field can also be seen when using the CMB codes. As

$w \to -1$ and $c_s^2 \to 1$, the differences become increasingly small. Since the equation of state is measured to be close to -1, and because it is difficult to separate matter and dark energy perturbations, such an effect will be very difficult to detect observationally.

We can now say why our models did not produce the voids seen when using a classical scalar field. In the classical scalar field case, ϕ, the potential term in δ_ϕ ultimately becomes dominate in the presence of collapsing matter, and this is why the void is created. When we fix w, we fix the perturbed potential, and so this term can never come to dominate. When w is constant the density of the scalar field is given by,

$$\rho = \frac{1}{2}\dot{\phi}^2 \left[1 + \frac{1-w}{1+w}\right]. \tag{4.65}$$

The term in the square brackets is a constant, and so by introducing a perturbation, $\phi + \delta\phi$, this becomes

$$\delta\rho = \dot{\phi}\delta\dot{\phi} \left[1 + \frac{1-w}{1+w}\right]. \tag{4.66}$$

The term $\dot{\phi}\delta\dot{\phi}$ continues to grow, as it does in the Dutta and Maor (2007) case. But unlike that case where the $\phi\delta\phi$ term grows and becomes dominant over the $\dot{\phi}\delta\dot{\phi}$ term, the potential is unable to change. It is for this reason that the effective scalar field and the elastic dark energy models cannot form voids.

5

Discussion of results and future work

The aim of the work contained within this thesis was to examine an elastic dark energy model and highlight observational differences between such a model, and an effective scalar field model (Bean and Doré (2004), and Weller and Lewis (2003)). It was shown in the work by Battye and Moss (2007), that when Elastic Dark Energy's sound speed is lowered, it starts to exhibiting clustering properties similar to CDM. If the clustering is sufficiently large, it will affect a range of cosmological measurements. With this direct relation between dark energy, and what we can experimentally observe, we are able to constrain dark energy parameters for different models. Using the CMB codes, CMBFAST (Seljak and Zaldarriaga (1996)), CAMB (Lewis et al. (2000)) and CosmoMC (Lewis and Bridle (2002)), coupled with WMAP5 (Dunkley et al. (2009)), SNIa (Kowalski et al. (2008)), weak lensing (Fu et al. (2008)) and ISW (Gaztanaga et al. (2006)) data, we were able to show that while there is no limit on the sound speed of the effective scalar field model, there is a lower bound on the elastic dark energy sound speed. While using WMAP5 and SNIa data, no such lower bound was evident, but when either weak lensing or ISW data was included the differences in the models become apparent. Using WMAP5, SNIa and weak lensing data gave a lower bound of $\log_{10} c_s \geq -3.84$ at the 2σ level, while using WMAP5, SNIa and ISW data gave a lower bound of $\log_{10} c_s \geq -3.22$ at the 2σ level. Our work is consistent with that of other authors performing similar analysis on the effective scalar field model, in that

no lower limit was found for the sound speed (see for example Bean and Doré (2004), Weller and Lewis (2003) and Hannestad (2005)).

The equation of state was more tightly constrained for the elastic dark energy model than for the effective scalar field model, when using both weak lensing and ISW data. Using WMAP5, SNIa and weak lensing data, we found a 2σ upper limit on $w \leq -0.872$, while for the effective scalar field, $w \leq -0.787$. Using the ISW data combined with WMAP5 and SNIa data, we find for the elastic dark energy, $w \leq -0.808$ and for the effective scalar field, $w \leq -0.791$, also at the 2σ level. An obvious first step to attempt to improve our constraints on elastic dark energy's sound speed and equation of state would be to combine the weak lensing, ISW, WMAP5, and SNIa data.

Using a model proposed in Ferramacho et al. (2008) for the evolution of SNIa, we repeated our analysis, and including the parameter *snK*, which represented the change in magnitude at a given redshift. In both the weak lensing and ISW cases, we were still able to show a lower bound to the elastic dark energy sound speed, where $\log_{10} c_s \geq -3.50$, and $\log_{10} c_s \geq -2.09$ respectively. No bound was found for the effective scalar field. While the cut off in sound speed is still present, the values of the cosmological parameters are not similar, due to the bimodal solution when using the ISW data. It would be interesting to combine the weak lensing and ISW data together with the WMAP5 and SNIa data as this could possibly remove the bimodal solution.

We also showed that the elastic dark energy model does not form voids, as classical scalar fields have been noted to do in the linear regime (Dutta and Maor (2007), Mota et al. (2008), and Wang and Fan (2009)). We noted that elastic dark energy clustering does affect the amplitude of the CDM clustering, by lowering it relative to an effective scalar field model. This property is heavily dependent on the equation of state, and the difference between the two models becomes greater as w tends towards zero. In order to improve this analysis, we would need develop a non-linear theory of elastic dark energy, and probe smaller length scales.

5.1 Future relevant missions

Our CosmoMC analysis relies on the quality of the data we have used, after all, we are testing a theoretical model against what is actually observed. Planck is an upcoming mission to map out full sky maps of the CMB anisotropies, over nine frequency bands, improving upon the resolution mapped out by WMAP. However given that our work is based in the linear regime, and the low multiple anisotropies are already well constrained, Planck won't make a significant difference to our work. It will however be an important tool for cosmology, improving both constraints on cosmological parameters, and astrophysical foreground models. What would be more significant in improving our work, is improved large scale structure data, covering more of the sky. There are a few experiments currently being developed with this goal in mind. A relevant upcoming mission is the Dark Energy Survey (DES). The DES will build a galaxy catalogue containing more than 300 millions objects, measuring the number, and spatial distribution of galaxy clusters in the $0.1 < z < 1.4$ range, and the record the luminosity distances for around 2000 supernovae in the $0.3 < z < 0.8$ range. The DES will also measure weak lensing shear out to $z \sim 1$. The Large Synoptic Survey Telescope (LSST) is another planned survey that is intended to map out the entire sky in multiple frequency bands. Due to its unique setup, the LSST will be able to measure weak lensing shear, supernovae, baryonic acoustic oscillations, and map out clusters, all as a function of redshift. By combining this data, further constraints on dark energy should be possible.

References

N. Afshordi, Y.-S. Loh, and M. A. Strauss. Cross-Correlation of the Cosmic Microwave Background with the 2MASS Galaxy Survey: Signatures of Dark Energy, Hot Gas, and Point Sources. *Phys. Rev. D*, 69:083524, 2004, arXiv:astro-ph/0308260.

S. W. Allen et al. Improved constraints on dark energy from Chandra X-ray observations of the largest relaxed galaxy clusters. *MNRAS*, 383:879–896, 2008, arXiv:0706.0033.

L. An, S. Brooks, and A. Gelman. Stephen brooks and andrew gelman. *Journal of Computational and Graphical Statistics*, 7:434–455, 1998.

C. Armendariz-Picon, V. Mukhanov, and P. J. Steinhardt. Essentials of k-essence. *Phys. Rev. D*, 63:103510, 2001.

P. P. Avelino, L. M. G. Beca, and C. J. A. P. Martins. Clustering Properties of Dynamical Dark Energy Models. *Phys. Rev. D*, 77:101302, 2008, arXiv:0802.0174.

M. Bartelmann and P. Schneider. Weak Gravitational Lensing. *Phys. Rept*, 340:291–472, 2001, arXiv:astro-ph/9912508.

N. Bartolo, P. S. Corasaniti, A. R. Liddle, and M. Malquarti. Perturbations in cosmologies with a scalar field and a perfect fluid. *Phys. Rev. D*, 70:043532, 2004, arXiv:astro-ph/0311503.

S. Basilakos, J. C. Bueno Sanchez, and L. Perivolaropoulos. The spherical collapse model and cluster formation beyond the Λ cosmology: Indications for a clustered dark energy? *Phys. Rev. D.*, 80:043530, 2009, arXiv:0908.1333.

R. A. Battye and A. Moss. Cosmological perturbations in elastic dark energy models. *Phys. Rev. D*, 76(2):023005, 2007.

R. Bean and O. Doré. Probing dark energy perturbations: The dark energy equation of state and speed of sound as measured by wmap. *Phys. Rev. D*, 69(8):083503, 2004.

C. L. Bennett et al. First Year Wilkinson Microwave Anisotropy Probe (WMAP) Observations: Preliminary Maps and Basic Results. *ApJS*, 148:1, 2003, arXiv:astro-ph/0302207.

M. C. Bento, O. Bertolami, and A. A. Sen. Generalized chaplygin gas, accelerated expansion, and dark-energy-matter unification. *Phys. Rev. D*, 66(4):043507, 2002.

O. Bertolami. The cosmological constant problem: a user's guide. *Int. J. Mod. Phys.*, D18:2303–2310, 2009, arXiv:0905.3110.

E. Boldt. The cosmic x-ray background. *Physics Reports*, 146(4):215 – 257, 1987.

S. Boughn and R. Crittenden. A correlation of the cosmic microwave sky with large scale structure. *Nature*, 427:45–47, 2004, arXiv:astro-ph/0305001.

S. Burles, K. M. Nollett, and M. S. Turner. Big-Bang Nucleosynthesis Predictions for Precision Cosmology. *ApJ.*, 552:L1–L6, 2001, arXiv:astro-ph/0010171.

R. R. Caldwell, M. Kamionkowski, and N. N. Weinberg. Phantom Energy and Cosmic Doomsday. *Phys. Rev. Lett.*, 91:071301, 2003, arXiv:astro-ph/0302506.

B. Carter. Interaction of gravitational waves with an elastic solid medium. 1982, arXiv:gr-qc/0102113.

T.-C. Chang, A. Refregier, and D. J. Helfand. Weak lensing by large-scale structure with the FIRST Radio Survey. *ApJ*, 617:794–810, 2004, arXiv:astro-ph/0408548.

J. J. Condon et al. The NRAO VLA Sky survey. *ApJ*, 115:1693–1716, 1998.

A. Cooray, P.-S. Corasaniti, T. Giannantonio, and A. Melchiorri. An indirect limit on the amplitude of primordial gravitational wave background from CMB - galaxy cross correlation. *Phys. Rev. D*, 72:023514, 2005, arXiv:astro-ph/0504290.

P.-S. Corasaniti, T. Giannantonio, and A. Melchiorri. Constraining dark energy with cross-correlated CMB and Large Scale Structure data. *Phys. Rev. D*, 71:123521, 2005, arXiv:astro-ph/0504115.

R. G. Crittenden and N. Turok. Looking for Λ with the Rees-Sciama Effect. *Phys. Rev. Lett.*, 76:575, 1996, arXiv:astro-ph/9510072.

R. de Putter and E. V. Linder. Kinetic k-essence and Quintessence. *Astropart. Phys.*, 28:263–272, 2007, arXiv:0705.0400.

S. Dodelson. *Modern Cosmology*. Elsevier Science, 2003.

J. Dunkley, E. Komatsu, M. R. Nolta, D. N. Spergel, D. Larson, G. Hinshaw, L. Page, C. L. Bennett, B. Gold, N. Jarosik, J. L. Weiland, M. Halpern, R. S. Hill, A. Kogut,

M. Limon, S. S. Meyer, G. S. Tucker, E. Wollack, and E. L. Wright. Five-Year Wilkinson Microwave Anisotropy Probe (WMAP) Observations: Likelihoods and Parameters from the WMAP data. *ApJS*, 180:306–376, 2009, arXiv:0803.0586.

S. Dutta and I. Maor. Voids of dark energy. *Phys. Rev. D*, 75(6):063507, 2007.

L. D. Ferramacho, A. Blanchard, and Y. Zolnierowski. Constraints on C.D.M. cosmology from galaxy power spectrum, CMB and SNIa evolution. *A&A*, 499(1):21–29, 2008, arXiv:0807.4608.

P. Fosalba, E. Gaztanaga, and F. Castander. Detection of the ISW and SZ effects from the CMB-Galaxy correlation. *ApJ*, 597:L89–92, 2003, arXiv:astro-ph/0307249.

L. Fu et al. Very weak lensing in the CFHTLS Wide: Cosmology from cosmic shear in the linear regime. *A&A*, 479:9–25, 2008, arXiv:0712.0884.

E. Gaztanaga, M. Manera, and T. Multamaki. New light on dark cosmos. *MNRAS*, 365:171–177, 2006, arXiv:astro-ph/0407022.

T. Giannantonio et al. A high redshift detection of the integrated Sachs-Wolfe effect. *Phys. Rev. D*, 74:063520, 2006, arXiv:astro-ph/0607572.

T. Giannantonio et al. Combined analysis of the integrated Sachs-Wolfe effect and cosmological implications. *Phys. Rev. D*, 77:123520, 2008, arXiv:0801.4380.

L. Grego, J. E. Carlstrom, E. D. Reese, G. P. Holder, W. L. Holzapfel, M. K. Joy, J. J. Mohr, and S. Patel. Galaxy cluster gas mass fractions from sunyaev-zeldovich effect measurements: Constraints on m. *ApJ*, 552(1):2, 2001.

T. Hamana et al. Cosmic shear statistics in the Suprime-Cam 2.1 sq deg field: Constraints on Ω_m and σ_8. *ApJ*, 597:98–110, 2003, arXiv:astro-ph/0210450.

S. Hannestad. Constraints on the sound speed of dark energy. *Phys. Rev. D*, 71:103519, 2005, arXiv:astro-ph/0504017.

B. M. S. Hansen et al. The White Dwarf Cooling Sequence of the Globular Cluster Messier 4. *ApJ*, 574:L155–L158, 2002, arXiv:astro-ph/0205087.

M. Hicken et al. Improved Dark Energy Constraints from 100 New CfA Supernova Type Ia Light Curves. *ApJ.*, 700:1097–1140, 2009, arXiv:0901.4804.

H. Hoekstra et al. A measurement of weak lensing by large scale structure in RCS fields. *ApJ*, 572(1):55, 2002, arXiv:astro-ph/0202285.

W. Hu and R. Scranton. Measuring Dark Energy Clustering with CMB-Galaxy Correlations. *Phys. Rev. D*, 70:123002, 2004, arXiv:astro-ph/0408456.

W. Hu, U. Seljak, M. J. White, and M. Zaldarriaga. A Complete Treatment of CMB Anisotropies in a FRW Universe. *Phys. Rev. D*, 57:3290–3301, 1998, arXiv:astro-ph/9709066.

D. Huterer. Weak lensing and dark energy. *Phys. Rev. D*, 65(6):063001, 2002.

N. Jarosik et al. Seven-Year Wilkinson Microwave Anisotropy Probe (WMAP) Observations: Sky Maps, Systematic Errors, and Basic Results. *ApJS*, 192:14, 2011, arXiv:1001.4744.

M. J. Jee, R. White, H. Ford, G. Illingworth, J. Blakeslee, et al. Weak-lensing detection at $z \sim 1.3$: measurement of the two lynx clusters with advanced camera for surveys. *ApJ*, 642(2):720, 2006, arXiv:astro-ph/0601334.

R. Jimenez and P. Padoan. A new method to determine Globular Cluster ages. 1996, arXiv:astro-ph/9602014.

N. Kaiser, G. Wilson, and G. A. Luppino. Large-Scale Cosmic Shear Measurements. 2000, arXiv:astro-ph/0003338.

A. Y. Kamenshchik, U. Moschella, and V. Pasquier. An alternative to quintessence. *Phys. Lett.*, B511:265–268, 2001, arXiv:gr-qc/0103004.

E. Komatsu et al. Five-Year Wilkinson Microwave Anisotropy Probe (WMAP1) Observations: Cosmological Interpretation. *ApJS*, 180:330–376, 2009, arXiv:0803.0547.

M. Kowalski et al. Improved Cosmological Constraints from New, Old and Combined Supernova Datasets. *ApJ*, 686:749–778, 2008, arXiv:0804.4142.

L. M. Krauss. Implications of the wmap age measurement for stellar evolution and dark energy. *ApJ*, 596:L1, 2003.

A. Lewis and S. Bridle. Cosmological parameters from CMB and other data: a Monte-Carlo approach. *Phys. Rev. D*, 66:103511, 2002, arXiv:astro-ph/0205436.

A. Lewis, A. Challinor, and A. Lasenby. Efficient computation of CMB anisotropies in closed FRW models. *ApJ*, 538:473–476, 2000, arXiv:astro-ph/9911177.

A. Liddle. *An Introduction to Modern Cosmology*. Wiley, 2003.

C. Ma and E. Bertschinger. Cosmological Perturbation Theory in the Synchronous and Conformal Newtonian Gauges. *ApJ*, 455:7, 1995, arXiv:astro-ph/9506072.

M. Malquarti, E. J. Copeland, A. R. Liddle, and M. Trodden. A new view of k-essence. *Phys. Rev. D*, 67:123503, 2003.

R. Maoli et al. Cosmic Shear Analysis in 50 Uncorrelated VLT Fields. Implications for Ω_0, σ_8. *A&A*, 368(3):766–775, 2000, arXiv:astro-ph/0011251.

R. Massey et al. COSMOS: 3D weak lensing and the growth of structure. *ApJS*, 172: 239–253, 2007, arXiv:astro-ph/0701480.

J. C. Mather, D. J. Fixsen, R. A. Shafer, C. Mosier, and D. T. Wilkinson. Calibrator design for the cobe far infrared absolute spectrophotometer (firas). *ApJ*, 512(2):511, 1999.

J. D. McEwen, P. Vielva, M. P. Hobson, E. Martinez-Gonzalez, and A. N. Lasenby. Detection of the ISW effect and corresponding dark energy constraints made with directional spherical wavelets. *MNRAS*, 373:1211–1226, 2007, arXiv:astro-ph/0602398.

D. F. Mota, D. J. Shaw, and J. Silk. On the Magnitude of Dark Energy Voids and Overdensities. *ApJ*, 675:29–48, 2008, arXiv:0709.2227.

M. R. Nolta et al. First Year Wilkinson Microwave Anisotropy Probe (WMAP) Observations: Dark Energy Induced Correlation with Radio Sources. *ApJ*, 608:10–15, 2004, arXiv:astro-ph/0305097.

N. J. Nunes and D. F. Mota. Structure Formation in Inhomogeneous Dark Energy Models. *MNRAS*, 368:751–758, 2006, arXiv:astro-ph/0409481.

S. Padin et al. First Intrinsic Anisotropy Observations with the Cosmic Background Imager. *ApJ*, 549:L1–L5, 2000, arXiv:astro-ph/0012211.

S. Perlmutter, G. Aldering, G. Goldhaber, R. A. Knop, P. Nugent, P. G. Castro, S. Deustua, S. Fabbro, A. Goobar, D. E. Groom, I. M. Hook, A. G. Kim, M. Y. Kim, J. C. Lee, N. J. Nunes, R. Pain, C. R. Pennypacker, R. Quimby, C. Lidman, R. S. Ellis, M. Irwin, R. G. McMahon, P. Ruiz-Lapuente, N. Walton, B. Schaefer, B. J. Boyle, A. V. Filippenko, T. Matheson, A. S. Fruchter, N. Panagia, H. J. M. Newberg, W. J. Couch, and T. S. C. Project. Measurements of Ω and Λ from 42 High-Redshift Supernovae. *ApJ*, 517(2):565, 1999.

C. Pryke et al. Cosmological Parameter Extraction from the First Season of Observations with DASI. *ApJ*, 568:46–51, 2002, arXiv:astro-ph/0104490.

T. H. Puzia. Relative Ages of Globular Clusters. 2002, arXiv:astro-ph/0210418.

A. Rassat, K. Land, O. Lahav, and F. B. Abdalla. Cross-correlation of 2MASS and WMAP3: Implications for the Integrated Sachs-Wolfe effect. *MNRAS*, 377:1085–1094, 2007, arXiv:astro-ph/0610911.

C. L. Reichardt et al. High resolution CMB power spectrum from the complete

ACBAR data set. *ApJ*, 694:1200–1219, 2009, arXiv:0801.1491.

A. G. Riess and M. Livio. The First Type Ia Supernovae: An Empirical Approach to Taming Evolutionary Effects In Dark Energy Surveys from SNe Ia at $z > 2$. *ApJ*, 648:884–889, 2006, arXiv:astro-ph/0601319.

A. G. Riess et al. Observational Evidence from Supernovae for an Accelerating Universe and a Cosmological Constant. *ApJ*, 116:1009–1038, 1998, arXiv:astro-ph/9805201.

R. K. Sachs and A. M. Wolfe. Perturbations of a cosmological model and angular variations of the microwave background. *ApJ*, 147:73–90, 1967.

P. Schneider, L. v. Waerbeke, and Y. Mellier. B-modes in cosmic shear from source redshift clustering. *A&A*, 389:729, 2002, arXiv:astro-ph/0112441.

R. Scranton et al. Physical Evidence for Dark Energy. 2003, arXiv:astro-ph/0307335.

U. Seljak and M. Zaldarriaga. A Line-of-Sight Integration Approach to Cosmic Microwave Background Anisotropies. *ApJ*, 469:437, 1996, arXiv:astro-ph/9603033.

D. N. Spergel et al. Wilkinson Microwave Anisotropy Probe (WMAP) three year results: Implications for cosmology. *ApJS*, 170:377, 2007, arXiv:astro-ph/0603449.

P. J. Steinhardt, L.-M. Wang, and I. Zlatev. Cosmological tracking solutions. *Phys. Rev. D*, 59:123504, 1999, arXiv:astro-ph/9812313.

M. S. Turner. A New Era in Determining the Matter Density. *ApJ*, 576:L101–L104, 2002, arXiv:astro-ph/0106035.

S. Unnikrishnan, H. K. Jassal, and T. R. Seshadri. Scalar Field Dark Energy Perturbations and their Scale Dependence. *Phys. Rev. D*, 78:123504, 2008, arXiv:0801.2017.

Q. Wang and Z. Fan. Dynamical evolutin of quintessence dark energy in collapsing dark matter halos. *Phys. Rev. D.*, 79:123012, 2009, arXiv:0906.3349.

S. Weinberg. The cosmological constant problem. *Rev. Mod. Phys.*, 61(1):1–23, 1989, astro-ph/0005265.

J. Weller and A. M. Lewis. Large Scale Cosmic Microwave Background Anisotropies and Dark Energy. *MNRAS*, 346:987–993, 2003, arXiv:astro-ph/0307104.

M. J. White. Anisotropies in the CMB. 1999, arXiv:astro-ph/9903232.

I. Zlatev, L.-M. Wang, and P. J. Steinhardt. Quintessence, Cosmic Coincidence, and the Cosmological Constant. *Phys. Rev. Lett.*, 82:896–899, 1999, arXiv:astro-ph/9807002.